

Czech Technical University in Prague
Faculty of Mechanical Engineering
Department of Instrumentation and Control Engineering



**Control Systems and Electronics for 2.9 kW
Internal Combustion Engine and Battery Hybrid
Multicopter Based on Power Tracking Method**

Master's Thesis

Bc. Kengo Nagashima

Master Program: Automation and Instrumentation Engineering

Branch of Study: Instrumentation Technology

Supervisor: doc. Ing. Martin Novák, Ph.D.

Prague, July 2022

Declaration of Authorship

I, Kengo Nagashima declare that this thesis titled, “Control Systems and Electronics for 2.9 kW Internal Combustion Engine and Battery Hybrid Multicopter Based on Power Tracking Method” and the work presented in it are my own. I confirm that this work was done wholly while in candidature for a master’s degree at this university. Also, where I have quoted from the work of others, the source is always given. Except for such quotations, this thesis is entirely my work.

Signature:



I. Personal and study details

Student's name: **Nagashima Kengo** Personal ID number: **463976**
Faculty / Institute: **Faculty of Mechanical Engineering**
Department / Institute: **Department of Instrumentation and Control Engineering**
Study program: **Automation and Instrumentation Engineering**
Specialisation: **Instrumentation Engineering**

II. Master's thesis details

Master's thesis title in English:

Control Systems and Electronics for a 2.9 kW Internal Combustion Engine and Battery Hybrid Multicopter Based on Power Tracking Method

Master's thesis title in Czech:

Řídicí systém a elektronika pro 2,9kW hybridní multikoptéru

Guidelines:

1. Design of block connections for power electronics
2. Simulation model of a control system for a generator
3. Experimentally validated control system

Bibliography / sources:

- [1] Donateo, Teresa & Spedicato, Luigi & Placentino, Davide. (2017). Design and performance evaluation of a hybrid electric power system for multicopters. Energy Procedia. 126. 1035-1042. 10.1016/j.egypro.2017.08.310.
[2] Guillaume J.J. Ducard, Mike Allenspach, Review of designs and flight control techniques of hybrid and convertible VTOL UAVs, Aerospace Science and Technology, Volume 118, 2021, 107035, ISSN 1270-9638

Name and workplace of master's thesis supervisor:

doc. Ing. Martin Novák, Ph.D. Division of electrotechnics FME

Name and workplace of second master's thesis supervisor or consultant:

Date of master's thesis assignment: **29.04.2022** Deadline for master's thesis submission: **12.08.2022**

Assignment valid until: _____

doc. Ing. Martin Novák, Ph.D.
Supervisor's signature

Head of department's signature

doc. Ing. Miroslav Španiel, CSc.
Dean's signature

III. Assignment receipt

The student acknowledges that the master's thesis is an individual work. The student must produce his thesis without the assistance of others, with the exception of provided consultations. Within the master's thesis, the author must state the names of consultants and include a list of references.

Date of assignment receipt

Student's signature

Abstract

This thesis introduces control systems and power electronics for a MultiCopter (MC) equipped with a Permanent Magnet Synchronous Generator (PMSG) unit. The MC itself is powered by two batteries and the PMSG, coupled with a 2.9 kW Internal Combustion Engine (ICE). The Hybrid MC (HMC) comes from the combination of the batteries and PMSG unit that supports the MC for extending its flight time and range significantly. In other words, the hybrid configuration is a serial hybrid. The required power is measured by several sensors and calculated which gives feedback back to the control systems. And the power output is optimised. The method is named as “power tracking method”. The application for the HMC is considered mainly for emergency environments when electricity is not supplied. The chapter starts with designing the HMC body taking into account efficiency and safety. Afterwards, block connections for the HMC’s power electronics are introduced. Also, electronic components and related parts are selected to satisfy various requirements. Next, the PMSG unit’s control systems are designed on MATLAB/Simulink and they are implemented on a microcomputer. In the end, all works are validated experimentally.

Contents

Introduction.....	9
Design of HMC.....	16
2.1 Mechanism of MC.....	16
2.2 Efficiency and Safety of Rotor Position Configuration	17
2.3 3D Model	19
Design of Block Connection for Power Electronics	21
3.1 Overview and Selected Parts.....	21
3.2 Components.....	27
3.2.1 ICE and PMSG.....	27
3.2.2 BLDC Motor and Propeller.....	32
3.2.3 ESC	35
3.2.4 Buck-Boost DC-DC Converter	38
3.2.5 Battery Management System (BMS)	39
Design of Control Systems	41
4.1 Overview	41
Algorithm.....	46
4.1.1 Input	46
4.1.2 Estimator	48
4.1.3 Logic Controller.....	53
4.1.4 PID Controller.....	54
4.1.5 Output	55
Experimental Validations.....	58
5.1 Constructed HMC	58
5.2 PMSG Unit without GC	61
5.3 Control Systems with Electronics	63
Conclusion	78
Acknowledgement	79
References.....	80
Appendix.....	85

List of Figures and Tables

Figure 1 Milestones toward different unmanned vehicles and UAVs [9].....	9
Figure 2 Five levels of drone autonomy [10].....	10
Figure 3 UAV configuration types [10].....	11
Figure 4 Energy source comparison [10].....	12
Figure 5 Battery comparison [14].....	13
Figure 6 Drive configuration comparison.....	14
Figure 7 Kesennuma, Miyagi after 11 March 2011 [19]	15
Figure 8 Overview of FC (with PX4) and peripheral devices [22].....	17
Figure 9 Controller architecture of PX4 [22].....	17
Figure 10 Comparisons between shrouded and open propellers [25]	18
Figure 11 Extra power consumption map by propeller configuration [26].....	18
Figure 12 Coaxial same direction rotors motions with three rotors failure [28].....	19
Figure 13 3D model of designed HMC.....	20
Figure 14 PMSG unit simple overview.....	21
Figure 15 PMSG unit overview	23
Figure 16 PMSG unit block connection overview 1	26
Figure 17 PMSG unit block connection overview 2.....	26
Figure 18 Property map of small ICEs.....	28
Figure 19 General ICE characteristics [38].....	29
Figure 20 Estimation of ICE characteristics with reduction ratios	30
Figure 21 Torque transferring experiment, (a) setup, (b) and (c) originally manufactured parts	32
Figure 22 Comparison of T-motor products at 2 kg thrust with 24 V	33
Figure 23 Motor efficiency dependences.....	34
Figure 24 Thrust measurement setup.....	34
Figure 25 Thrust comparison between two propellers.....	34
Figure 26 EMAX BLheli-80A waveforms (yellow) with speed sensor waveforms (blue), (a) for lower speed and (b) for higher speed. T-motor ALPHA 60A 6S waveforms, (c) for lower speed and (d) for higher speed.....	35
Figure 27 ESC power vs. thrust comparison.....	36
Figure 28 ESC power/thrust ratio vs. thrust comparison	37
Figure 29 Efficiency map of DC-DC converter [43]	39
Figure 30 Two different BMS ports [44]	39
Figure 31 Small-scaled hybrid system experiment setup.....	40
Figure 32 GC overview.....	42
Figure 33 Device communication overview	42
Figure 34 GC program overview I/O (Motor speed sensors are not assigned).....	44
Figure 35 GC program overview	45
Figure 36 Current sensor program	46
Figure 37 Voltage sensor program.....	46
Figure 38 Oscilloscope (a) and photo tachometer (b) measurements	47
Figure 39 Speed sensor algorithm (actual duty ratio is 50 %)	48
Figure 40 Speed sensor program (for generator)	48
Figure 41 6-cell Lithium battery characteristics	49
Figure 42 6-cell Lithium battery SOC estimation by OCV method (original curve... grey dot).....	50

Figure 43 SOC estimation program (OCV, CC and their hybrid)	51
Figure 44 Thrust estimation program by power consumption	52
Figure 45 Thrust estimation program by thrust motor speeds	52
Figure 46 Required power estimation program by propeller thrusts	52
Figure 47 MOSFET logic controller flowchart.....	53
Figure 48 MOSFET logic controller program	54
Figure 49 Thrust PID controller.....	55
Figure 50 UART conversion program	56
Figure 51 MOSFET switch matrix program	57
Figure 52 Constructed HMC 1.....	59
Figure 53 Constructed HMC 2.....	60
Figure 54 Constructed HMC 3.....	60
Figure 55 1 st PMSG unit (a), burnt ESC as ICE starter (b) and experiment setup (c)	62
Figure 56 2 nd PMSG unit (a), worn right-angle adapter (b) and deformed tools (c).....	62
Figure 57 ICE with a propeller (a), 3rd PMSG unit (b), a moment when the new PMSG unit is destroyed (c), damage to bolts (d) and damage to pulley holder (e)	63
Figure 58 Current sensor data acquisition (top), frequency spectrum (middle) and designed low-pass filter characteristics (bottom)	65
Figure 59 Current sensor data acquisitions with filters (top) and zoomed view (bottom)	66
Figure 60 Voltage sensor data acquisition (top), frequency spectrum (middle) and zoomed view (bottom)	67
Figure 61 Voltage sensor data acquisitions with filters (top) and zoomed view (bottom).....	68
Figure 62 Speed sensor data acquisitions with filters (top) and zoomed view (bottom)	69
Figure 63 PWM signal (top) and conversion into duty ratio and ON/OFF signals (bottom).....	70
Figure 64 SOC estimation with BMS (a), battery cell voltages before and after 5 mins of charging (b) and (c).....	71
Figure 65 Estimated SOCs (top), zoomed views (middle) and (bottom).....	73
Figure 66 Voltage (top), voltage derivative (middle) and current (bottom) sensor data acquisitions during SOC measurement	74
Figure 67 Push button (top) and hybrid SOC (bottom) signals during SOC measurement	75
Figure 68 SOC (top), required and generator power (middle) and charging/discharging MOSFET PWM duty ratios (bottom)	76
Figure 69 Required and generator power (top) and throttle servomotor PWM duty ratio (bottom)...	77
Table 1 Selected parts for MC and PMSG unit	25
Table 2 Fuel comparisons [37]	29
Table 3 Estimated torque based on figure 21.....	30

List of Abbreviations

AI	Artificial Intelligence
BEMC	Battery Electrical Multicopter
BLDC	BrushLess Direct Current
BMS	Battery Management System
CC	Coulomb Counting
CFRP	Carbon Fibre Reinforced Plastic
ESC	Electrical Speed Controller
EV	Electrical Vehicle
FC	Flight Controller
GC	Generator Controller
GCS	Ground Control Station
HEV	Hybrid Electrical Vehicle
HMC	Hybrid Multicopter
ICE	Internal Combustion Engine
IMU	Inertia Measurement Unit
LPF	Low-Pass Filter
MAF	Moving Average Filter
OCV	Open Circuit Voltage
PDB	Power Distribution Board
PMS	Power Management System
PMSG	Permanent Magnet Synchronous Generator
PMSM	Permanent Magnet Synchronous Motor
SOC	State of Charge
UAV	Unmanned Aerial Vehicle
WL	Window Length

CHAPTER 1

Introduction

Since electronics parts such as Inertial Measurement Units (IMUs), batteries, and motors are developed dramatically, UAV technologies especially for MultiCopters (MCs) have grown surprisingly. Also, the demand for UAVs is increasing rapidly in recent years for use of agriculture, delivery services, military, and so on. Referring the military utilisation, it is mentioned that a swarm attack is a threat to a naval ship [1]. More and more developments and business chances are expected from UAVs and related industries. To accomplish various tasks for the mentioned applications, plenty of remarkable technologies are under development. For the hardware, a bladeless and safe quadcopter [2], deformable and flexible propellers [3] [4], tilting rotors for a quadcopter [5] and laser cutting quadcopter production [6] are interesting examples. Regarding the software, quadcopter flight stabilising when a rotor failure occurred [7], and quadcopter high-speed flight [8] are splendid and futuristic technologies. Also, interesting milestones for unmanned vehicles and UAVs are depicted in figure 1. According to the figure, there is a possibility of the trend of nano vehicles in the future.

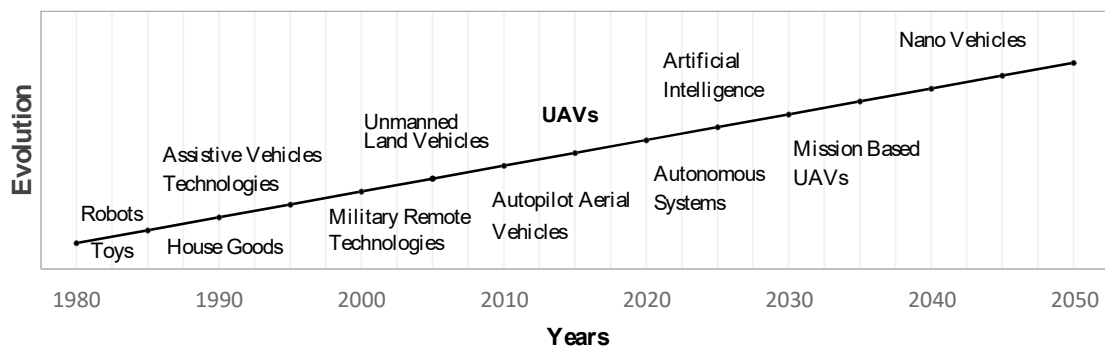


Figure 1 Milestones toward different unmanned vehicles and UAVs [9]

The current trends are autonomous flight and Artificial Intelligence (AI). In most cases, they are mounted on MCs and enable them to do given missions. Figure 2 illustrates the five-level of drone or UAV autonomy. Level 4 means UAVs are capable of flying outside

of a pilot's vision and have safety backups to correspond to some unexpected problems or situations. Both academy and industry are thrived to achieve level 4 autonomous flight at this moment. There is no doubt that AI, computer vision, control engineering and many other fields of study must be integrated for this purpose.













Autonomy Level	Level 0	Level 1	Level 2	Level 3	Level 4	Level 5
Human Involvement						
Machine Involvement						
Degree of Automation	No Automation	Low Automation	Partial Automation	Conditional Automation	High Automation	Full Automation
Description	Drone control is 100% manual.	Pilot remains in control. Drone has control of at least one vital function.	Pilot remains responsible for safe operation. Drone can take over heading, altitude under certain conditions.	Pilot acts as fall-back system. Drone can perform all functions 'given certain conditions'.	Pilot is out of the loop. Drone has backup systems so that if one fails, the platform will still be operational.	Drones will be able to use AI tools to plan their flights as autonomous learning systems.
Obstacle Avoidance	NONE	SENSE & ALERT		SENSE & AVOID	SENSE & NAVIGATE	

Figure 2 Five levels of drone autonomy [10]

UAVs are classified into some categories by their flight method or mechanism as represented in figure 3. The fixed-wing UAVs are quite common and are applied practically in the military for a long period. The hybrid section indicates UAV combinations with fixed-wings and MCs called Vertical Take-Off and Landing (VTOL) UAVs. Popularity is also focused on them since they take the advantage of two different types of UAVs. Not only the classification but there is one by multiple energy sources [11]. The most common is using electricity from a battery because it is simple and cheap. Meanwhile, one utilising fuel and four-stroke Internal Combustion Engines (ICEs) for rotating propellers directly as mechanical energy and it flies like a quadcopter [12]. For the fixed-wing or VTOL types, an ICE is quite often mounted for the longer flight time and range.

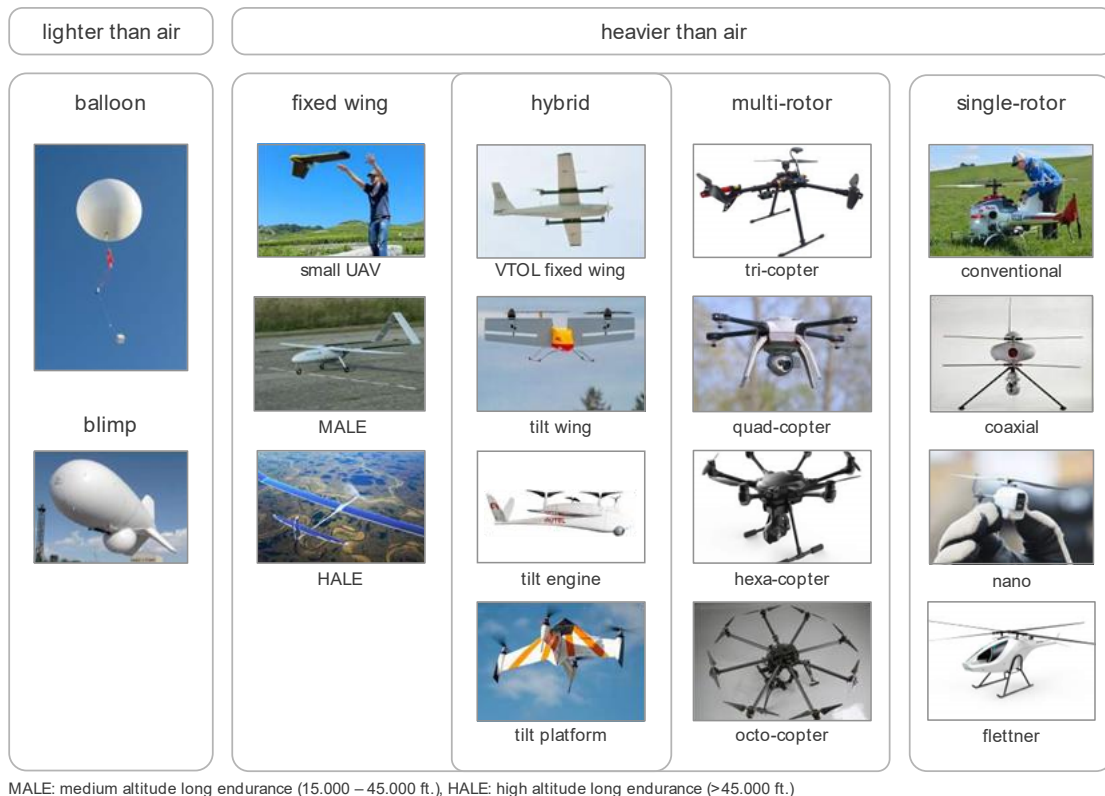


Figure 3 UAV configuration types [10]

Considering only MCs, there are various limitations in them and the critical one is their flight time and range. Figure 4 displays the comparison of various energy sources with their energy density per 1 kg and 1 L. In the figure, gasoline is located quite further from the axes and is over 10000 Wh/kg and Wh/L respectively. And hydrogen is considered a promised and futuristic energy source. One thing that has to be mentioned is that all energy is not possible to convert perfectly and the referred values are lower after the conversion into electrical energy. However, the energy density is significantly larger than the batteries and incomparable. Also, energy source containers cannot be forgotten and the comparison is introduced in [13]. It is possible to say that the tank for gasoline/ICE still has the advantage in its volume which is beneficial to UAVs or MCs.

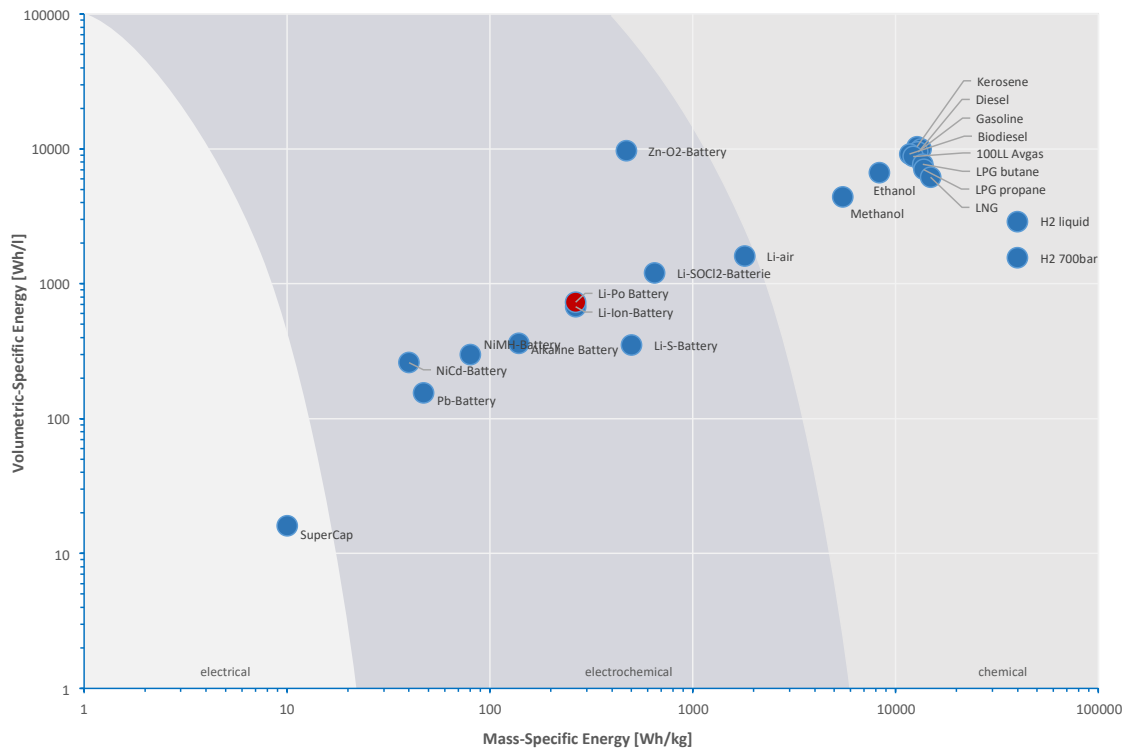


Figure 4 Energy source comparison [10]

Focusing on only batteries, figure 5 describes the battery comparison with their energy and power density per 1 kg. A parameter, power density is an important factor for batteries since the flowable current depends on it. The state-of-art battery, the solid-state battery is focused on research as a feasible next-generation battery. However, the energy and power densities are still less than 1000 Wh/kg and kW/kg respectively at this moment. While the competition in Electrical Vehicles (EVs) is fierce everywhere, battery technology is the mandatory key. MCs are also inevitable to follow the trend but flying and keeping an object in the air requires vast energy and are not possible to reuse the energy, unlike ground vehicles. Therefore, a different approach is necessary for them in the current situation, especially for industrial ones.

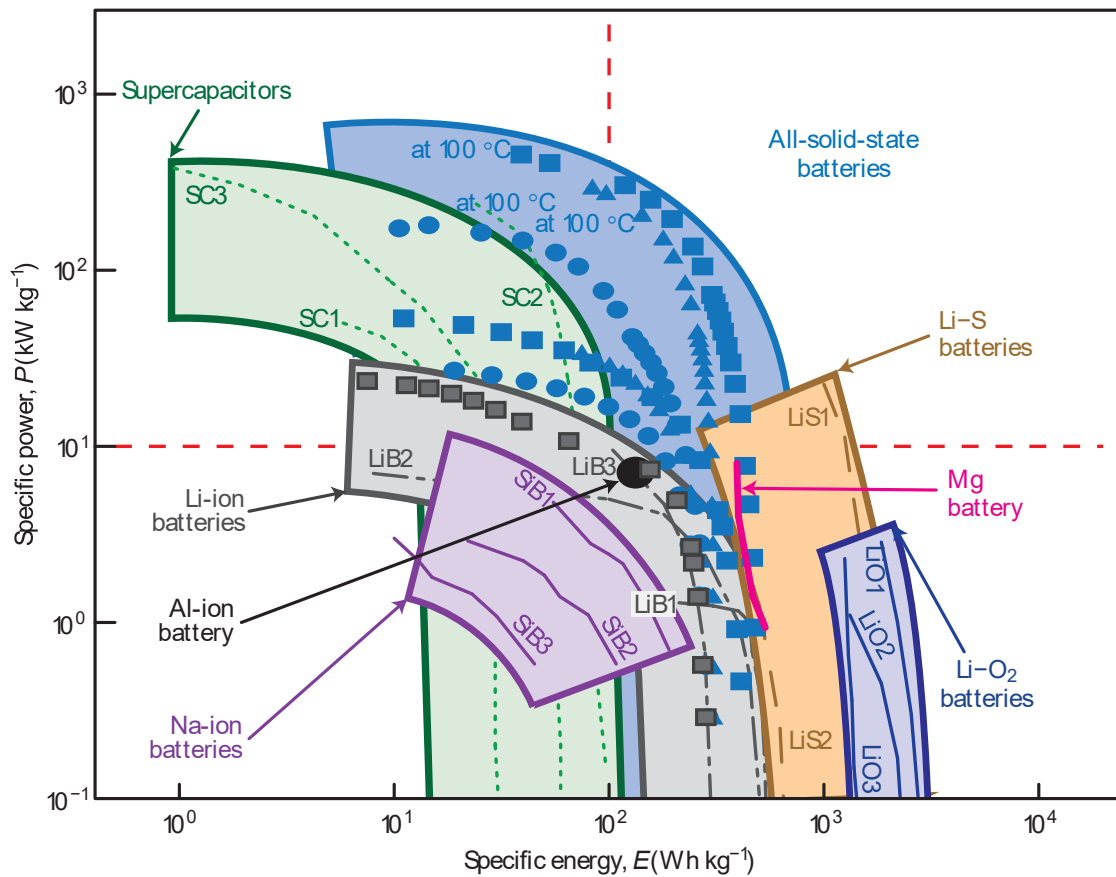


Figure 5 Battery comparison [14]

Considering the revealed facts, it is possible to come up with the idea of making a hybrid system to compensate for the disadvantage. And Hybrid Electrical Vehicles (HEV) are already well developed and succeeded in their business such as Toyota Prius. There is no wonder to think of applying the techniques to hybrid UAVs. However, there are differences between HEVs and hybrid UAVs that cannot apply the hybrid technologies for them directly and they have to adapt to each characteristic [15] [16]. Hybrid systems can be divided into two, one is a rule-based control algorithm and another is an optimisation-based control algorithm [17]. In this thesis, the rule-based control algorithm is applied. Based on the algorithm, a method that senses mechanical and electrical parameters and varies the produced power is named the “power tracking method”. For a hybrid fixed-wing UAV, the method is suitable for better fuel consumption efficiency in a condition that the consumed power changes smoothly like cruising compared to terrain tracking [18].

Similar to HEVs classifications [13], hybrid UAVs or HMCs can be sorted by their hybrid configuration as shown in figure 6. The applied method in this thesis is the serial configuration since it is simple and attachable to already existing MCs easily. The disadvantage is its efficiency because the energy is converted into only electrical energy not utilising the mechanical energy directly like the other hybrid methods.

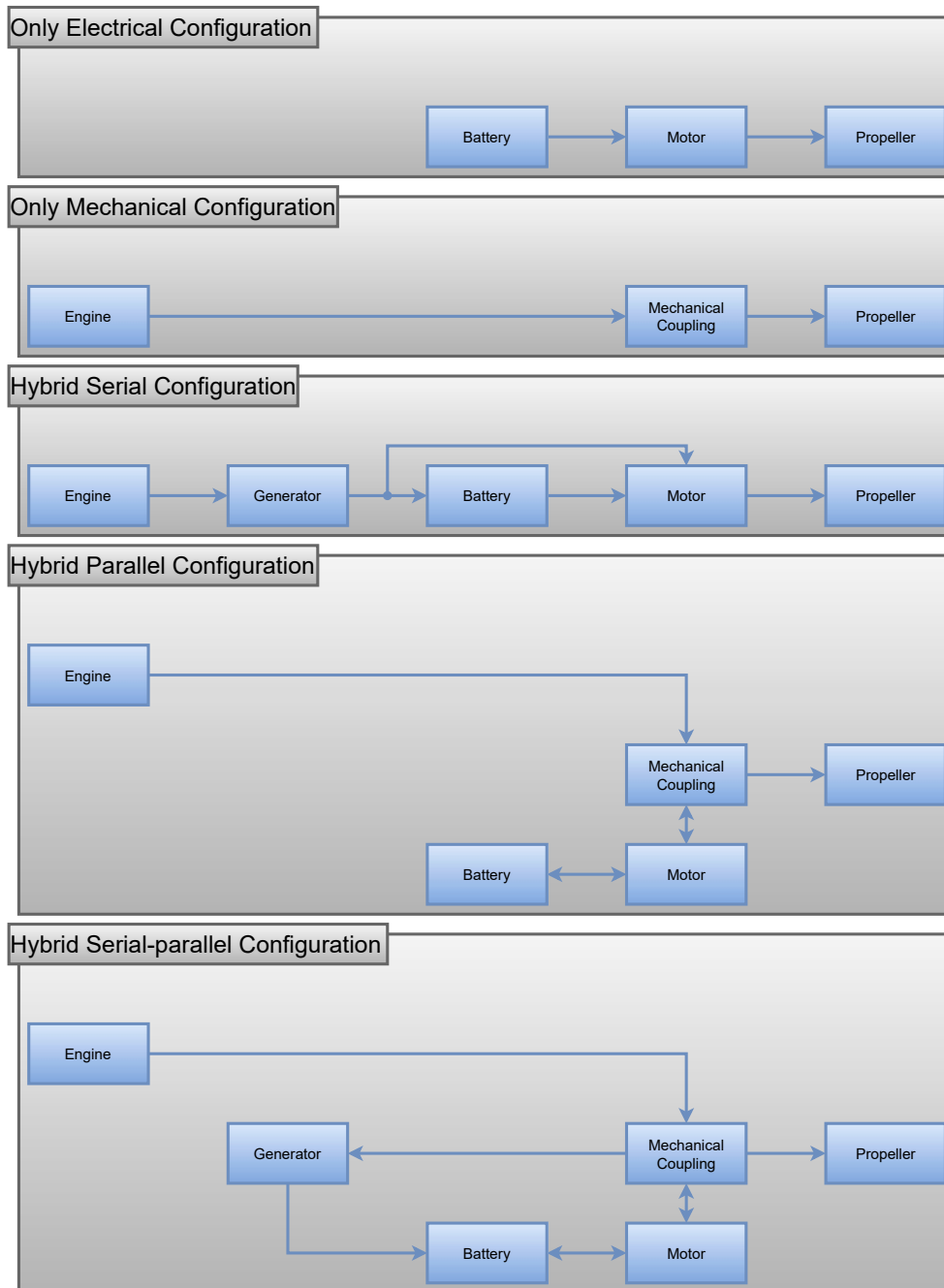


Figure 6 Drive configuration comparison

The purpose of this thesis is to develop an HMC with an ICE and batteries which enhances the flight time and range dramatically and is usable in emergencies such as earthquakes or tsunamis. Figure 7 displays the aftermaths of the Great East Japan earthquake in March 2011. For instance, delivering medical kits, foods or essential items is an option for use. Surveying the disaster situation, and finding or rescuing people are the other ideas. During such an unprecedented environment, infrastructure including electricity supply is destroyed and shut down. Meanwhile, gasoline is an essential item for every transport, storable in tanks and much easier to get. Therefore, the designed MC is capable of its flight only by fuel which is a mixture of gasoline and engine oil. The small backup power is supplied from AA batteries and their extras are kept in the MC. The MC has the function of a generator and can store the electrical energy into the mounted main LiPo batteries. Also, it is designed compactly, efficiently and simply so that more developed MCs based on this prototype can be deployed at various spots like hospitals, fire stations or city halls and trained people can operate the MCs easily. Thus, there will be more chances to save more people.



Figure 7 Kesenuma, Miyagi after 11 March 2011 [19]

CHAPTER 2

Design of HMC

In this chapter, the body design for the HMC is introduced. Taking and keeping the enormous advantage from gasoline as an energy source, the HMC is designed to mount a Permanent Magnet Synchronous Generator (PMSG) unit safely and stably. The chapter starts with a quick explanation of the principles of an MC. Afterwards, efficient and safe configurations of rotors are explained by referring to various sources. In the end, a 3D model is created explaining the features.

2.1 Mechanism of MC

A battery-driven MC is quite simple being composed of several motors, Electrical Speed Controllers (ESCs), a battery and a Flight Controller (FC) in general. The detailed mechanical principle is not explained in this thesis but varying the speed of rotors with propellers enables the amazing dynamic manoeuvre [20]. Considering the software or controlling part, Several control methods such as non-linear or predictive control are already existed [21]. However, PID control is quite common and is often implemented in most MCs. For the designed HMC, a Pixhawk with PX4 or Ardupilot is utilised. An overview of the FC (with PX4) and peripheral devices, is revealed in figure 8. And a controller architecture of PX4 is described in figure 9. The first figure indicates that the FC is manipulated in two ways, one is by a radio transmitter and another is by a ground station (Ground Control Station (GCS) or QGroundControl for PX4). It is a command computer connected to a transmitter and utilises the MAVLINK protocol for communication. Motors or ESCs are controlled by PWM signals and communications between some sensors are done by various protocols as explained. Regarding the next figure, the architecture is in cascade form controller with a mixture of P and PID controllers (depending on the selected mode, it is changeable) and extended Kalman filters are applied to estimate the values. Inside the PID controllers, not typical parallel

PID controllers but applied PID controllers such as PI-D or K-PID controllers are implemented with anti-windup functions.

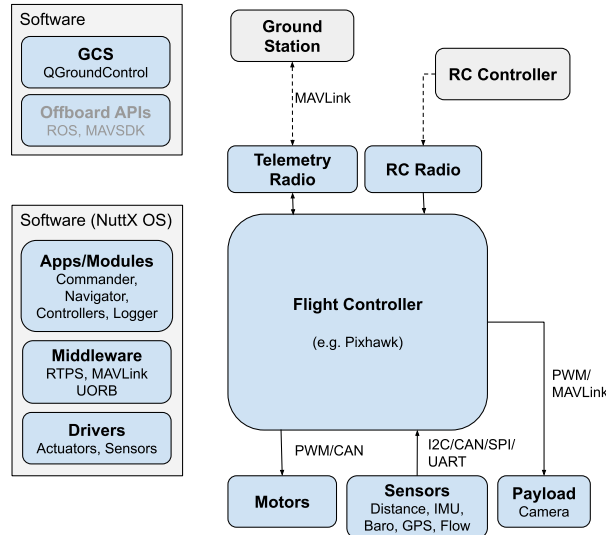


Figure 8 Overview of FC (with PX4) and peripheral devices [22]

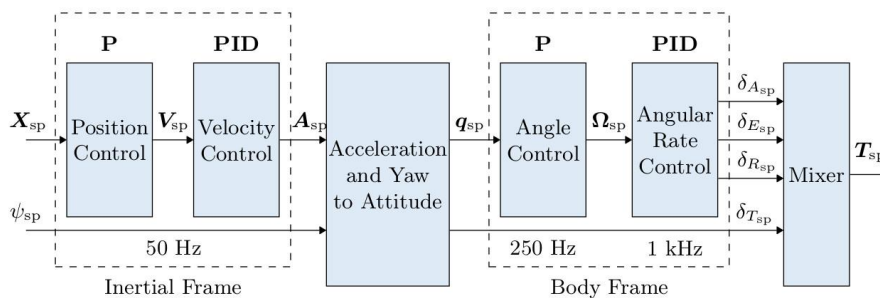


Figure 9 Controller architecture of PX4 [22]

2.2 Efficiency and Safety of Rotor Position Configuration

At first, considering propellers, the characteristics of a propeller vary by a small difference dramatically [23] and it is reasonable to design a propeller suited for MCs since the properties between MCs and fixed-wing UAVs are different completely. For achieving a longer flight time and range, the efficiency can never be forgotten. ESCs, motors and other electronics parts are crucial for better efficiency. In addition, the rotor position configuration is mandatory to consider since it affects flight safety significantly as well [24]. Not only the propeller geometry but a surrounding around the propeller,

shroud affects the thrust as indicated in figure 10 and it implies the efficiency is also affected. The figure illustrates that a shrouded rotor (even considering its weight) has a larger thrust compared to an open rotor. This resource approached only for a 6.3-inch rotor but still, a similar result can be expected for a much bigger propeller.

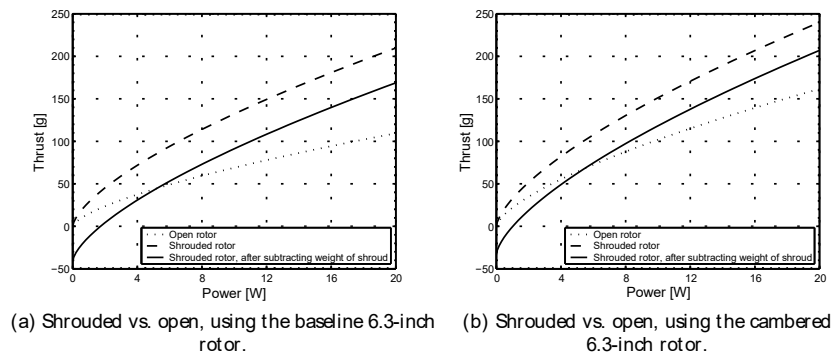


Figure 10 Comparisons between shrouded and open propellers [25]

Increasing the thrust of MCs is achieved by increasing the number of rotors. However, there is a limit for it due to the body size limitation and so on. It is logical to think of designing coaxial rotors instead. Figure 11 introduces an extra power map for opposite-direction coaxial rotors compared to independent single rotors which have 10 N thrust in total. The distance and overlap mean the distance and overlap between the top and bottom rotors based on their rotor diameter. It can be seen that the closer distance of approximately 0 to 20 % and overlap of around 10 % indicate the best results

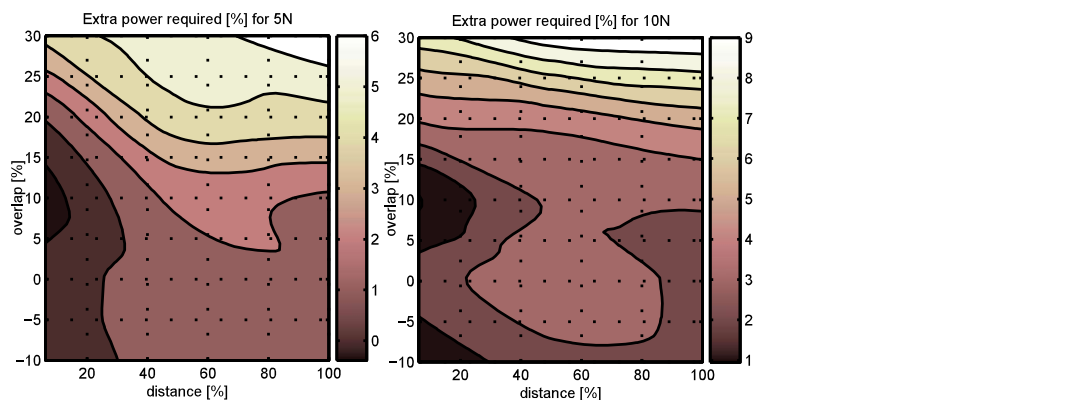


Figure 11 Extra power consumption map by propeller configuration [26]

Regarding the coaxial rotor direction, both opposite-direction has better efficiency than both same directions [27]. From the mentioned facts, coaxial and opposite-direction

rotors seem suitable for MCs. However, safety also has to be considered. Figure 12 describes the numerical behaviour of a coaxial and same-direction MC in case its three rotors' failure occurred. It indicated that the MC is still able to keep flying stably since the other same-direction rotors compensate for the thrust. Other rotor position configurations such as the coaxial opposite-direction and a normal quadcopter are not possible to keep such a stable flight if three rotors are failed. Especially for quadcopters, one rotor failure leads to a crash. Therefore, for keeping the efficiency and safety advantages at the same time, some rotor position configurations are suggested in [27].

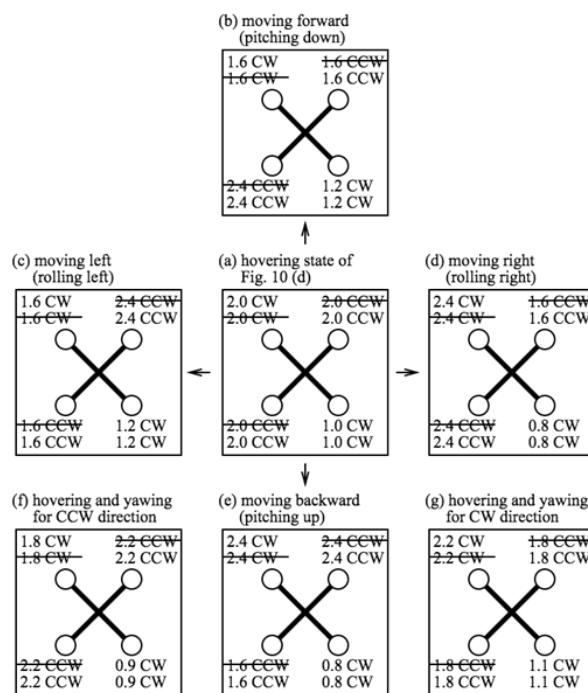


Figure 12 Coaxial same direction rotors motions with three rotors failure [28]

2.3 3D Model

Figure 13 shows the 3D model for the designed prototype MC. To meet the weight requirement, size limitation and efficiency as referred to in the previous pages, eight rotors in the coaxial and opposite direction with slightly tilted foldable arms are designed. The rotor diameter is approximately 1000 mm and the propeller size is 22-inch. The weight is expected around 15 kg including 2 L of fuel and two 4000 mAh LiPo batteries. The body structure is a combination of layered-same-designed plates and tubes for cost

reduction. The skid is slightly reinforced for a strong impact of landing and supporting the weight. For ensuring, a wire pass-through in the skid tubes that gives more strength. The ESCs and other heating parts are well exposed to the propeller air. The antennas and other communication parts are mounted away from devices (such as an ICE ignitor) that emit strong electromagnetic waves to avoid interferences. The centre of gravity is located under the thrusts and acts as a pendulum which makes the MC stable. Under the rotors, objects that do not disturb the flowing air, additional tanks or other parts can be mounted. The torque from the ICE to the PMSG is transferred by a timing belt mounted on separate top and bottom plates respectively. The layered-plates structure and the ICE geometry match the design well. Since the vibration from the ICE (two-stroke ICE for this project) is quite strong, the installation of dampers is necessary to prevent a failure in MC itself [29]. Therefore, rubber dampers between the PMSG unit and MC body are installed and join them. Altering the ICE or torque transferring mechanism (which are mentioned in the next chapter) are other ways to suspend the vibrations. Regarding the material, Carbon Fibre Reinforced Plastics (CFRPs) are utilised mainly for the body and they have good characteristics in weight, strength and vibration attenuation [30]. However, CFRP has to be utilised carefully because its properties can change significantly by its weaves [31] and layer configuration [32]. The joint parts are made of aluminium. The wire thickness affects the consumed power that can never be neglected [33] and the power losses are estimated quite hugely, especially in this MC with a low voltage and high current system.



Figure 13 3D model of designed HMC

CHAPTER 3

Design of Block Connection for Power Electronics

In this chapter, power electronics in the MC and PMSG unit are introduced by designing their block connections. Starting from an overview of the block connections for power electronics, the selection of those parts is explained.

3.1 Overview and Selected Parts

First of all, the system voltage is set as 6S which is around 24 V due to the low cost of LiPo batteries. However, lower voltage leads to higher currents and larger energy losses and it is not ideal for achieving higher efficiency. It would be a great choice to apply a 12-cell (48 V) system for a high efficient MC. A simple overview of the PMSG unit is illustrated in figure 14. It starts from an ICE and its torque is transferred by a timing belt to a PMSG that emits a three-phase current and they are rectified into direct current. For stabilising and matching the appropriate output voltage, DC-DC converters are utilised. Most stabilised power goes to a 24 V bus directly and a few portions of the power go to batteries for charging. Meanwhile, the batteries can discharge into the 24 V bus to compensate for the power shortage very quickly as if acting like a capacity.

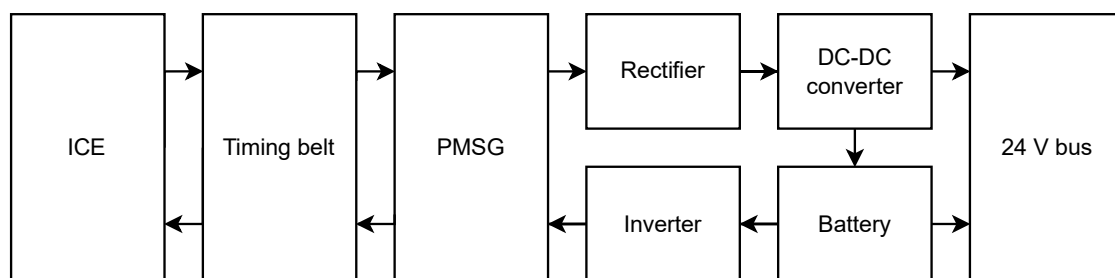


Figure 14 PMSG unit simple overview

A more detailed overview is revealed in figure 15 with various arrow lines and various colours. Small dashed, big dashed and normal line arrows represent mechanical, communication and power connections respectively. Pink, orange and green arrows

indicate ways after a branch point, way 1 for 24 V bus directly, way 2 for charging and way 3 for discharging respectively. Red, yellow and blue block colours imply types of objects, mechanical actuator, energy source and controller respectively. In the figure, it starts from an ICE (GT-33) with an ignitor (IG-02) and fuel. The torque is transferred by a timing belt (5 mm HTD) to a PMSG (MN8017 KV120) that emits a three-phase current and they are rectified into direct current. For stabilising and matching the system voltage of 24 V, three DC-DC buck-boost converters (24 V, 30 A, 720 W) for each, are utilised. Five MOSFETs (60 V, 100 A) are for the ICE starter which is mentioned later. The current and voltage are measured and there is a branch point. Way 1 is connected to another current sensor and goes to a Power Distribution Board (PDB). On way 2, a MOSFET unit (40 V, 50 A) is connected for controlling charging. After that, a DC-DC boost converter (6 A, 150 W) increases the voltage to a slightly higher than the battery voltage around 25.2 V and limits the following current. Since there are two batteries (6S LiPo 4000 mAh 60C), each line has a current sensor, a voltage sensor and a Battery Management System (BMS) board (35 A) that monitor and protect the batteries. For way 3, the current is measured again and ten MOSFETs (60 V, 100 A) control discharging quickly and go to the PDB merging with way 1. All MOSFETs keep a much larger maximum current in parallel connections for safety. For starting the ICE, the PMSG is also connected to an inverter (and a rotary encoder in the case of Odrive) with relays and they are used only when starting. While not used, they are isolated by relays to avoid a short circuit. To operate the high current, there is one with a coiled mechanical relay and another with a photodiode relay. The voltage is adjusted for the relays. The speed of the PMSG is measured by a speed sensor and the ICE is controlled by servomotors. Also, the speeds of the thrust motors are measured. To ensure the operation of a Generator Controller (GC), an auxiliary battery with a DC-DC buck converter (5 A, 75 W) is mounted. The voltage is slightly lower than the voltage from the PDB with a DC-DC buck converter (20 A, 300 W) to prevent the current backflow. Every input voltage signal from the mentioned sensors and output voltage signal is processed by the GC which is a microcontroller (NUCLEO-F767ZI) at the centre of the figure. Also, it communicates with two transmitters and the FC by PWM signals and UART protocol respectively.

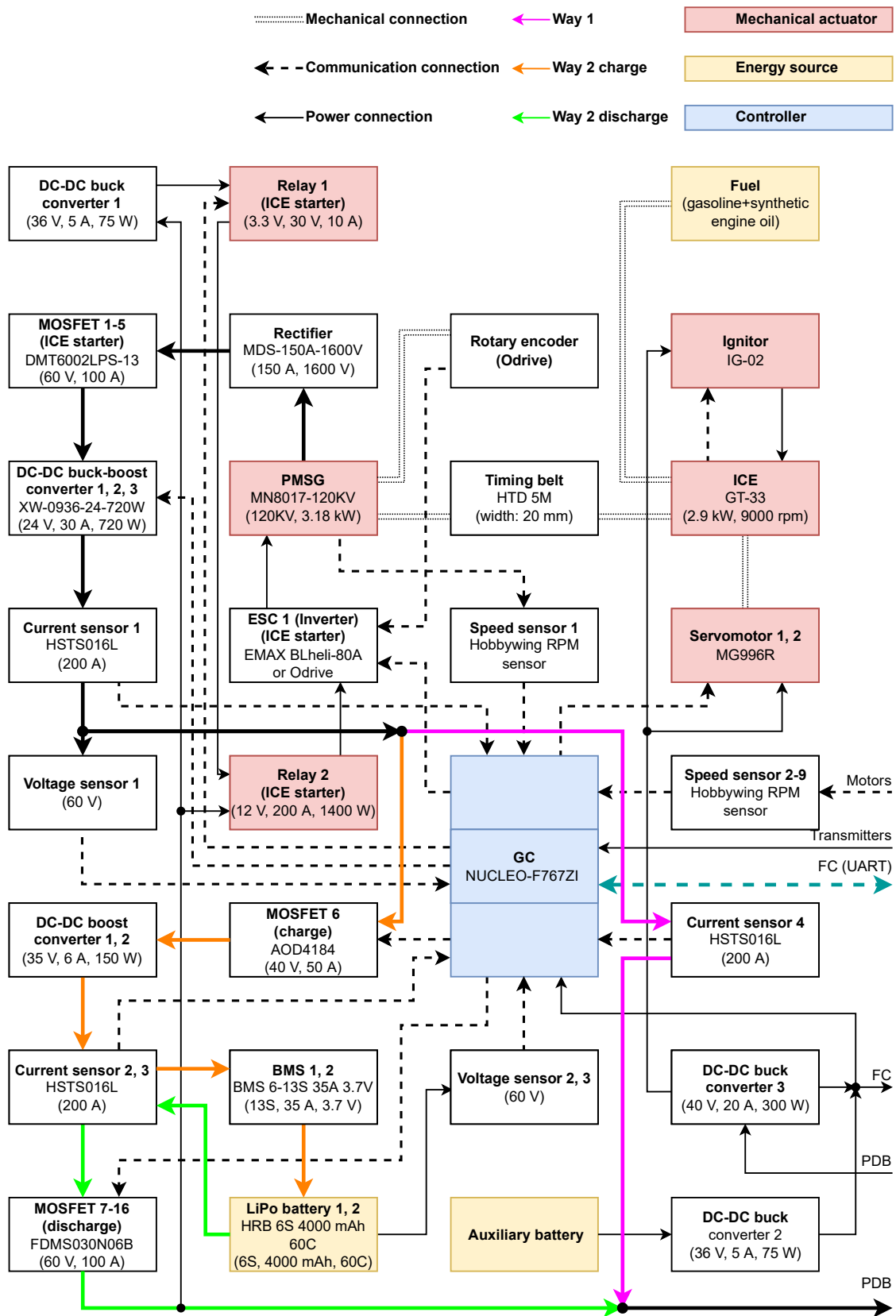


Figure 15 PMSG unit overview

Considering the practical connections, figures 16 and 17 depict the first and second parts of the PMSG unit respectively. Major differences from the previous figures are additions of various electronics components such as diodes or capacitors.

Looking at the first figure, five capacitors after the rectifier are connected in parallel for smoothing the output wave. The positive terminal is connected to the DC-DC buck-boost converters while the negative terminal is connected to the five MOSFETs as relays for starting the ICE. Since the expected current is up to 90 A from the DC-DC converters, The gate voltage is supplied from a level shifter to change the appropriate voltage around 5 V for the five MOSFETs with pull-down resistors. The output from the DC-DC converter is also connected with supercapacitors for better performance [34]. The terminal voltage is dropped to around 3 V so that the GC can measure it. To avoid high voltage to the GC in some cases, two Zener diodes are installed. For the ICE starter, there is a branch from the PMSG. One way is to the rectifier as mentioned already and another is connected to the ESC to control the PMSG as a motor with the relays and free-wheeling diodes since it is a coiled mechanical relay. Those relays have enough margins to allow the unexpected higher voltage [35]. The speed sensor connects to two PMSG terminals and outputs pulsed waves with various periods depending on PMSG speed.

Regarding the last figure, five Schottky diodes which have enough safety factors are installed towards the 24 V bus for backflow prevention. The reason why the Schottky diodes are selected is to match the same components as others and they can be alternated with normal diodes. From a branch after one of the current sensors, two diodes are set for backflow prevention. When charging the batteries, the DC-DC boost converters increase the voltages to 25.2 V and the currents flow into the batteries through BMSs. The voltages are monitored externally by the same principle as before. The BMSs are utilised for balancing the batteries' cells mainly. Since BMSs accepting higher currents are much more costly, the BMSs with lower currents are selected. However, the problem is how to manage the higher current because the expected currents from the batteries are up to 240 A (4000 mAh, 60C) each. While, during the charge, the current flow is only up to 4 A (4000 mAh, 1C) each. Therefore, bypass connections [36] are applied for the discharge as represented in the figure. It means that currents flow through the BMSs only when

charging and the currents when discharging head to the 24 V bus directly. To control the currents, the five MOSFETs with pull-down resistors in each battery are implemented with also enough safety factors. Since the switching of the current flows can be done quickly, five Schottky diodes which have a good property in high-speed switching, for each unit are applied. The selected major parts for the MC and PMSG unit are listed in table 1 with their product names or some important specifications in brackets. The parts that are not utilised for the PMSG unit are also added in bold letters.

BMS 1, 2	Broodio BMS 6-13S 35A 3.7V (13S, 35 A, 3.7 V)
Current sensor 1-3	HSTS016L (200 A)
DC-DC boost converter 1, 2	(35 V, 6 A, 150 W)
DC-DC buck converter 1, 2	(36 V, 5 A, 75 W)
DC-DC buck converter 3	(40 V, 20 A, 300 W)
DC-DC buck-boost converter 1-3	XW-0936-24-720W (24 V, 30 A, 720 W)
ESC 1 (inverter) (ICE starter)	EMAX BLheli-80A (6S, 80 A) or Odrive
ESC 2-9 (thrust motor)	EMAX BLheli-40A (6S, 40 A)
FC	Pixhawk (clone)
GC	NUCLEO F767ZI
ICE	GT-33 (2.9 kW, 9000 rpm)
Ignitor	IG-02
Level shifter 1, 2	TXS0108E
LiPo battery 1, 2	HRB 6S 4000 mAh 60C (6S, 4000 mAh, 60C)
MOSFET 1-5 (ICE starter)	DMT6002LPS-13 (60 V, 100 A)
MOSFET 6 (charge)	AOD4184 (40 V, 50 A)
MOSFET 7-16 (discharge)	FDMS030N06B (60 V, 100 A)
PMSG	MN8017-KV120 (120KV, 3.18 kW)
Propeller	(CFRP 22-5.5inch)
Rectifier	MDS-150A-1600V (150 A, 1600 V)
Relay 1 (ICE starter)	(3.3 V, 30 V, 10 A)
Relay 2 (ICE starter)	(12 V, 200 A, 1400 W)
Servomotor	MG996R
Speed sensor 1-9	Hobbywing RPM sensor
Thrust motor	MN6007II (360KV, 1.04 kW)
Timing belt	HTD 5M (width: 20mm)

Table 1 Selected parts for MC and PMSG unit

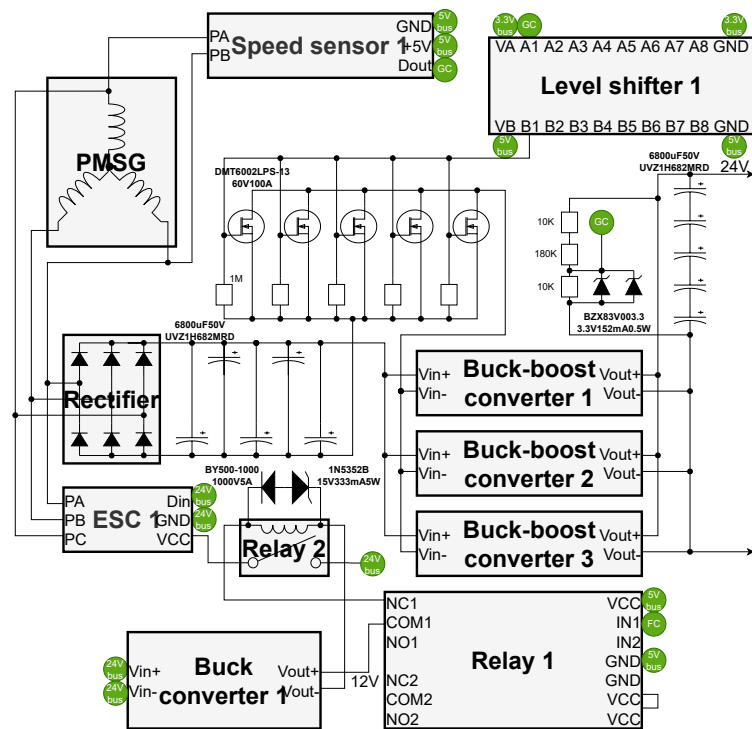


Figure 16 PMSG unit block connection overview 1

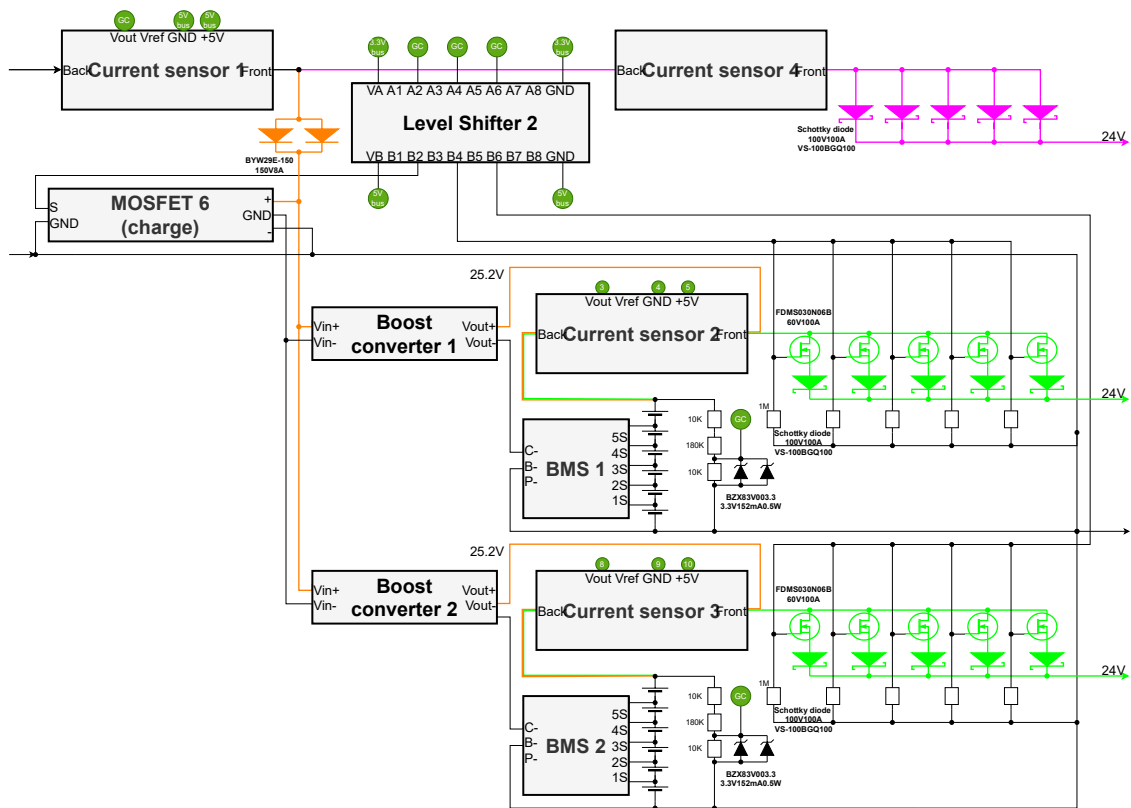


Figure 17 PMSG unit block connection overview 2

3.2 Components

3.2.1 ICE and PMSG

Selecting an appropriate ICE for a hybrid UAV is the beginning of the design and determines the characteristics of the hybrid UAV. Figure 18 displays various types of ICEs for hobby-use small vehicles. There are four classifications for such ICEs mainly, the one is on which types of vehicles are suitable for being mounted. The ICEs for cars, boats, helicopters and aeroplanes are major and they are modified for the best performance in their utilisation. The position of their silencers, the size of their cooling heads and the speed-torque-power characteristics are the apparent differences. The second classification is the ICE mechanisms. Reciprocating, rotary and turbine ICEs are representative. Depending on the mechanisms, the rest two classifications are also determined which are the types of available fuels and the number of strokes respectively. To suit the HMC, an ICE with one-cylinder, two-stroke and gasoline is chosen. The exact model is GT-33 from OS engine which produces high-quality products. The definitive reason is its cost-effect, the ICE costs 500 USD approximately and its simplicity. Its cylinder has 33 ccs and the power is 2.9 kW maximum at 9000 rpm which is enough power to lift an object over 15 kg in the air (the detail is introduced later). Two-cylinder ICEs are more suitable than one-cylinder ICEs for UAVs due to their vibration property and they tend to cancel out vibrations by the two-cylinders [29]. Also, four-stroke ICEs produce fewer vibrations than two-stroke ICEs. Meanwhile, four-stroke ICEs are composed of more parts than two-stroke ICEs. However, the ICE cost and simplicity exceed those benefits this time.

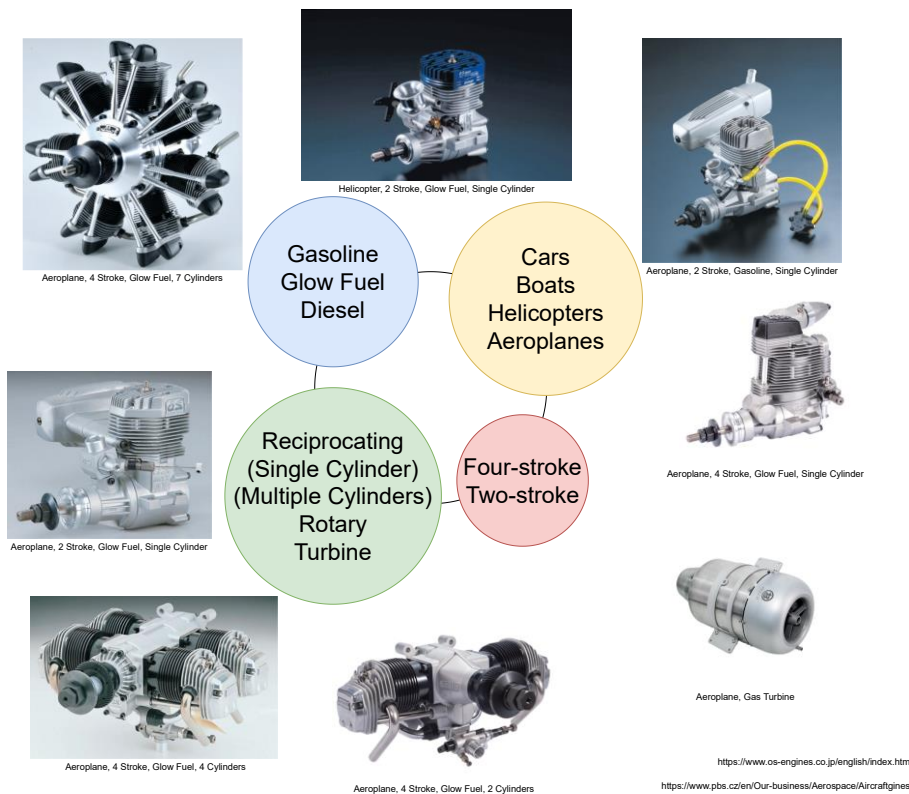


Figure 18 Property map of small ICEs

The selected ICE works with gasoline with some portion of engine oil. Meanwhile, there are ICEs supplied by a fuel called glow fuel which is a mixture of methanol and nitromethane. They are also popular ICEs since they do not require an external ignitor. Properties of various fuels are compared in table 2. The important factors are stoichiometric air-fuel ratio and calorific value. The first one represents the ratio between inlet air and fuel in the cylinder. In other words, 1 g of gasoline and approximately, 15 g of air can react or combust perfectly. Thus, gasoline does not need to be consumed as much as glow fuel (methanol and nitromethane) does [37]. The second one means the thermal energy produced when combusted perfectly. Gasoline has around twice a larger value than glow fuel (methanol and nitromethane). However, more glow fuel than gasoline can be fit in the cylinder and it can produce the same or more thermal energy [37]. In general, efficiency is an important key for HMC. Taking account of all revealed facts, gasoline is more economical and can produce more energy by a small amount of it. Therefore, again, GT-33 as an ICE is selected.

	Methanol	Nitromethane	Gasoline	Diesel
Molecular formula	CH ₃ OH	CH ₃ NO ₂	C _n H _m (C ₄ -C ₁₁)	C _n H _m (C ₁₁ -C ₁₆)
Molecular weight	32.04	61.04	About 100 (average)	About 200 (average)
Density (20 °C) [g/cm ³]	0.793	1.139	0.72-0.78	0.83-0.85
Boiling point (760mmHg) [°C]	64.65	101.2	17-220	180-360
Stoichiometric air-fuel ratio [kg/kg]	6.45	3.96	About 15	About 15
Calorific value [kcal/kg]	5330	5370	About 10,500	About 10,200
Flash point [°C]	11	35	About -40	About 70
Ignition temperature [°C]	470	418	About 260	About 230
Combustible range [vol%]	6.7-36	7.3-∞	1.4-7.6	0.6-7.5
Calorific value [kcal / kg]	∞	10.5 wt%	About 290 ppm	
Water solubility (20 °C)	∞	2.2 wt%	About 80 ppm	
Vapor density (air = 1)	1.11	2.11	3-4	

Table 2 Fuel comparisons [37]

The typical characteristics of an ICE are described in figure 19. The x-axis is the speed and the y-axis is the torque on the right side and the power on the left side. It can be seen that they are not linear apparently and there are three regions called low end, power band and high end. It is ideal to work in the power band area for better performance.

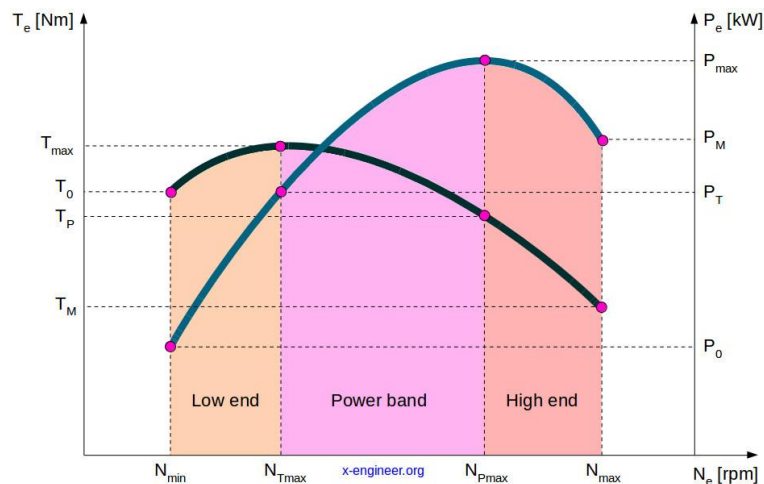


Figure 19 General ICE characteristics [38]

Since the selected ICE's characteristic curves are not published by the manufacturer, they have to be estimated from the given specifications which are 2.9 kW at 9000 rpm. Based on the information, figure 20 depicts the simply estimated speed-power lines. The three right lines are when the maximum power is 2.9 kW at 9000 rpm starting from 0 kW at 0 rpm with 1, 1.2 and 1.5 reduction ratios respectively. In addition, the left lines are when the maximum power is 2.9 at 5000 rpm starting from 0 kW at 0 rpm with the same reduction ratios. The estimated speed-power lines are for choosing a proper timing belt

and a proper pulley which is connected to the PMSG. From the figure, the torques are calculated in table 3 by equation (1) as follows where T is torque in [Nm], P is power in [W] and ω is the speed in [rad/s].

$$T = \frac{P}{\omega} \quad (1)$$

One of the reasons, why the reduction ratios 1.2 and 1.5 are picked up, is the availability of the pulleys. Another is that they match the PMSG characteristics and logical explanations of the selection follow in the next pages. The published characteristics data (for motor use) from the manufacturer is in [39].

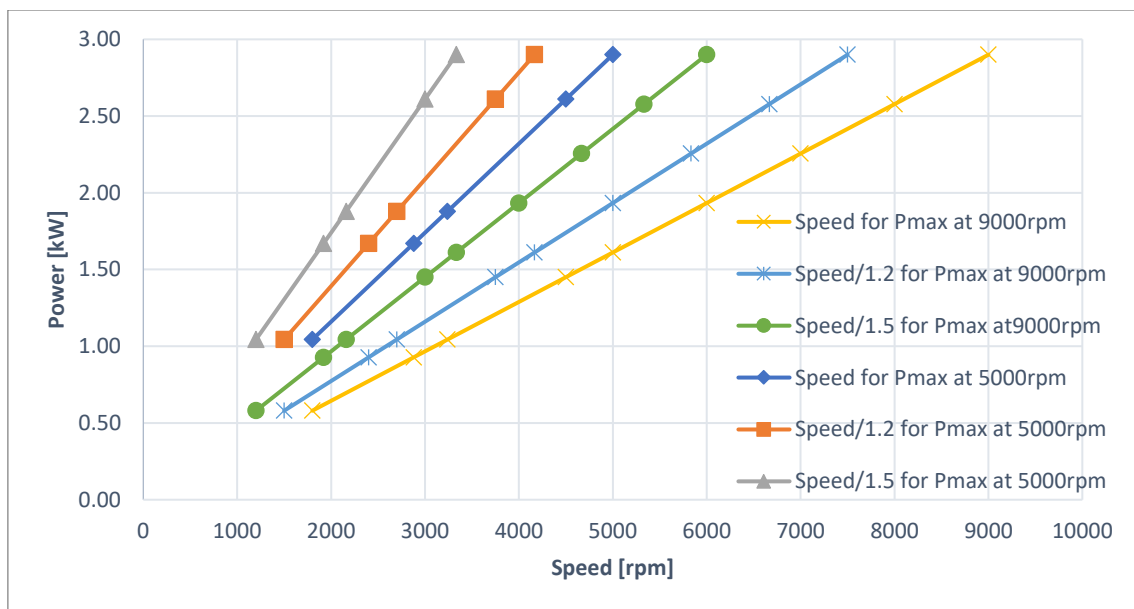


Figure 20 Estimation of ICE characteristics with reduction ratios

Torque [Nm]	Torque*1.2	Torque*1.5	Torque [Nm]	Torque*1.2	Torque*1.5
Speed for Pmax at 9000 [rpm]			Speed for Pmax at 5000 [rpm]		
3.08	3.69	4.62	5.54	6.65	8.31

Table 3 Estimated torque based on figure 21

Regarding general motor parameters, every motor has some constant relationship between the input voltage and its speed. A KV value is often seen on a BrushLess DC (BLDC) motor. A KV value indicates the speed when 1 V is given without any loads. For example, 120 KV means the motor rotates at 120 rpm when 1 V is induced. Thus, a KV

value is one of the constants for a Permanent Magnet Synchronous Motor (PMSM) and it can be derived mathematically. A question is what happens to a PMSG. It can predict logically that in the reversed utilisation, a PMSG is capable of generating 1 V when the speed of 120 rpm is given. However, to verify the assumption, an experiment is done. A BLDC motor which has 600 KV is coupled as being driven, with a DC motor as a driver. And the BLDC motor outputs three-phase alternative currents. The currents that are rectified into a direct current are measured. The result is that the voltage is linear depending on the speed as assumed.

From the given and revealed information, MN8017-KV120 is selected as the PMSG. Its maximum power is 3.18 kW and surpasses the ICE's power slightly. Since buck-boost DC-DC converters can input 9 to 36 V (which is explained later), the maximum output voltage from the PMSG is limited to 36 V. In that case, $(120 * 36 =)$ 4320 rpm is calculated as the maximum speed for the PMSG (the actual speed can be fewer due to voltage drops as explained before). Because there is a suitable working range in the ICE, its maximum operation power is set to about 2 kW. And looking back at figure 21, a point close to 4000 rpm and 2 kW pass through the line of P_{max} at 9000 rpm with a 1.5 reduction ratio. Also considering the torque, the PMSG as a PMSM produces over 4 Nm torque when the power is 2 kW according to the specifications in [39]. The ICE might make 4.62 Nm torque shown in table 3 assuming the speed-power curve is linear and there is still a margin to compensate for the estimating deviation. Even though the ICE has different characteristics from the specifications such as the maximum power reaching 2.9 kW at 5000 rpm in the worst scenario, the chosen configurations can manage the undesired case without spending extra costs by sacrificing the speed (for instance, 2 kW at approximately 3500 rpm without the reduction). Therefore, MN8017-KV120 is selected as the PMSG and is capable of matching the ICE characteristics. For coupling with the ICE and PMSG, a timing belt and 1.5 reduction ratio pulleys are utilised due to their weight and cost advantages. An experiment is done to observe the torque transmitting behaviour between a PMSM and a PMSG as illustrated in figure 21 (a). 2GT timing belt and pulleys fixed with 3D printed PLA material holder is used. The experiment taught two tips. The first is to tighten enough the belt otherwise it leads to failure. The second is to loosen enough the belt or vibrations are produced which leads to

another failure. For the selection of the timing belt, some calculations based on the transmitting torque are done referring [40]. As a result, 5 mm HTD belt, 30 and 45 teeth 5M pulleys (1.5 reduction ratio) are chosen. Also, aluminium EN AW-7075 pulley holders shown in figure 21 (b) and (c) are manufactured originally. The one is designed to couple with an encoder and an electrical drill on the tip.

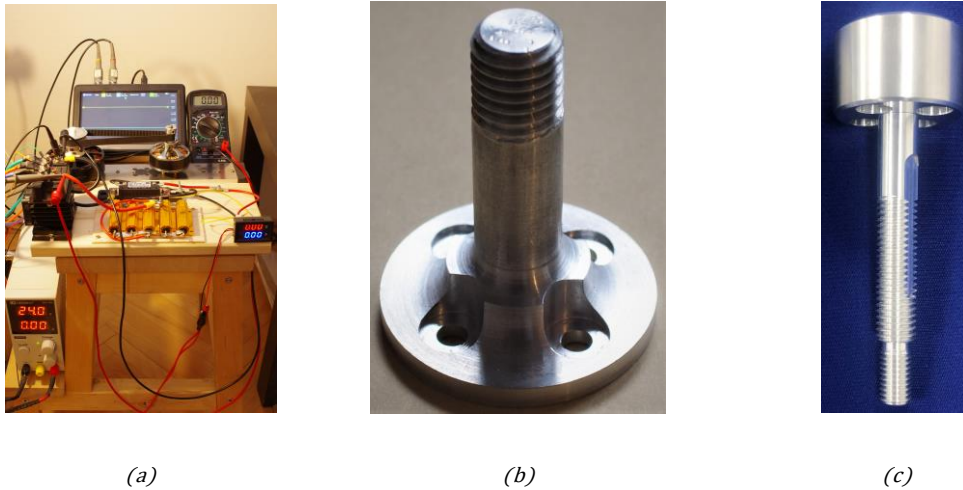


Figure 21 Torque transferring experiment, (a) setup, (b) and (c) originally manufactured parts

3.2.2 BLDC Motor and Propeller

BLDC motors (or PMSMs) are quite often used for MCs due to their simplicity, weight and efficiency merits. BLDC motors have parameters such as a KV value and suitable propeller sizes depending on their speed and torque characteristics. How the parameters affect BLDC motors from T-motor are bar-charted in figure 22. The comparisons are when the thrust of the motors is 2 kg with a 24 V supply. The data is brought from their manufacturer, T-motor and interpolated for estimating. Efficiency here means the ratio between the power and thrust. Both current (on the left with blue colour) and power/thrust ratio (on the right with orange colour) have a common y-axis. In each bar, the motor propeller's diameter, pitch, KV value and product name are written on the bottom. The current consumption of 5212 with a 16-inch propeller is around 12 A while U8 Lite with a 30-inch propeller consumes less than half. There are more facts and they are summarised simply in figure 23. The overview shows the relationships between efficiency (power/thrust ratio), KV value, propeller diameter and input voltage. The efficiency

decreases as the KV value increases (in the dotted line). Also, the efficiency increases as the propeller diameter and the input voltage increase (in the normal line). In general, a lower speed with a higher voltage leads to higher efficiency. By the way, propeller thrust increases by the square of the speed in general. High-efficient BLDC motors are expensive and U8 Lite costs 300 USD. By balancing high efficiency (power/thrust ratio) and price, MN6007II-320KV whose price is 130 USD, with 22-inch propellers is selected.

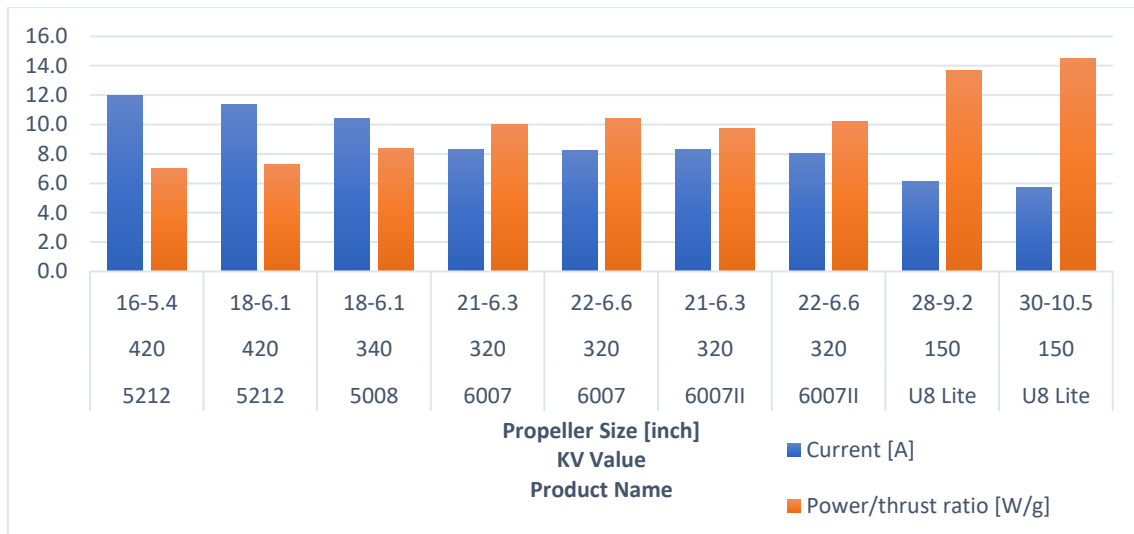


Figure 22 Comparison of T-motor products at 2 kg thrust with 24 V

For comparing the catalogue data in [39] and an experimental result, an experiment is set up. Instruments are the same motor (MN6007II-320KV), 22-inch diameter and 5.5-inch pitch propeller, an Electric Speed Controller (ESC) (EMAX BLheli-60A), and a power meter (WM150). Also, a thrust meter, which utilises a load cell, from Mayatech. The experiment setup is shown in figure 24 and the result is in figure 25. The x and y-axes represent speed and thrust respectively. The blue line with round markers is the measured data while the orange line with square markers is the catalogue data. A few things to notify are that the experimental propeller's pitch is slightly lower than another and the propeller geometry is different. Also, wind flow obstacles are not well focused. Therefore, this is not a perfect comparison but one can observe the behaviour. And the maximum measured thrust experimentally is around 3 kg due to some limitations. Thus, a second-order polynomial approximation is utilised for the forward prediction. Looking at the result, the measured one climbs up at a slower speed. In other words, it can produce a

higher thrust at a slower speed. The power and efficiency are not dealt with here but only the motor's characteristics and propeller's geometry. The equations are created from the curves and utilised in the next chapter.

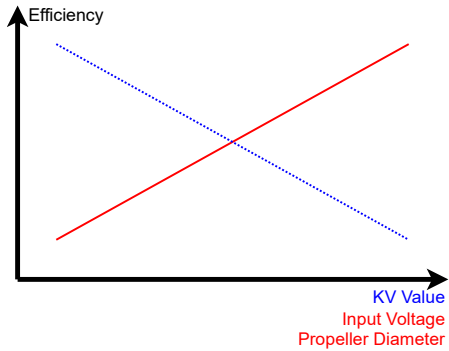


Figure 23 Motor efficiency dependences

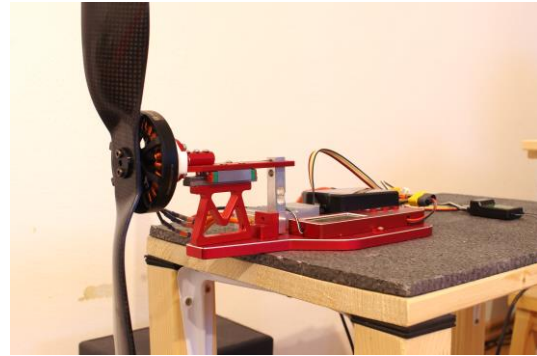


Figure 24 Thrust measurement setup

Experimental results related to motor and propeller efficiency are validated theoretically in [41]. According to that, enlarging propeller size and slowing the propeller speed for higher efficiency, lead to a loss of controllability and a variable pitch propeller is suggested to beat the difficulty.

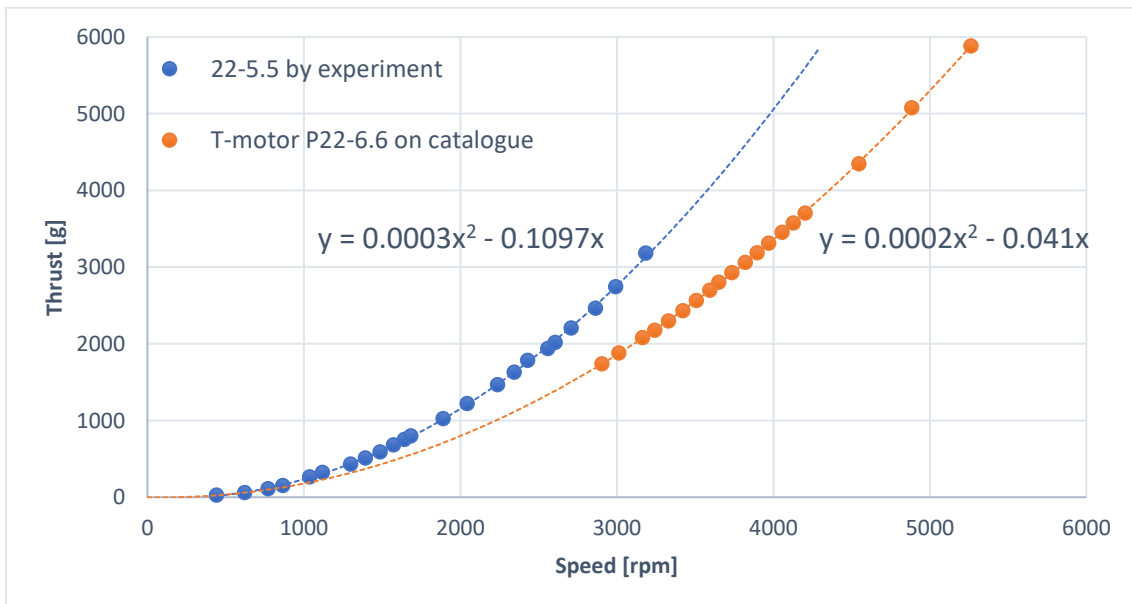


Figure 25 Thrust comparison between two propellers

3.2.3 ESC

ESCs are one of the most important parts of MCs because their efficiency can vary significantly. Also, there are various protocols for controlling an ESC [20] to improve its controllability. For the HMC, EMAX BLheli-40A for the thrust motors are selected since it is quite cost-friendly and easy configuration. An ESC switches on and off at least six transistors to generate three-phase currents. The switches' sequences are based on the Back Electromotive Force (BEMF) (for the sensorless method). Superposing the BEMF and input switched voltage produces sinusoidal or trapezoidal waveforms with sudden drops and rises which occurred due to the commutation periods [42]. For checking actual line voltage waveforms, an experiment is done and the comparison result is represented in figure 26. EMAX BLheli-60A waveforms (yellow) with speed sensor waveforms (blue) for lower speed (a) and higher speed (b). T-motor ALPHA 60A 6S waveforms for lower speed (c) and higher speed (d). The waveforms differ totally from EMAX BLheli-60A due to a high-efficient control algorithm [39].

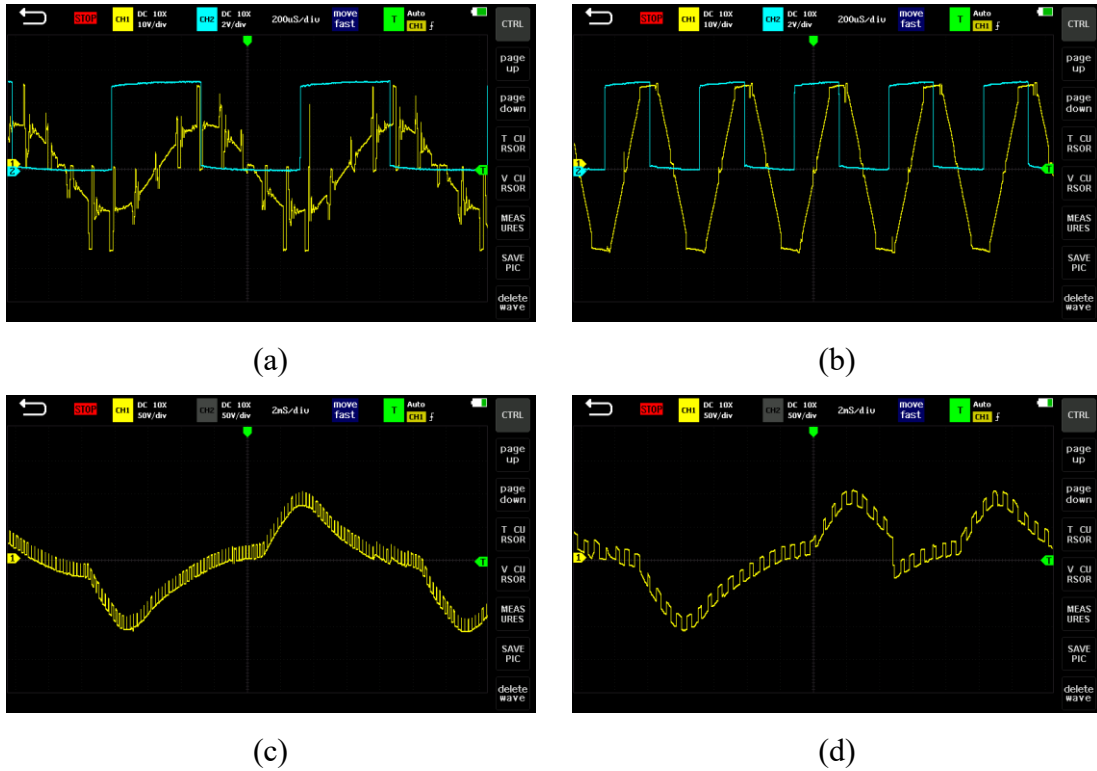


Figure 26 EMAX BLheli-80A waveforms (yellow) with speed sensor waveforms (blue), (a) for lower speed and (b) for higher speed. T-motor ALPHA 60A 6S waveforms, (c) for lower speed and (d) for higher speed.

Now, the actual efficiencies of both ESCs are the focus of curiosity. The comparisons of the ESCs are introduced in figure 27 and figure 28. The used instruments for the experiment are the BLDC motor (MN6007II-320KV), a 22-inch diameter and 5.5-inch pitch propeller, and the ESCs (ALPHA 60A 6S, EMAX BLheli-60A and EMAX BLheli-40A), a power meter (WM150) and thrust meter which utilises a load cell from Mayatech. The orange round markers are ALPHA 60A 6S, the green square markers are EMAX BLheli-60A, the yellow triangle markers are EMAX BLheli-40A and the brown x markers are FLAME 60A HV whose data is gained on the catalogue. In the first figure, the x and y-axes are thrust and power respectively. The markers are interpolated by second-order polynomial curves. It can be seen that the EMAX series are overlapped. ALPHA 60A 6S draws the line underneath them, and also, FLAME 60A HV locates at the bottommost among the four. In other words, the EMAX series are the worst efficient and the difference is around 80 W at 2 kg compared to the most efficient one. In addition, it is revealed that to produce 12 and 16 kg thrust by (eight of) the selected ESCs, almost 1.5 kW and over 2 kW powers each are required.

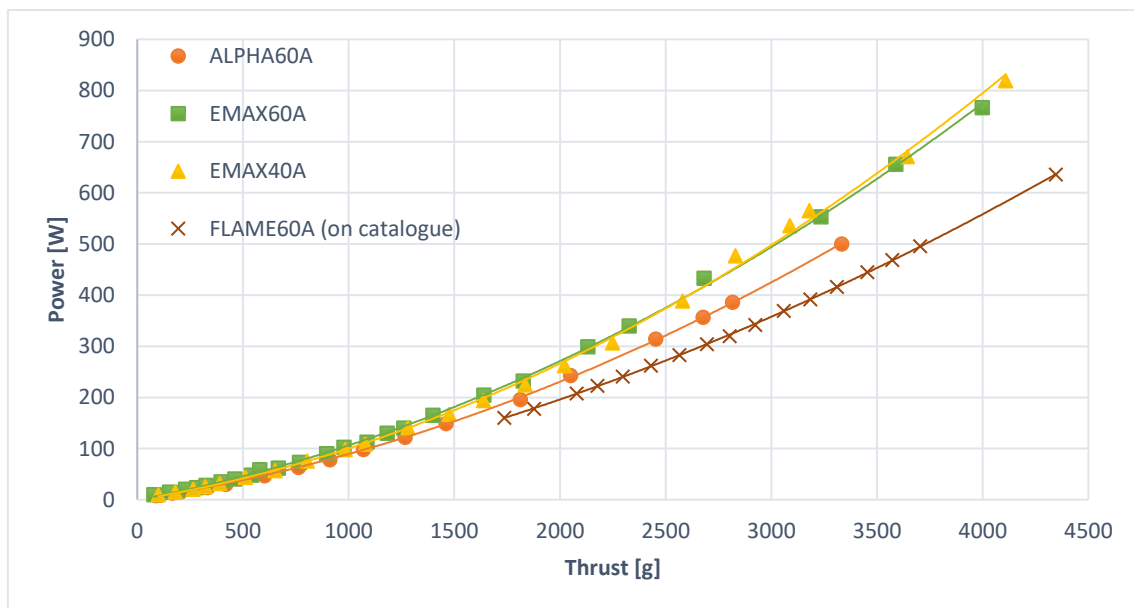


Figure 27 ESC power vs. thrust comparison

Regarding the last figure, the x and y-axes are thrust and power/thrust ratio respectively. There are bumps in each ESC (except FLAME 60A HV) at around 400 g of thrust. The maximum power/thrust ratio, about 14 g/W is taken by ALPHA 60A 6S. However, if

FLAME 60A HV is examined, it can be the greatest efficient one according to the trend in the figure. For the other two ESCs, the highest efficiencies stay at about 12 g/W and it implies almost 15 % lower than ALPHA 60A 6S. After passing the hills, all of the efficiencies descend gradually and they are almost linear against the thrust until certain points. ALPHA 60A 6S changes the steepness to more loosed at about 2000 g. The EMAX series have twice turning points to soften the steepness at around 1500 and 3000 g. Also, the point for FLAME 60A HV can be seen at approximately 2500 g. The ranking of the highest power/thrust ratio is not changed after the bump and FLAME 60A HV keeps its position. The EMAX series still overlap each other and significant differences cannot be found. Compared to the highest and lowest efficient ESCs, the difference is around 2 g/W at 2000 g which means the selected ESC, EMAX BLheli-40A has a 20 % lower power/thrust ratio than FLAME 60A HV. However, the cost of EMAX BLheli-40A is around 25 USD while ALPHA 60A 6S and FLAME 60A HV cost 70 and 100 USD respectively. Thus, again, EMAX BLheli-40A is chosen due to the economical reason and the relatively worse power/thrust ratio is acceptable according to the cost. For the best performance and power/thrust ratio of the MC, alternating those ESCs are the first step.

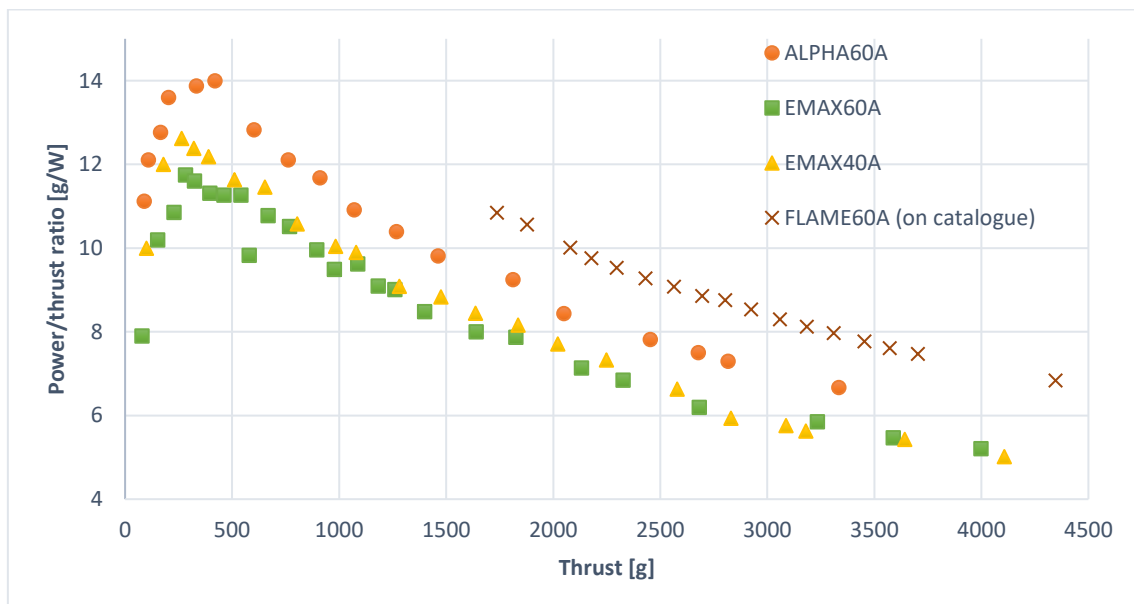


Figure 28 ESC power/thrust ratio vs. thrust comparison

3.2.4 Buck-Boost DC-DC Converter

Supplying stable power is an essential key for MCs to achieve agile manoeuvring and regulators or DC-DC converters can play the role. Since the main power voltage is 24 V and the estimated current is up to 90 A which generates 2.16 kW, three buck-boost DC-DC converters, XW-0936-24-720W are selected as the regulators. The reason why the buck-boost is applied is the ICE characteristics are not known and the input voltage range, 9 to 36 V can adjust the uncertainty. It indicates that the minimum and maximum PMSG speed is $(120 * 9 =)$ 1080 and $(120 * 36 =)$ 4320 rpm after the reduction. Thus, the ICE speeds, taking account of the reduction, are 1620 and 6480 rpm which suit the expected range (calculated in the previous pages). Also, the efficiency of DC-DC converters is not negligible for the MC. In general, chopper DC-DC converters have quite excellent efficiencies. Figure 29 indicates the characteristics maps for XW-0936-24-240W. The product whose rated current is 10 A, is slightly different in its rated current from the selected one, XW-0936-24-720W which has 30 A of the rated current. However, it is still possible to consider the behaviours as a reference. In the figure, x and y-axes are the input voltage and load current respectively. And the more yellowish region has better efficiency while the more blueish area has worse efficiency. It can be seen that 96 % or more efficiency at 6 A ranges between around 16 to 27 V. From the spot, the efficiency goes down gradually like an independent mountain. Therefore, the input voltage should be closer to the output voltage, 24 V and set ideally in the range, which is $(120 * 16 =)$ 1920 and $(120 * 27 =)$ 3240 rpm in speed for higher efficiency. Since the ICE's power is estimated to increase as the speed increases, the point at $(120 * 16 * 1.5 =)$ 2880 and $(120 * 27 * 1.5 =)$ 4860 rpm is approximately 1.4 and 2.4 kW respectively. Thus, the required power range for the MC from 1.5 to 2 kW is inside the high-efficient range by the DC-DC converter.

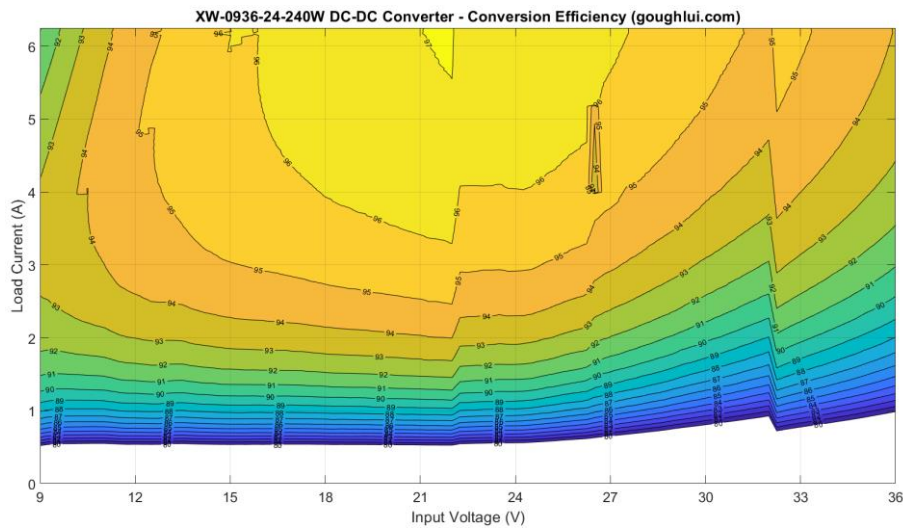


Figure 29 Efficiency map of DC-DC converter [43]

3.2.5 Battery Management System (BMS)

A BMS for sustaining a battery safe and healthy by monitoring, estimating and doing various processes. The main functions of a BMS are over-charge, over-discharge current protection, overheat prevention and cell-balancing. The selected BMS boards for the MC are Broodio BMS 6-13S 35A 3.7V due to the cost-friendly reason. In general, a BMS board is connected to a battery, charger and load as shown in figure 30 and the chosen one has three separated ports like the right one in the figure. All negative terminals from the components are connected to the BMS. Each port plays the role of switching for charging and discharging by monitoring the currents.

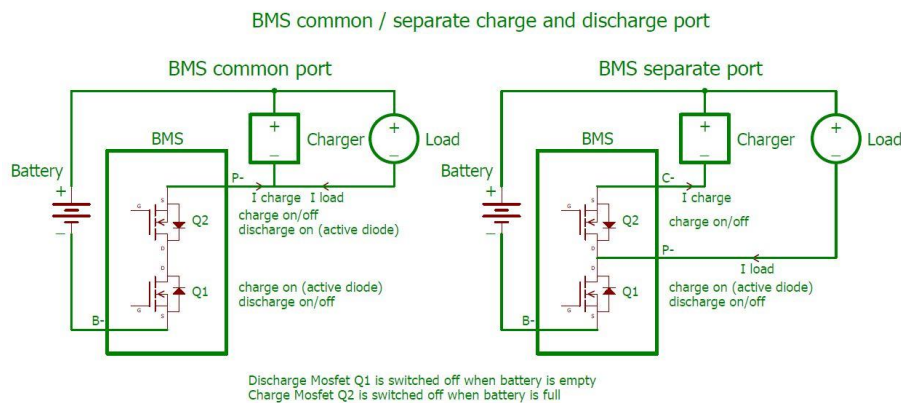


Figure 30 Two different BMS ports [44]

The selected BMS board has the mentioned basic functions but estimating ability. Thus, the estimation is done externally by utilising current and voltage sensors. Also, the battery discharge current can reach 200 A and the BMS board is not capable of handling such a high current, a bypass connection [36], is applied only for discharging. The charging current going to the battery is also limited at 1C charge which is 4 A each and 8 A in total through a DC-DC converter. There are two types of methods for balancing battery cells, passive and active cell balancing [45]. The selected BMS board is equipped with passive cell balancing. To observe the actual behaviour of the hybrid system of the PMSG unit including a BMS, a smaller scale-sized experiment is performed. The setup is illustrated in figure 31. The experiment validates that the designed hybrid system also can be operated. In addition, the behaviour of a LiPo battery is observed which leads to help in the next chapter, estimator.

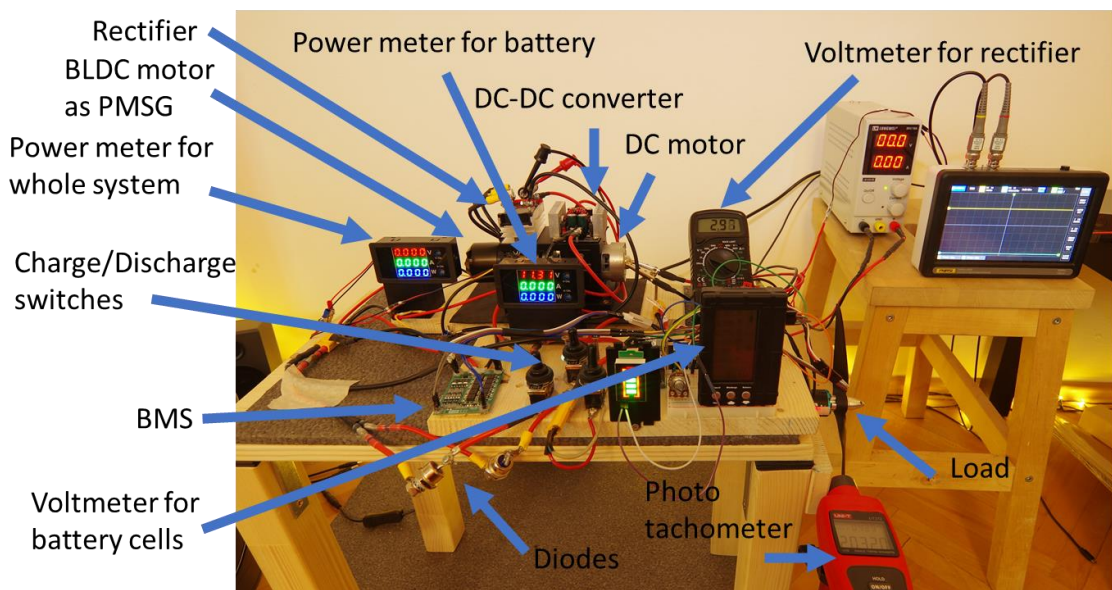


Figure 31 Small-scaled hybrid system experiment setup

CHAPTER 4

Design of Control Systems

In this chapter, control systems for the PMSG unit are designed on MATLAB/Simulink utilising the code generator function. The code generation is done in C language and the code is implemented on the GC, NUCLEO F767ZI directly. The chapter starts with an overview of the entire control system. Afterwards, each component's algorithm or principle is introduced. Parameters for the systems are listed in Appendix.

4.1 Overview

A simple overview of the control systems is represented in figure 32. Speed, voltage and current sensors measure the properties of several components. The GC outputs PWM signals to the two servomotors and the ICE throttle and choke are manipulated. Accordingly, the PMSG output power also varies and the speed, voltage and current are sensed. When starting the ICE, the relays (for the ICE starter), the ESC (for ICE starter) and MOSFETs (for the ICE starter) are controlled by the GC. For charging and discharging, the GC manipulates the MOSFETs (for charging and discharging) next to the batteries on both sides. Incoming and outgoing voltage and current towards and from the batteries are measured. Also, the speeds of eight thrust (BLDC) motors are measured. The FC and two transmitters send signals and operate the GC as well.

The PMSG unit control system integrates with the FC and sends data to it. Also, the gained and calculated data in the PMSG unit control system is designed to display in a GCS (but it is not validated in this thesis). A communication overview between devices is displayed in figure 33. The FC in the centre is manipulated by one of the two transmitters, AT10II by PWM signals. In the same way, the transmitter controls the GC on the bottom right. The GC sends data to the FC by UART communication. Also, another transmitter, FS-i6 controls the GC by PWM signals. The FC radio communicates with the GCS through the MAVLINK communication.

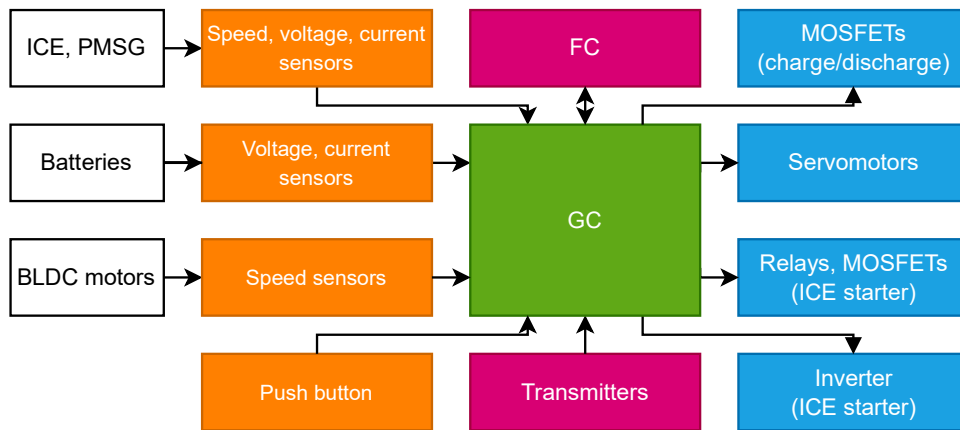


Figure 32 GC overview



Figure 33 Device communication overview

Overviews of the entire control systems on Simulink are revealed in figure 34 and figure 35. The control systems are divided into five stages by their colours. The first stage in purple colour is for inputs from various sensors and the two transmitters. There are four current sensor inputs, three voltage sensor inputs, nine speed-sensor inputs and seven PWM signal inputs in the area. In the next stage, those inputs are processed for smoothing.

The measured data from the inputs might have problems such as spike noise and deficits. For smoothing and repairing the data, FIR (moving average) filters are utilised. Some of the PWM signals are transformed into boolean signals. Also, some rate transition blocks are implemented in this section for limiting over-sampled frequency and reducing the computational load of the GC. In the third stage, various estimations based on revealed equations (in the previous chapter) are performed by utilising the processed data. Afterwards, the estimated values are sent to two controllers, the MOSFET logic controller and the throttle servomotor controller. The first controller is for the MOSFETs managing the charge and discharge. The other controller is for optimising the ICE's power (speed). At the end of the stages, various protocols are considered for emergencies and implemented. The throttle control is switchable to a manual mode that is manipulated by PWM signals from one of the transmitters directly. There is a block for starting the ICE as well. Finally, all eight signals are outputted as PWM signals for the MOSFETs, relays and an ESC. On the top of figure 35, there is a block for UART communication. Some important signals are gathered from various blocks, converted into UART protocol packets and they are sent to the FC.

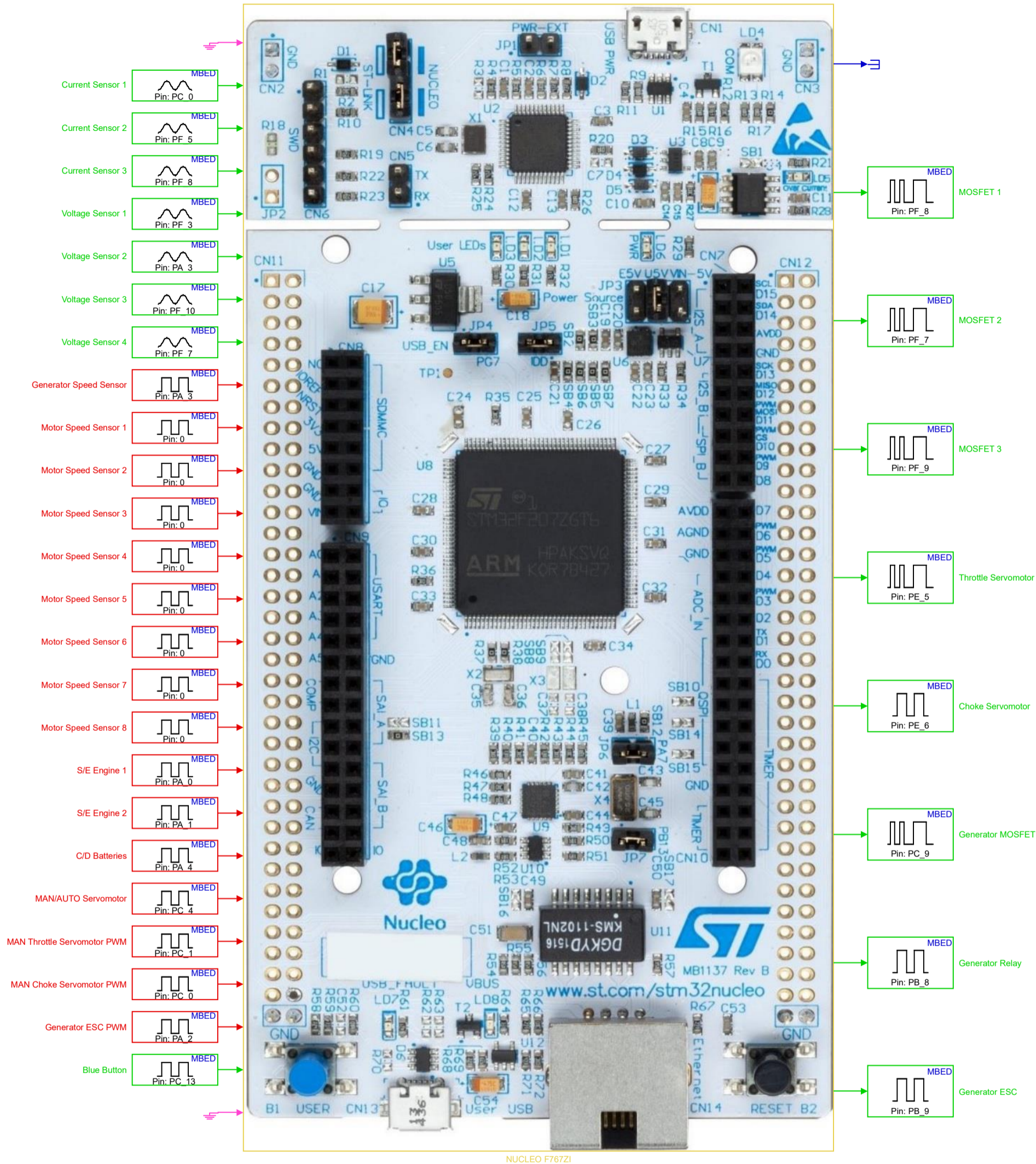


Figure 34 GC program overview I/O (Motor speed sensors are not assigned)

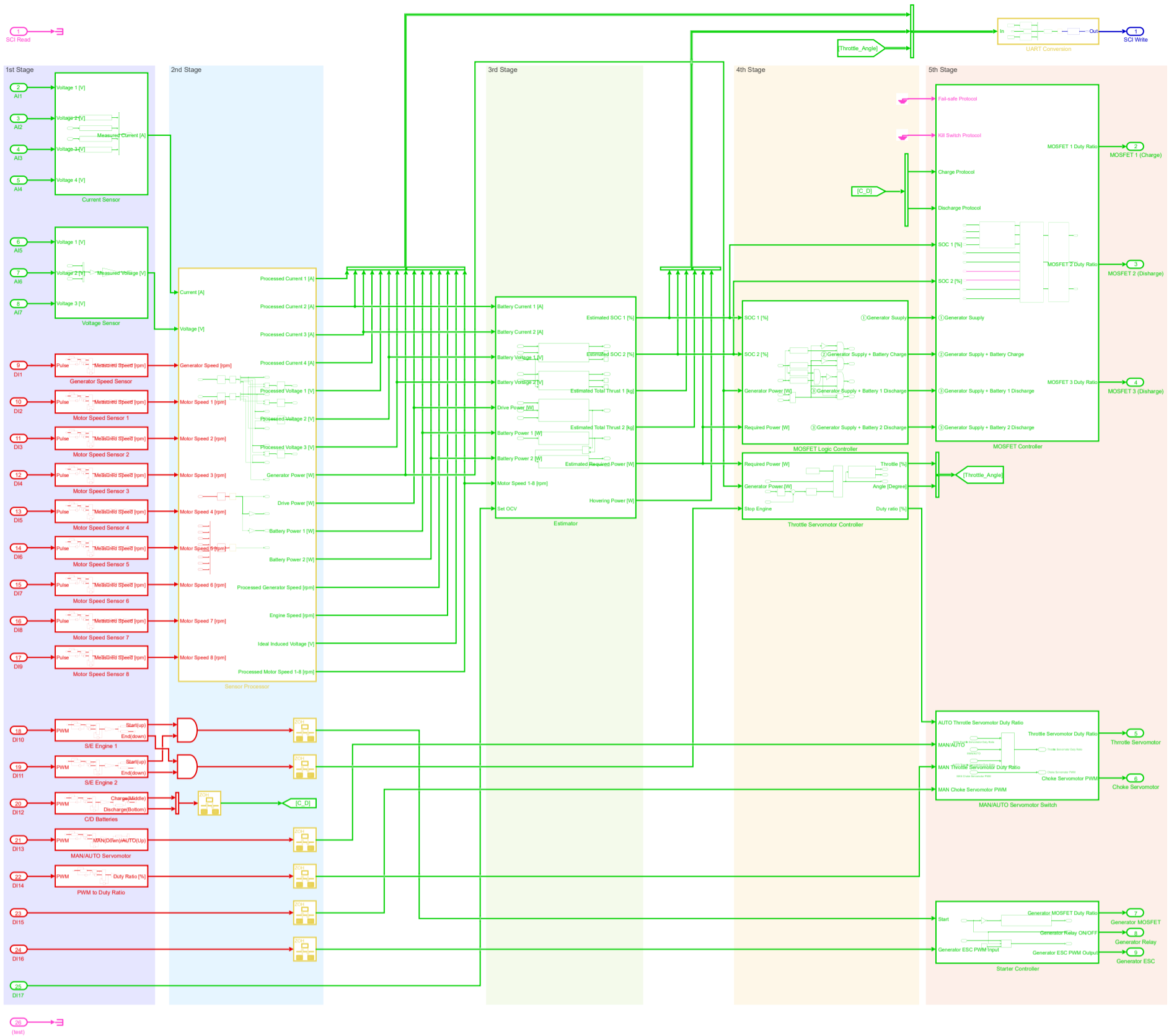


Figure 35 GC program overview

4.2 Algorithm

4.2.1 Input

The GC, NUCLEO F767ZI has 24ch 12-bit ADCs and 2ch 12-bit DACs. The input voltage range is from 0 to 3.3 V. The least significant bit is calculated as $3.3 \text{ V} / 4096 = 8.057 \cdot 10^{-4} \text{ V}$. The current sensor, HSTS016L outputs $2.5 \pm 0.625 \text{ V}$ depending on the direction and the magnitude of the flowing current up to 200 A. For instance, when 200 A flows in the positive direction, the voltage reaches 3.125 V. Meanwhile, when 10 A flows in the negative direction, the voltage is set to 2.188 V. The GC recognises the reference voltage (V_r) 3.3 V as 1 and 0 V as 0. Therefore, the program determining the current is indicated in figure 36. To avoid and compensate for deviations, some blocks are also added.

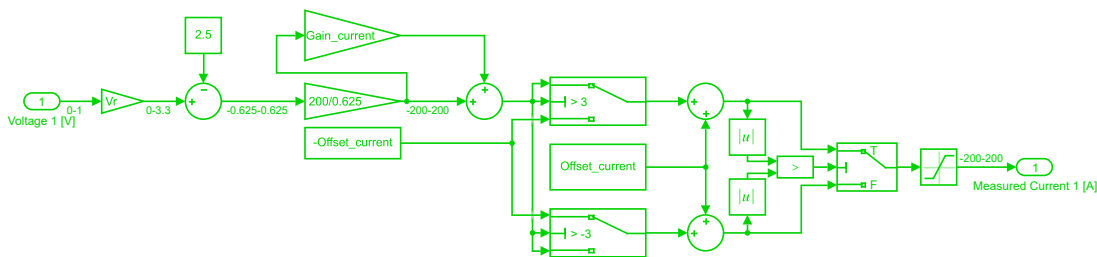


Figure 36 Current sensor program

For sensing the voltage of various terminals, voltage dividers are utilised as shown in the previous chapter. To derive the measuring voltage, the program illustrated in figure 37 is designed. R_1 and R_2 represent the resistances of the voltage divider. The output is in vector form here.

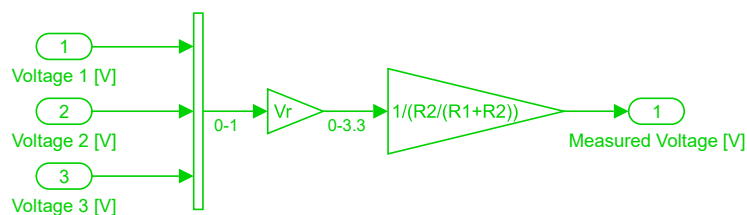
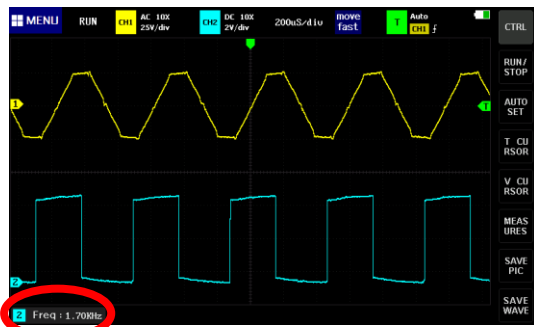


Figure 37 Voltage sensor program

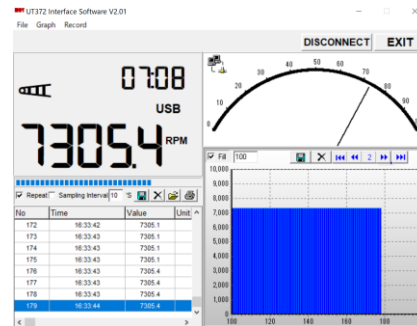
For speed sensing, the PMSG emit a three-phase sinusoidal voltage and BLDC motors give a three-phase trapezoidal voltage (at a certain speed) shown in figure 38 (a) because of the superposition of the BEMF and ESC voltage. And the speed sensor outputs pulse signals corresponding to the sinusoidal or trapezoidal voltages represented in the same figure. The red circle marker is the result of FFT and tells the frequency of the pulse. The speed of PMSG and BLDC motors can be calculated as an equation (2) below where n is the speed in [rpm], f is line voltage frequency in [Hz], and P is the number of poles.

$$n = \frac{f}{\frac{P}{2}} * 60 \quad (2)$$

In this case, the line frequency is 1.7 kHz and the number of poles is 28. Therefore, the result is 7286 rpm. For validating the speed, a photo tachometer, UT372 is utilised. The result is 7305 rpm which is indicated in figure 38 (b) and the values are almost the same. Thus, the emitted voltages from the PMSG and BLDC motors can be applied for speed sensing by the speed sensors and give a quite accurate result.



(a)



(b)

Figure 38 Oscilloscope (a) and photo tachometer (b) measurements

The speed sensing algorithm is illustrated in figure 39. The counter counts up while the pulse is raised. The maximum number of counting is kept until the next count-up. For the appropriate derivation of the count-up, the counter sampling time must be less than twice smaller than the pulse widths according to Nyquist–Shannon sampling theorem. However, it is better to have some margins for more accurate measuring. The estimated maximum frequency is 2 kHz. Therefore, the sampling frequency is set as 10 kHz which means the sampling time is five times smaller than the measuring period.

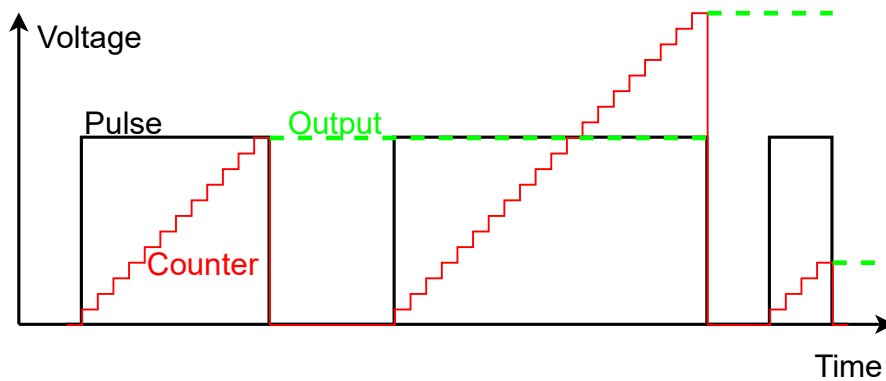


Figure 39 Speed sensor algorithm (actual duty ratio is 50 %)

The program is depicted in figure 40. It is maximally simplified and optimised for implementing onto the GC and actual operation. The algorithm and program are also applied to other programs in the GC.

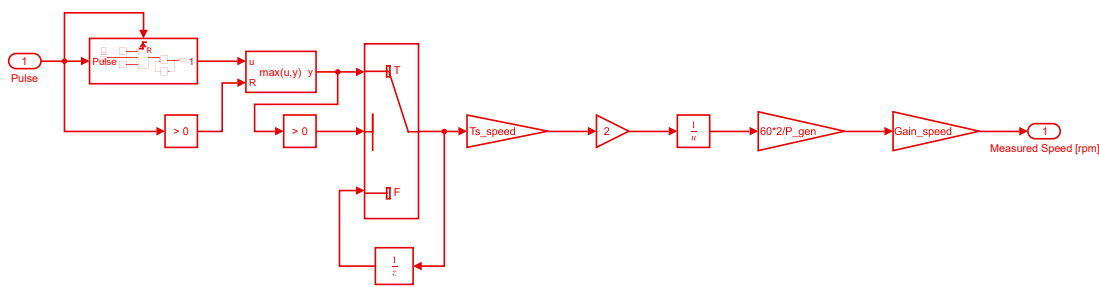


Figure 40 Speed sensor program (for generator)

4.2.2 Estimator

There are four estimators mainly. The one is for the battery capacities. The second and third are for the thrust from the power consumption and BLDC motor speeds respectively. The fourth is for the required power from the thrust. Considering the battery capacity estimation, a terminology, State Of Charge (SOC) is often used to represent the rest available capacity and it is expressed in equation (3) where $C_{releasable}$ is releasable battery capacity and C_{rated} is available battery capacity.

$$SOC = \frac{C_{releasable}}{C_{rated}} \quad (3)$$

However, estimating the releasable capacity is not simple due to Li-ion's or LiPo's non-linear characteristics as shown in figure 41, nominal current discharge on the top and various current discharge on the bottom. This is when a constant current flows and the battery rated capacity is 4 Ah. The graph is derived based on an ideal Lithium battery whose recovery time is 30 seconds. The X-axis and y-axis are time in minutes and voltage. Depending on the number of discharge currents, battery voltage varies remarkably.

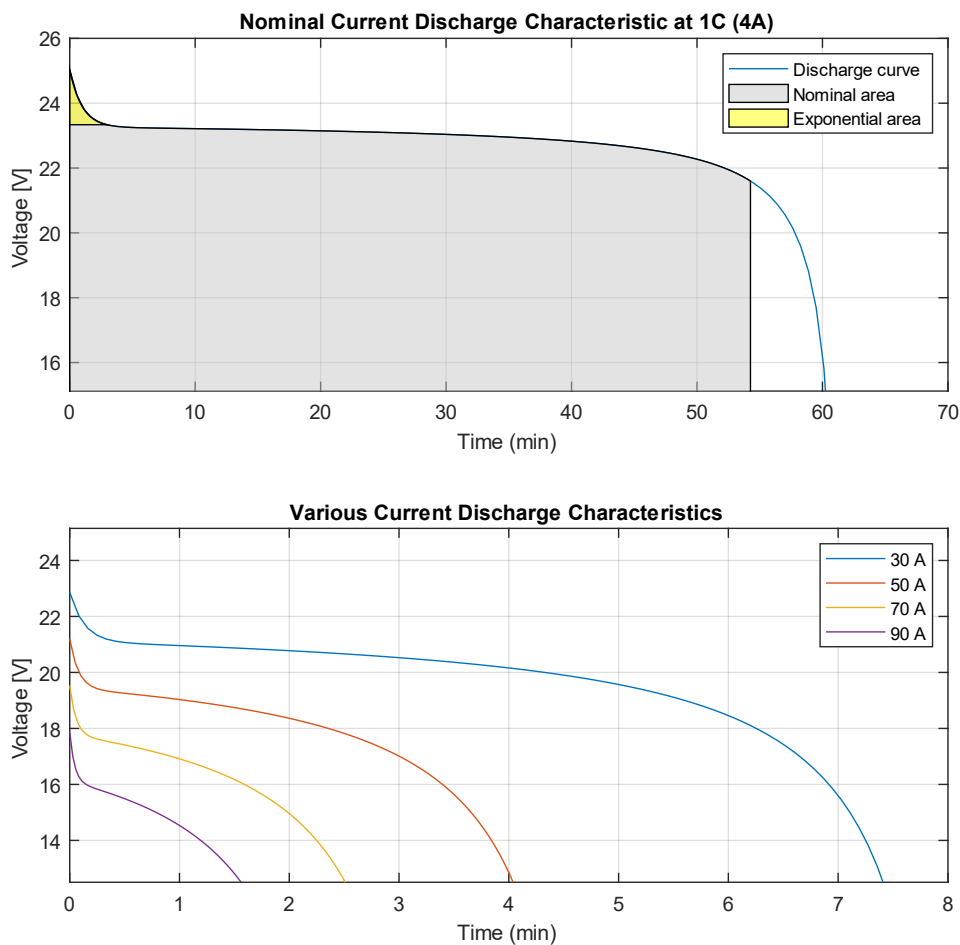


Figure 41 6-cell Lithium battery characteristics

There are various methods for SOC estimating [46] [47] [48] [49]. This time, a hybrid method is developed by combining the Open Circuit Voltage (OCV) method and the Coulomb Counting (CC) method. Equation (4) of the CC method is depicted below where t is time, t_0 is initial time, τ is counting time and i_{bat} is flowing current.

$$SOC(t) = SOC(t_0) - \frac{1}{C_{rated}} * \int_{t_0}^{t_0+\tau} i_{bat}(t)dt \quad (4)$$

The OCV method simply measures a battery voltage since the voltage is dependent on the SOC. Figure 42 represents a SOC non-linear curve depending on a voltage with linear approximations and their intersections for simplification. The CC method measures the coming and outgoing flow of currents to a battery and integrates it over time. However, the measurement deviation increases as time goes by [47]. The main frame of the hybrid method is the CC method. When initialising the SOC, the OCV method is utilised. Under 30 % of SOC, a variation of the voltage is remarkable. Thus, the OCV method is more reliable than before and both methods are fused like a complementary filter with an OCV reliability ratio. Therefore, the hybrid method can compensate and reduce the risks that each method has. The program is introduced in figure 43.

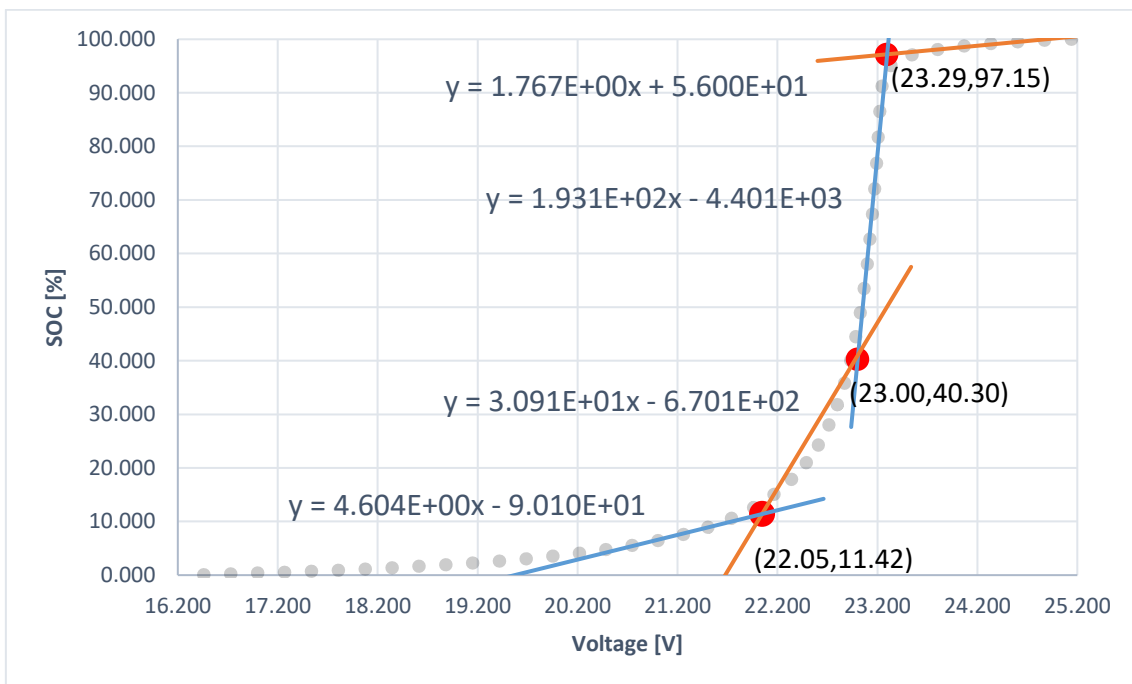


Figure 42 6-cell Lithium battery SOC estimation by OCV method (original curve... grey dot)

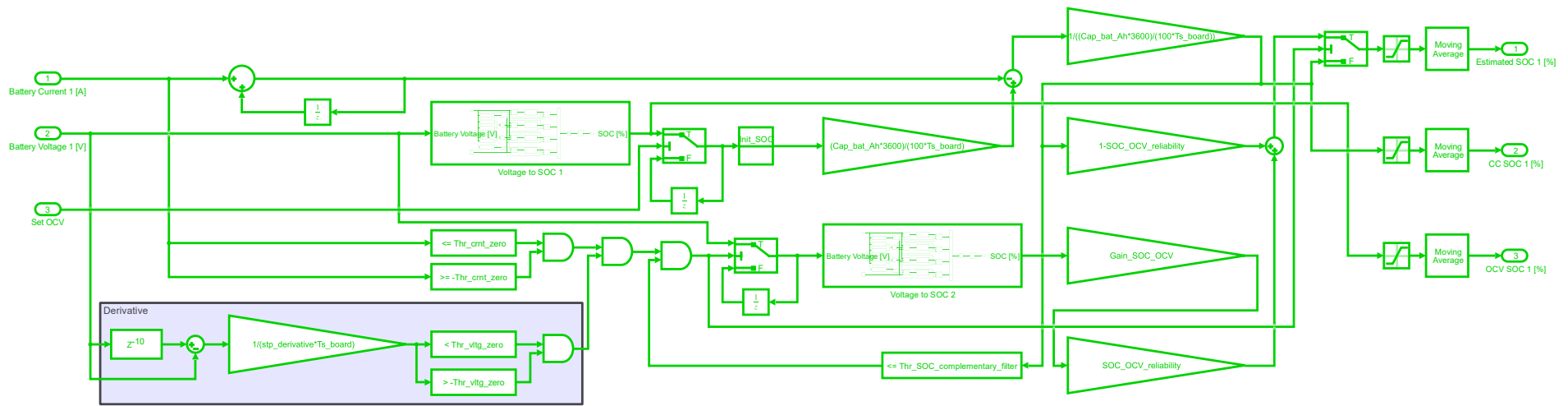


Figure 43 SOC estimation program (OCV, CC and their hybrid)

From the consumption power of the HMC, its thrust is estimated based on the equation derived in the previous chapter. The program is displayed in figure 44.

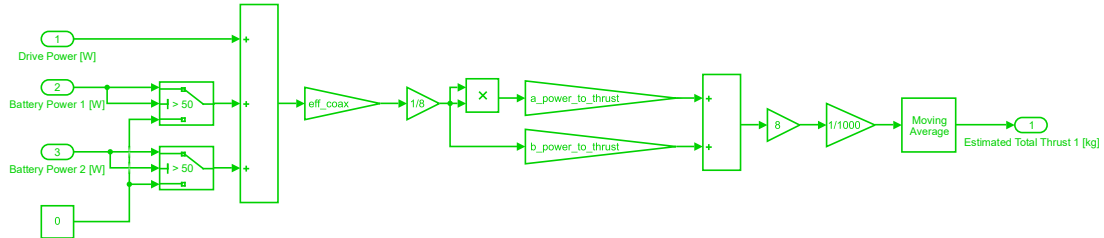


Figure 44 Thrust estimation program by power consumption

From the speeds of the BLDC motors, its thrust is estimated based on the equation derived in the previous chapter. The program is indicated in figure 45.

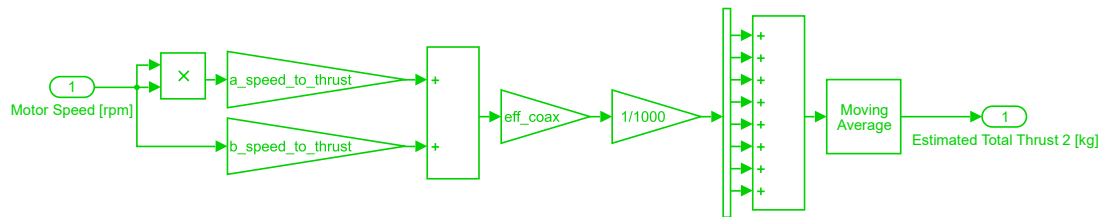


Figure 45 Thrust estimation program by thrust motor speeds

From the estimated thrust, its required power is estimated based on the equation derived in the previous chapter. The program is revealed in figure 46. The minimum required power is always calculated based on the set body weight.

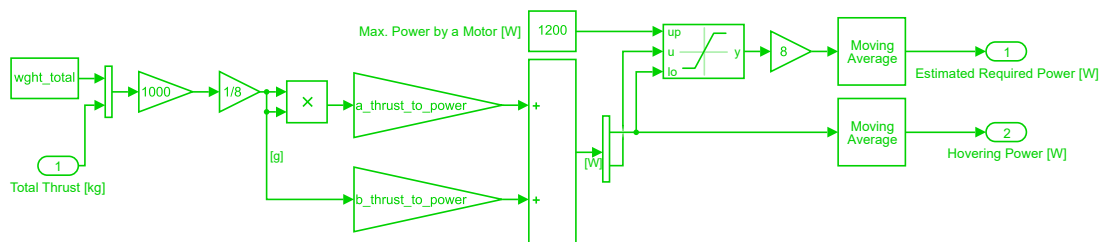


Figure 46 Required power estimation program by propeller thrusts

4.2.3 Logic Controller

A logic controller is selected for quick charging and discharging of the batteries. And it is a good combination with MOSFETs. The logic controller is designed based on a flowchart in figure 47. Firstly, the generator power is checked if it is over the required power. After that, all of the batteries' capacities are checked. The next processes are chosen depending on the capacities. The loop never ends and keep working for safety reason. And this is a reason why the controller is independent. The program is represented in figure 48.

- ① Generator Supply
- ② Generator Supply + Battery Charge
- ③ Generator Supply + Battery Discharge

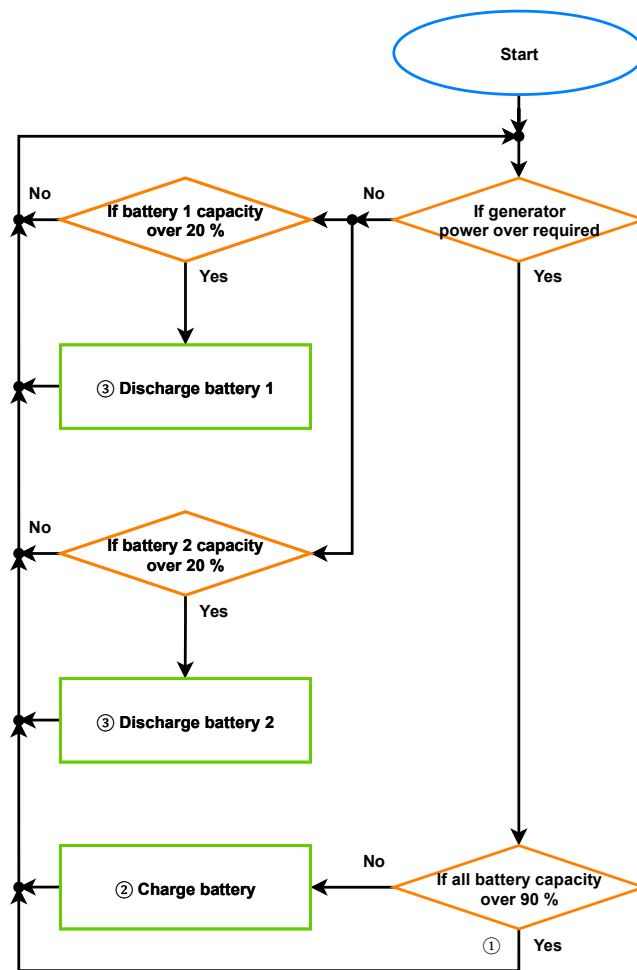


Figure 47 MOSFET logic controller flowchart

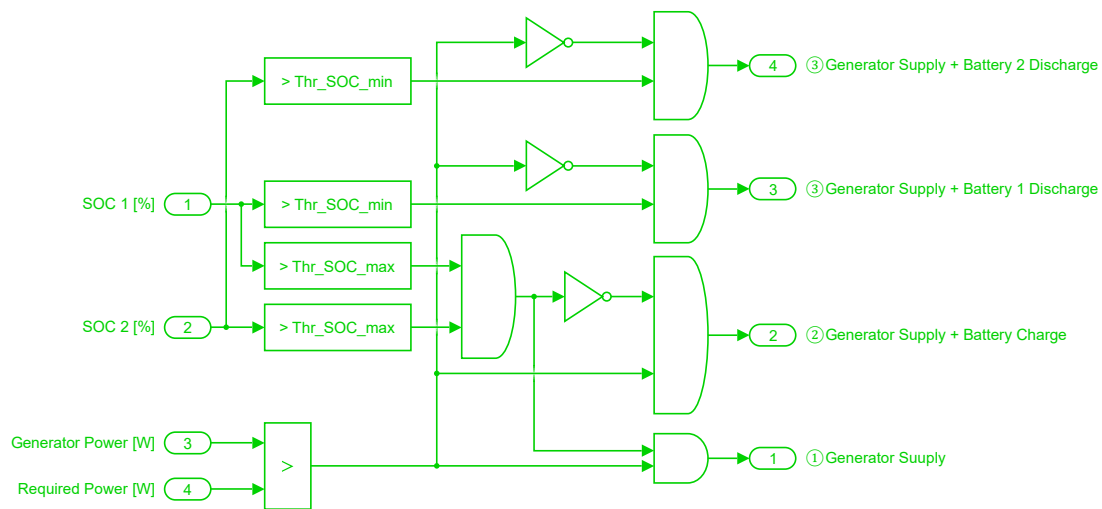


Figure 48 MOSFET logic controller program

4.2.4 PID Controller

A PID controller is selected for optimising the ICE power to meet the required power. In other words, the method is named the power tracking method. It can keep high efficiency and save fuel consumption. Since the ICE power does not vary suddenly, a PID controller is a good option. For the selection of PID controllers, there are some considerations, A velocity (also called incremental) form PID controller is a modified PID controller. It suits discrete-time and has the advantage that it does not require an anti-windup function externally [50] [51]. There is also an applied controller, 2-DoF or PI-D controller in the velocity form [52]. For this system, a normal parallel PID controller is utilised since the performance is quite enough and of its simplicity. For the anti-windup, the clamping method is applied to the controller.

Regarding digital PID gain parameters, they can be determined by the Ziegler-Nichols method even in the same as continuous-time PID gain parameters [53]. However, CHR set-point tracking method with 0 % overshoot [54] is chosen because less overshoot is more important than faster speed. Also, the plant is estimated as a first-order system with a time delay and is a transfer function whose input is the engine throttle angle (controlled by servomotor and PWM signal) and output is generator power. The filter coefficient (the

order of the filter) for the derivative part, N is set arbitrary. The parameters are listed in Appendix.

Equation (5) represents the parallel PID controller in discrete-time [55]. Equation (6) is an approximation method in the discretion for the integral and derivative parts and it is the trapezoidal method [55].

$$C_{par}(z) = K_p + K_i\alpha(z) + K_d \left[\frac{N}{1 + N\beta(z)} \right] \quad (5)$$

$$\alpha(z) = \beta(z) = \frac{T_s z + 1}{2 z - 1} \quad (6)$$

The program is shown in figure 49. The initial condition block is for breaking the algebraic loop. When stopping the ICE, a value for throttling to zero is sent.

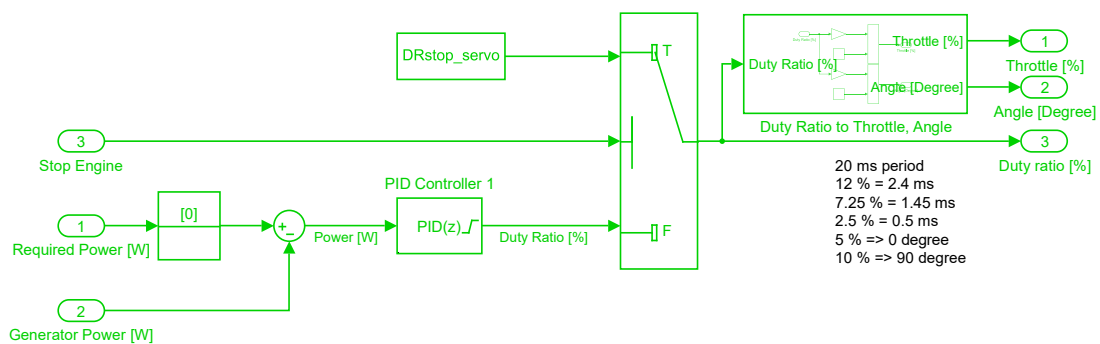


Figure 49 Thrust PID controller

4.2.5 Output

Figure 50 displays a program for UART conversion. The input reads values gathered from various blocks and it is sandwiched by the header and the terminator. When outputting, the data is converted into a serial form.

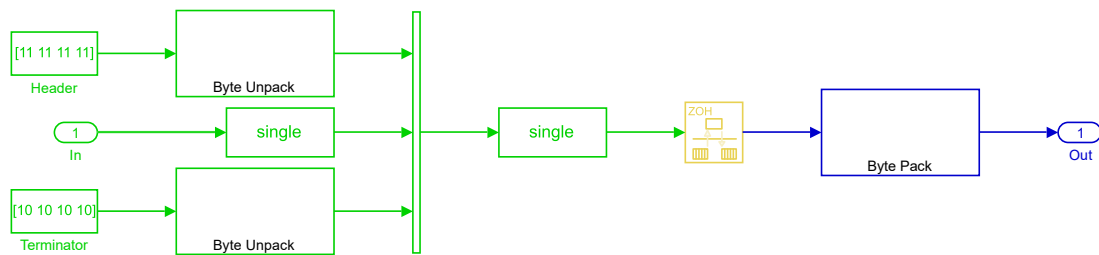


Figure 50 UART conversion program

The outputs from the GC board are mainly PWM signals for the MOSFETs and pulse signals for the relays. Those signals are generated by specific blocks on Simulink because manual generation of the signals can cause a small deviation in the signals. The program is illustrated in figure 51. It has a matrix form with indications D and C for discharging and charging respectively. M implies the MOSFET and 1 is for charging. 2 and 3 are for discharging. In addition, four emergency protocols are designed for avoiding undesired incidents. The protocols for manual charging and discharging of the batteries are operated by the transmitters. Fail-safe and kill switch protocols are also implemented for the future-use and are operated by the FC.

CHAPTER 5

Experimental Validations

In this chapter, the designed HMC body, the PMSG unit, the designed power electronics block connections and the designed control systems are constructed, implemented and validated experimentally. Also, improvements and feedback from the preliminary designs are suggested.

5.1 Constructed HMC

Figure 52, 53 and 54 show the PMSG unit and the constructed HMC respectively. They all are based on the introduced designs and are still in progress (missing parts, not wired nor configured completely). The components in those figures are indicated below.

1. PMSG unit
2. Thrust motor with propeller
3. ESC
4. Fuel tank
5. Skid
6. Foldable arm
7. Multi-layered plates
8. ICE with pulley
9. PMSG with pulley
10. Timing belt

11. Coupling for encoder
12. Servomotors
13. Encoder
14. Reinforcing pillar
15. Ignitor
16. (Bottom) layer with dumpers for DC-DC converters, rectifier and capacitor
17. Layer for brain electronics such as GC or FC
18. Layer for PDB, batteries and other power electronics
19. Layer for various electronics
20. (Top) layer for communication electronics

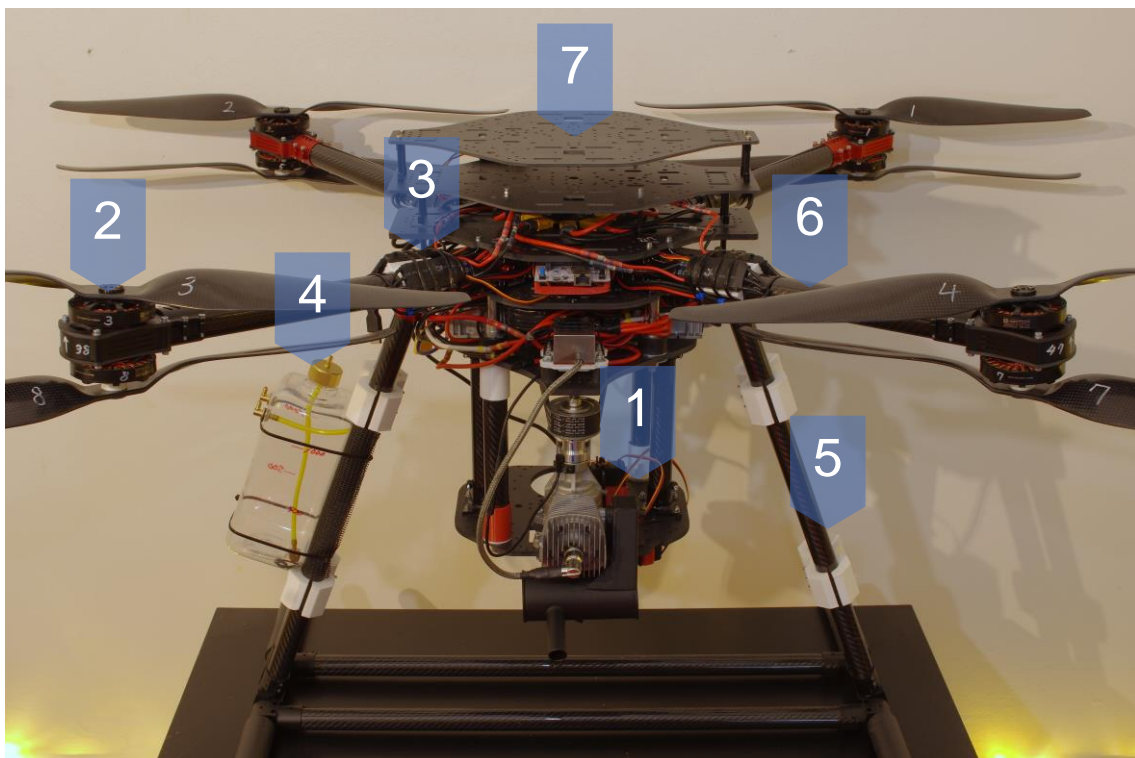
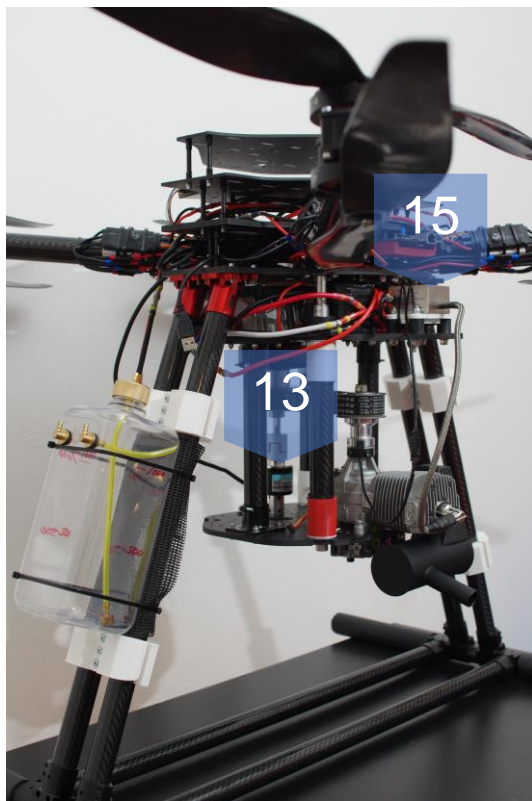
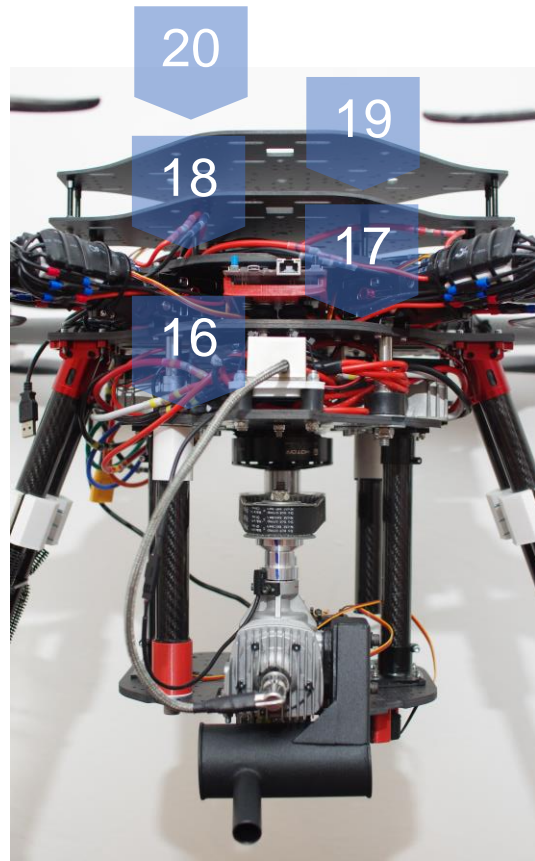


Figure 52 Constructed HMC 1



(a)



(b)

Figure 53 Constructed HMC 2

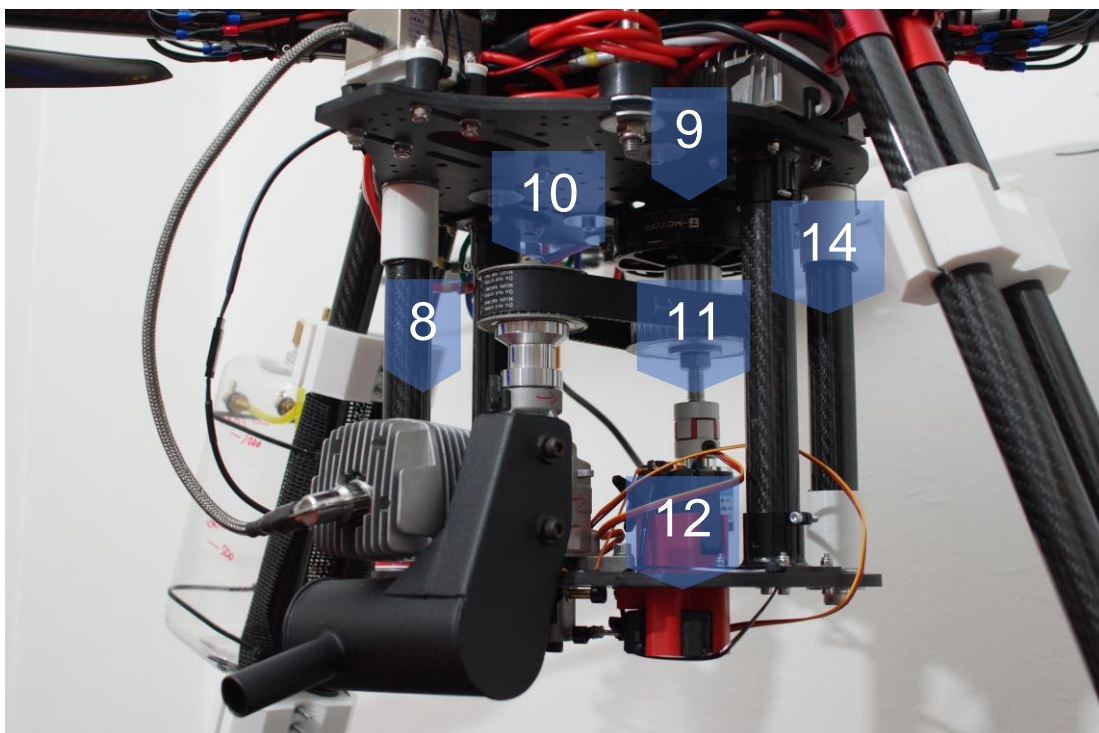


Figure 54 Constructed HMC 3

5.2 PMSG Unit without GC

To validate the PMSG unit, five experiments are done and three remarkable results are introduced here. The first one is when starting the ICE by the PMSG and the ESC (all parts are listed in the previous chapter). The setup is named the 1st PMSG unit and is indicated in figure 55 (a). The ICE and the PMSG are mounted on different plates. The result is that the ESC is not able to rotate the PMSG properly due to the ICE's torque variation that occurred by compression and expansion cycles. To solve the problem, a motor controller, Odrive is suggested to add to the power electronics design instead of the ESC. The driver is capable of various control including speed control utilising a rotary encoder and it might overcome the difficulty. Also, the ESC is burnt due to a short circuit as in figure 55 (b). Accidentally, the ESC and the rectifier are connected without any isolators. Therefore, a measure is taken and relays and MOSFETs as isolators are added to the block connection design.

Also, another doubt appears that if the PMSG speeds up over the ESC driving speed, the ESC would be destroyed. To clarify it, another experiment is performed and the setup is depicted in figure 55 (c). A BLDC motor (MN6007II) is run by an ESC (EMAX BLheli-40A) and an electric drill (POWEB1510). First, the ESC control the motor speeding up until a certain point. Second, the electric drill attached to the motor speeds up exceeding the speed at the same time. The result is that the ESC has no problem and is not destroyed under the condition, that both speeds are lower than the ESC's maximum operatable speed with no load. However, for confirming safety, more validation must be done by looking into the ESC's firmware and the program in case of utilising an ESC.

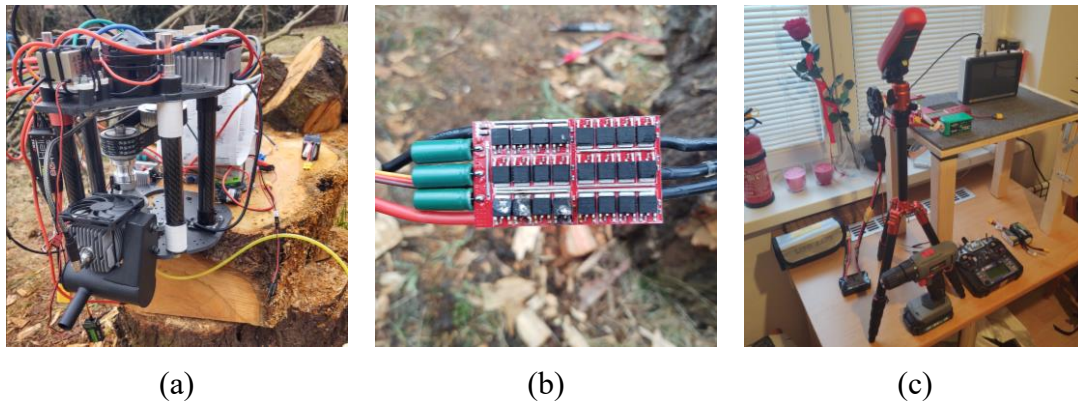


Figure 55 1st PMSG unit (a), burnt ESC as ICE starter (b) and experiment setup (c)

The second experiment is when starting the ICE with an electric drill (BOSCH AdvancedImpact 900) instead. The setup is named the 2nd PMSG unit and is displayed in figure 56 (a). The pulley holder shaft is mounted with a hex-nut for transferring the torque from the drill through a right-angle adapter. The result is that the adapter is worn and destroyed due to huge vibrations and the torque that the PMSG unit produces as represented in figure 56 (b). Also, the related parts are deformed as depicted in figure 56 (c). Thus, the setup is modified to access the shaft directly transferring the torque from the drill and it is introduced in the next experiment.

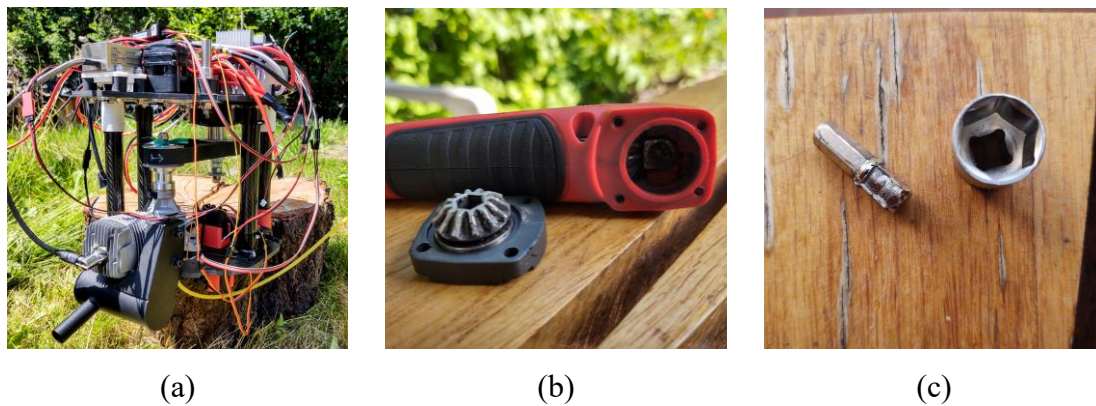


Figure 56 2nd PMSG unit (a), worn right-angle adapter (b) and deformed tools (c)

The third experiment starts by running the ICE with a propeller to realise and adjust the ICE configuration. The setup is indicated in figure 57 (a) and it works as it should. After the confirmation, the 3rd PMSG unit is tested and its setup is illustrated in figure 57 (b). The ICE and the PMSG are mounted on the same plate. The setup configuration enables direct access to the shaft for transferring the torque from the electric drill. In addition, the timing belt is altered to a shorter one to tighten the tension. The result is that bolts holding

the pulley holder are sheared, loosened and unbolted. They are occurred by exceeding the allowance torque, vibration and radical mechanical designs respectively. The moment that the part is destroyed is captured in figure 57 (c). This is after around 5 seconds when the ICE starts running. During the run, any abnormal symptoms are not seen but vibrations are significant to observe. When the moment comes, the pulley is blown off with the belt. Meanwhile, the ICE and the PMSG just remain fixed with a few scratches. The damaged bolts and pulley holder are revealed in figure 57 (d) and (e).

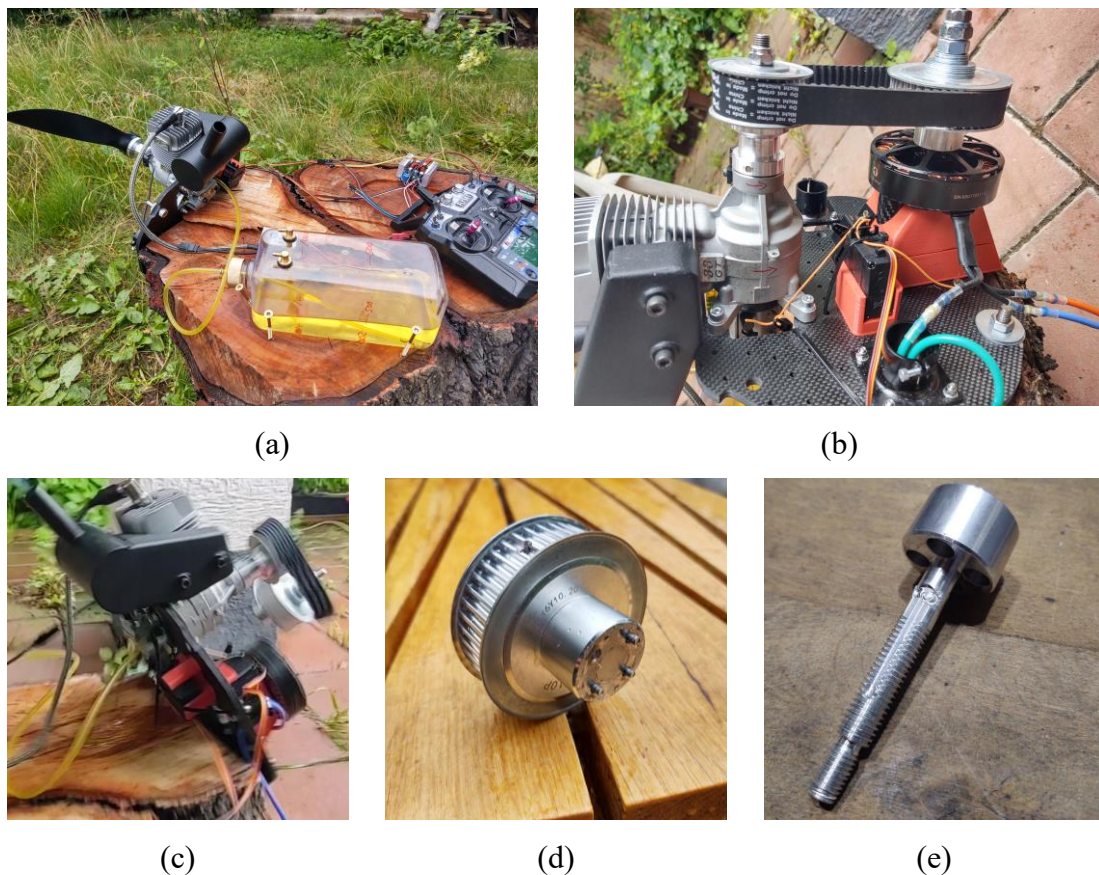


Figure 57 ICE with a propeller (a), 3rd PMSG unit (b), a moment when the new PMSG unit is destroyed (c), damage to bolts (d) and damage to pulley holder (e)

5.3 Control Systems with Electronics

For validating the designed control systems, they are divided individually and implemented on the GC, NUCLEO F767ZI through MATLAB/Simulink code generator with C language. The GC is equipped with some electronics, a current sensor, a voltage

sensor, a speed sensor, a receiver, a servomotor and a BMS. Each control system with each electronics is tested respectively.

The first validation is current sensing. Input flowing current is supplied from a power supply and connected to a resistor. The current is manipulated to vary and the maximum current is limited to 10 A by the power supply. A current sensor (listed in the parts list) utilises a hall-effect detection method and the power cable passes through the sensor. The data acquisition result from the sensor is depicted in figure 58 on the top with its amplitude (frequency) spectrum at the bottom. The x-axes are time in seconds and frequency in hertz while the y-axes are current in ampere and amplitude respectively. The sensor follows it moderately. However, plenty of spikes and noises can be seen at the same time. The largest current reaches 150 A while it should be less than 10 A. By analysing the data, a uniform noise is found to exist. A low-pass filter (LPF) is designed to eliminate the noise.

Its magnitude and phase response characteristics are represented in figure 58 on the bottom, whose blue colour indicates the magnitude while orange colour means the phase. The x-axis is the frequency in hertz while the y-axes are magnitude in decibel and phase in radians respectively. It is an equiripple FIR filter with 50 orders and its cutoff frequency is around 0.91 Hz.

After applying the LPF, moving average filters (MAF) whose window length (WLs) are 5 and 50 and their combinations, the results are introduced in figure 59 on the top. A remarkable range of the data is zoomed on at the bottom. The MAFs have excessive zig-zag lines. The spikes remain in the LPF. Meanwhile, one of the MAF and LPF combinations with WL 50 has a delayed response. Therefore, another combination with WL 5 is suitable for the current sensor among those filters.

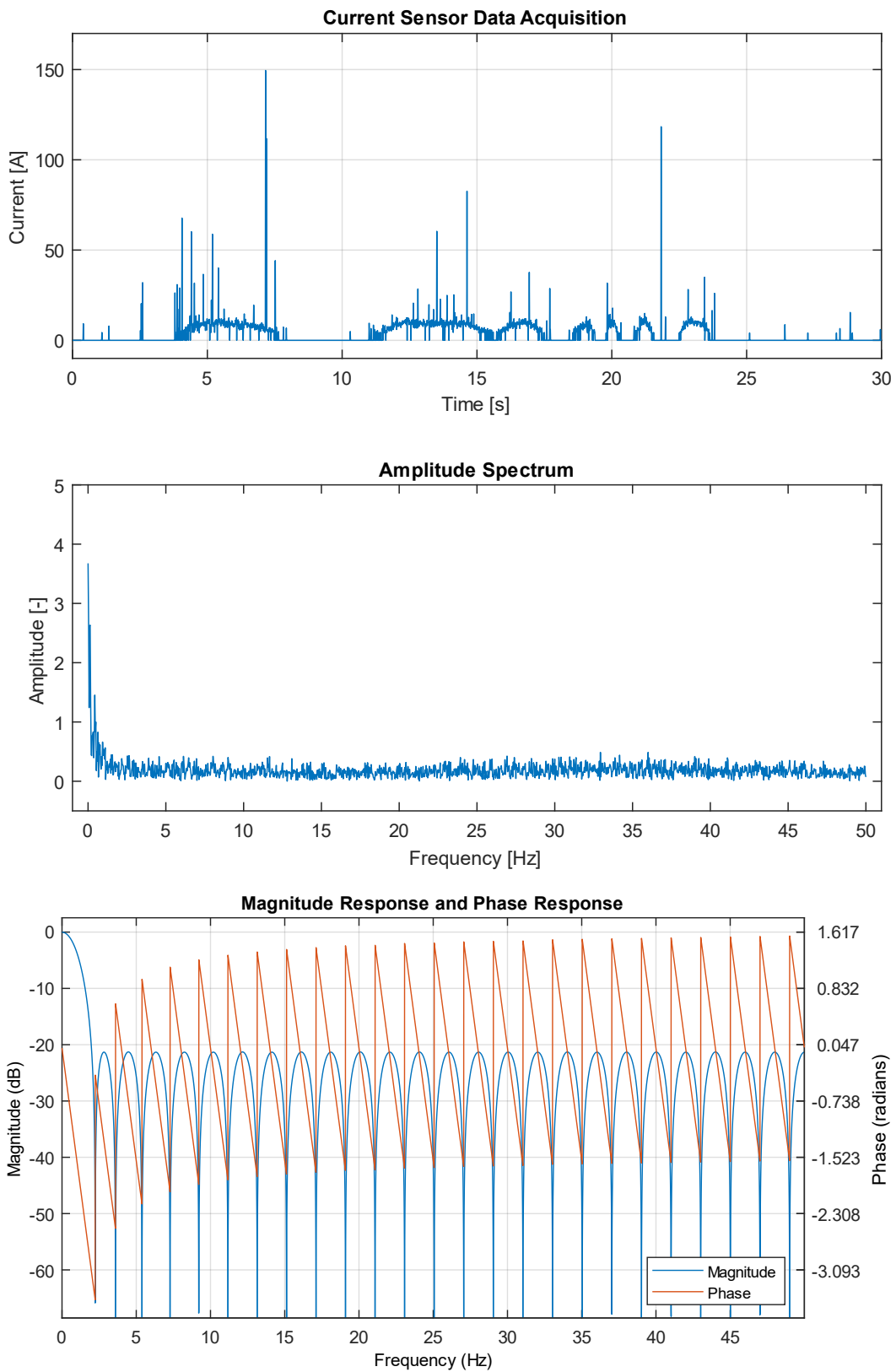


Figure 58 Current sensor data acquisition (top), frequency spectrum (middle) and designed low-pass filter characteristics (bottom)

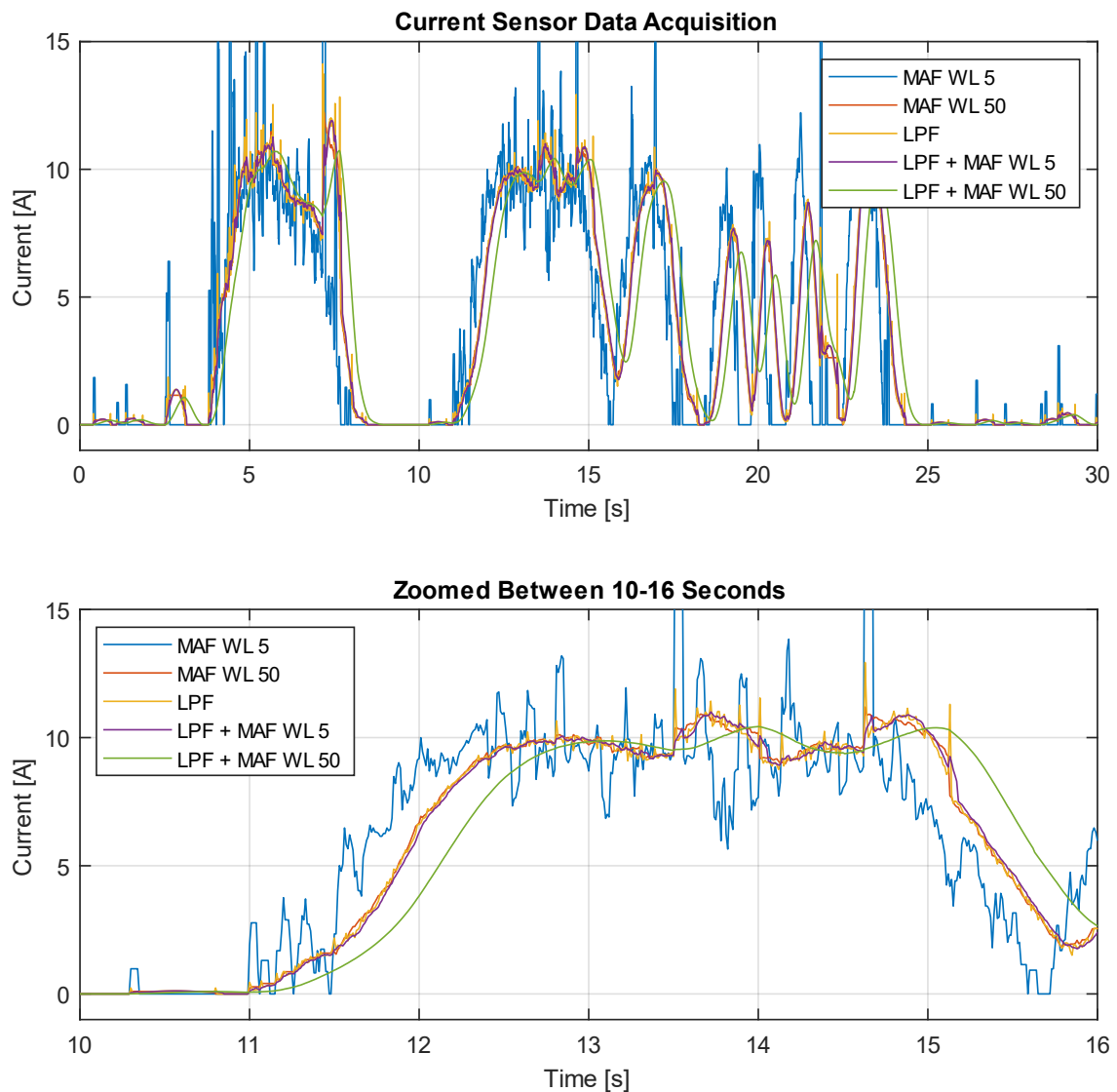


Figure 59 Current sensor data acquisitions with filters (top) and zoomed view (bottom)

The second validation is voltage sensing. A power supply is connected to a series of resistors as designed. And the divided voltage is read by the GC and is calculated as the original voltage. The data acquisition result from the sensor is illustrated in figure 60 on the top with its amplitude (frequency) spectrum in the middle and the zoomed view on the bottom. The x-axes are time in seconds and frequency in hertz while the y-axes are voltage in volt and amplitude respectively. Compared to the current data, spikes and noises are quite less even considering the spectrum analysis. In the same way as the current sensor, the filters are applied.

The results are shown in figure 61 on the top and a remarkable range of the data is zoomed on at the bottom. They all are quite smooth, meanwhile, some time delays and amplitude attenuations are seen in some filters. Taking into account the properties, the MAF WL 5 seems suitable for the voltage sensor.

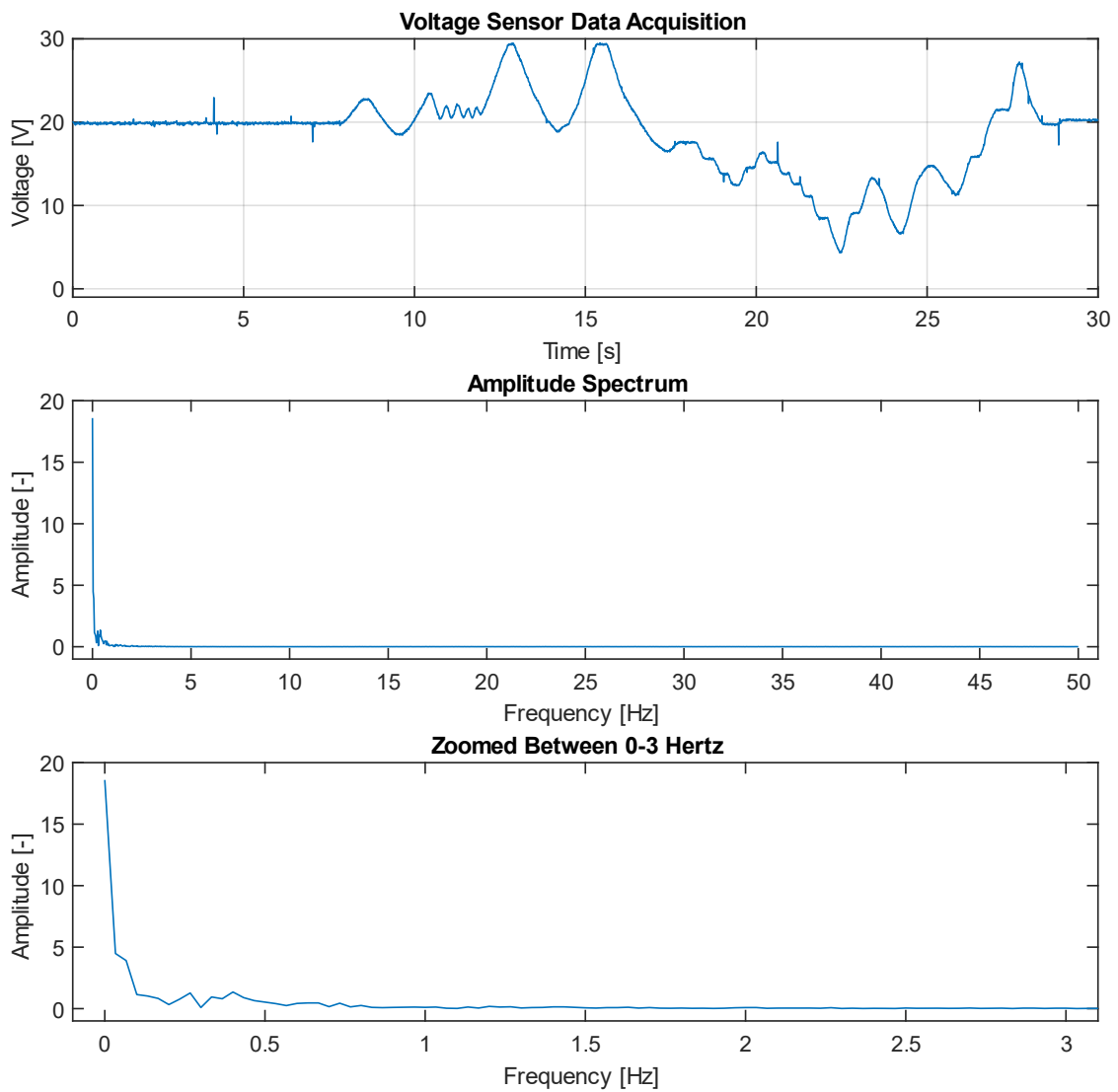


Figure 60 Voltage sensor data acquisition (top), frequency spectrum (middle) and zoomed view (bottom)

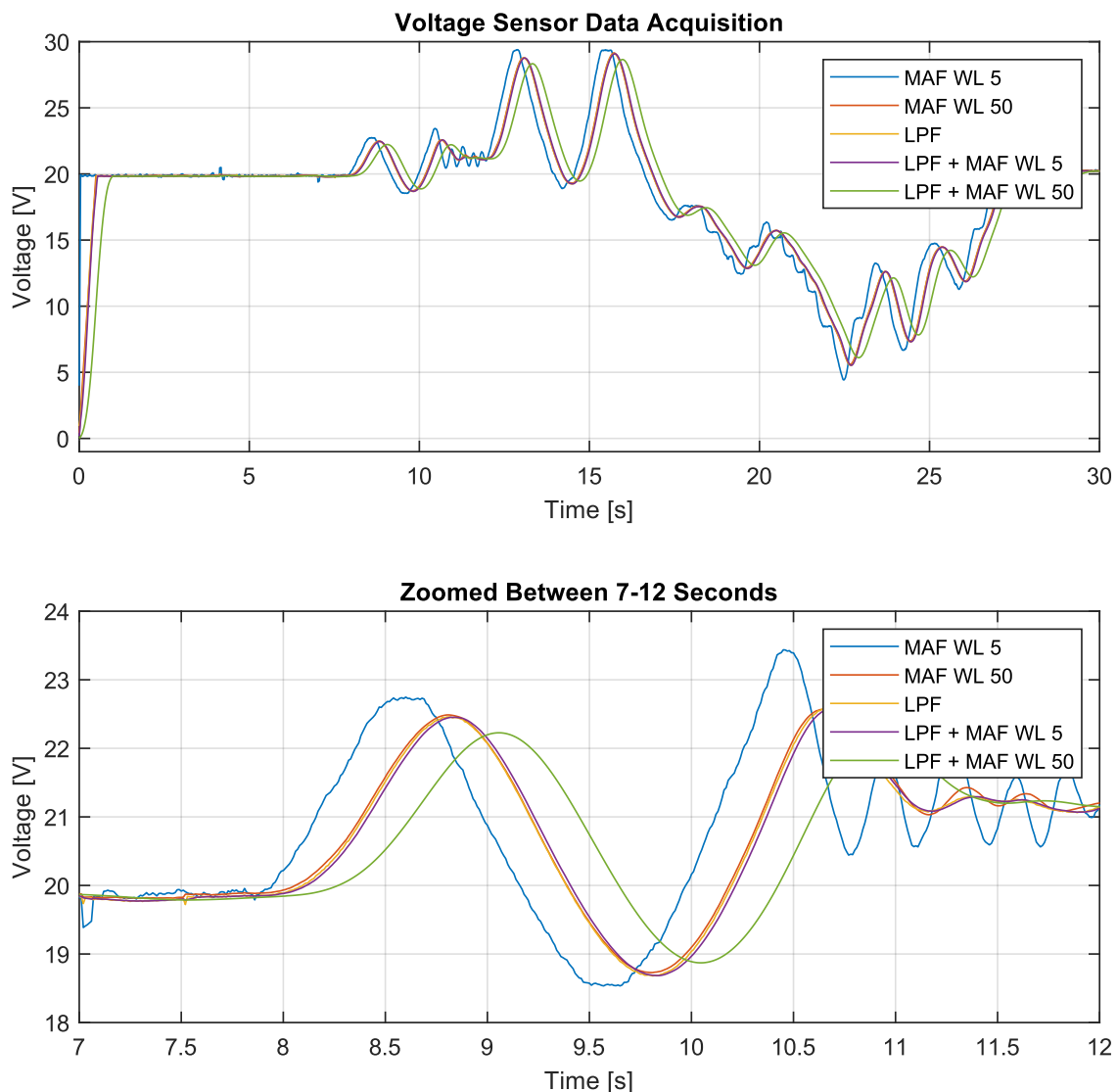


Figure 61 Voltage sensor data acquisitions with filters (top) and zoomed view (bottom)

The third validation is the speed sensing of a motor. A speed sensor (listed in the parts list) is connected to the GC and a thrust motor (listed in the parts list) which is controlled by an RC transmitter (FS-i6). For adjusting voltage for the GC, a series of resistors are utilised as a voltage divider. The data acquisition result from the sensor is revealed in figure 62 on the top and a remarkable range of the data is zoomed on at the bottom. The x-axis is time in seconds while the y-axis is the speed in revolution per minute. The data compares four non-filtered and filtered acquisitions. The MAF WL 100 and the LPF have relatively larger fluctuation. Meanwhile, the combination of them is more smooth with a

few time delays. Since the speed sensing sampling time is quite small, the time delay should be acceptable. Thus, the combination filter is applied for speed sensing.

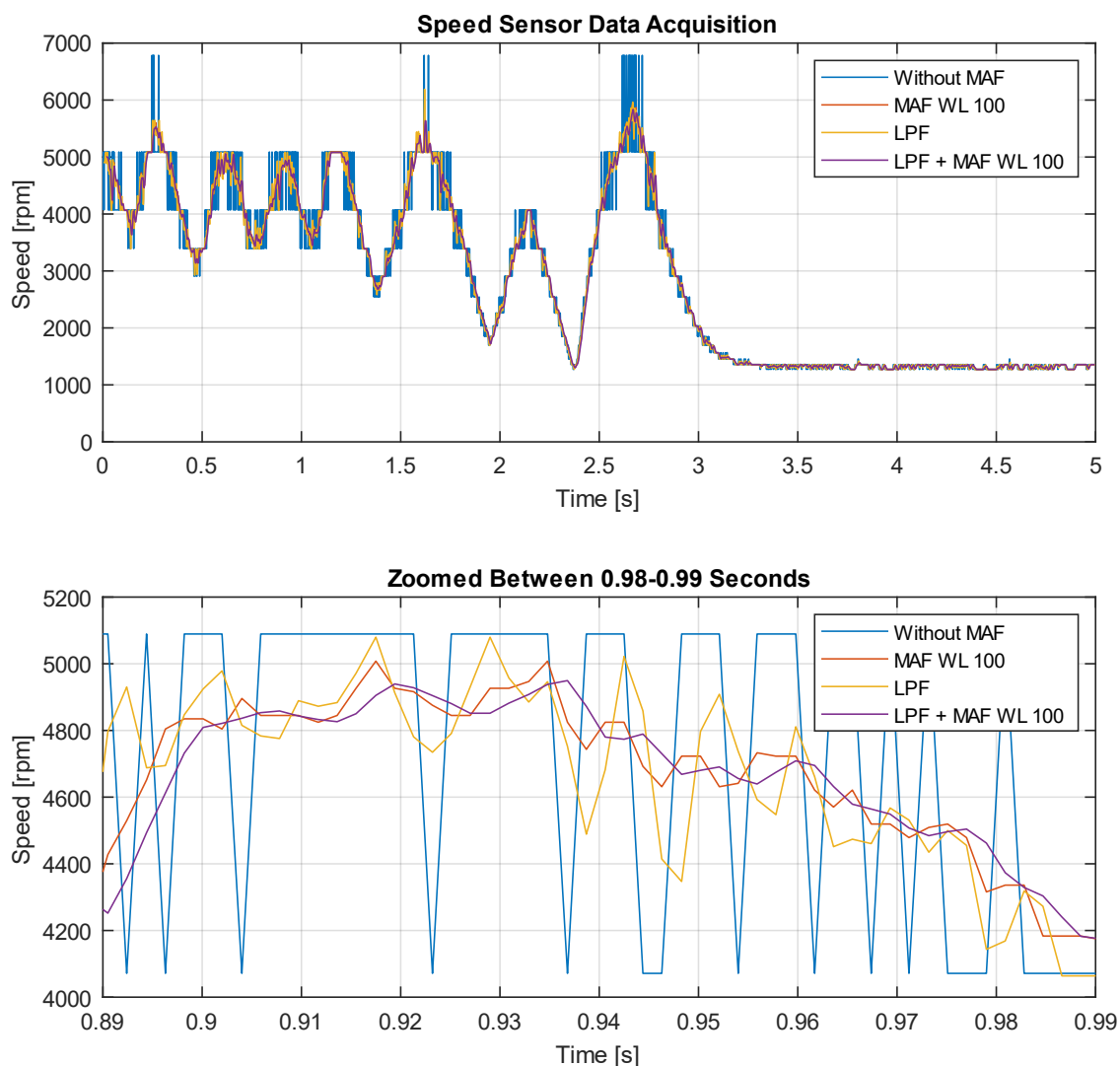


Figure 62 Speed sensor data acquisitions with filters (top) and zoomed view (bottom)

The fourth validation is PWM signal conversion for various switches. Since this is an application of speed sensing, the principle is the same as the previous validation but just with threshold functions. Also, PWM signals have a constant 20 ms period. The PWM signals come from an RC receiver (FS-i6B) controlled by an EC transmitter (FS-i6). For adjusting voltage for the GC, a series of resistors are also utilised here. The result is illustrated in figure 63, with the original PWM signals on the top, duty ratio and on/off switching on the bottom. The x-axes are time in seconds while the y-axes are signal logic,

duty ratio in blue colour and switch logic in orange colour. The conversion works quite well and there is nothing to mention for improvement.

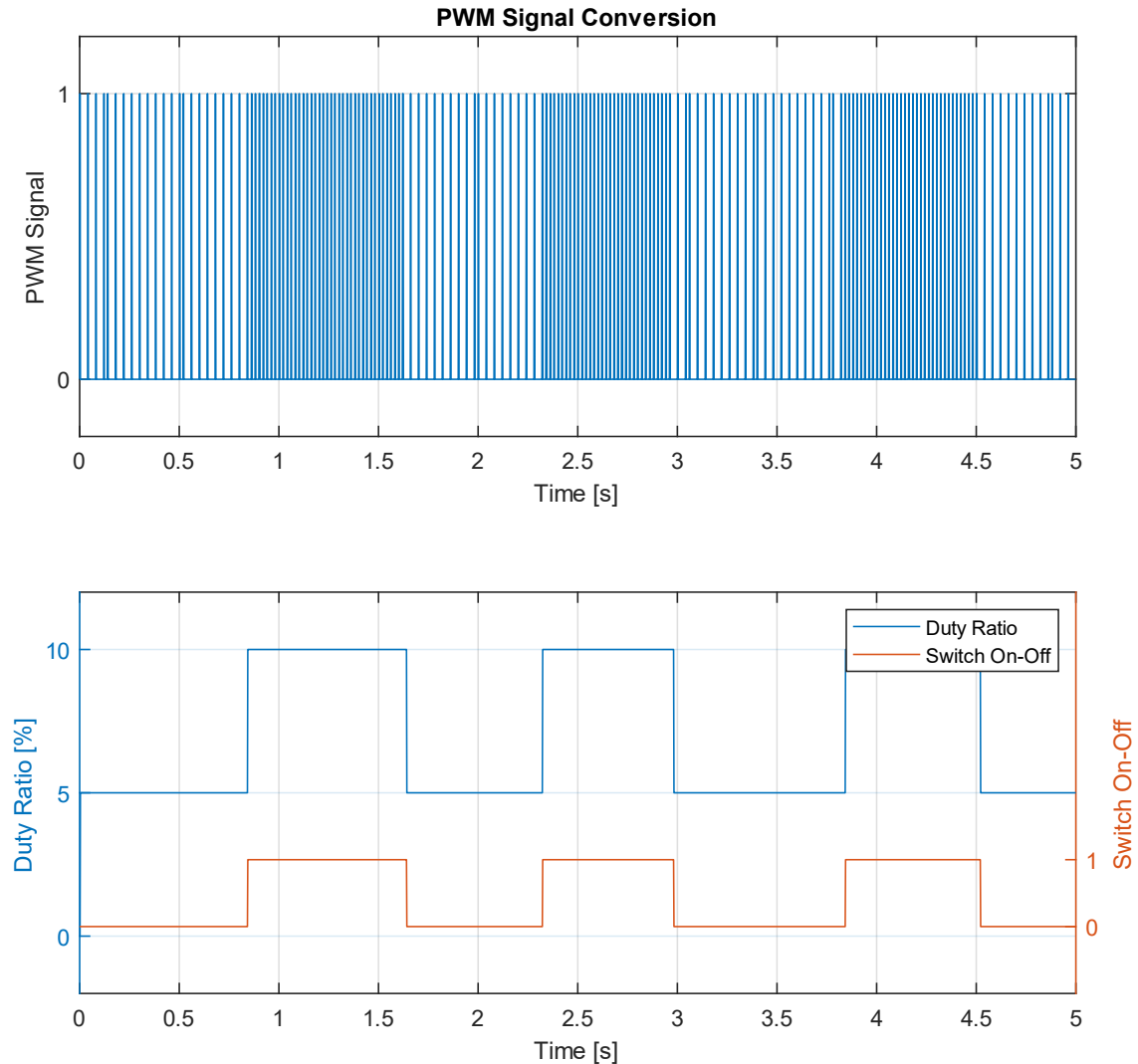


Figure 63 PWM signal (top) and conversion into duty ratio and ON/OFF signals (bottom)

The fifth validation is SOC estimation with a BMS. The validation setup is displayed in figure 64 (a). A BMS, a LiPo battery, voltage and current sensors are in the figure. They all are in the parts list. The sensors send data to the GC. The charging current is supplied from a power supply. Since discharging a few hundred watts is difficult in my environment, only charging validation is performed. Figure 64 (b) and (c) indicate voltages in each battery cell before and after 5 minutes of charging. Even though it is a small and short period of charge, the BMS equalises the cell voltages and seems working

properly. However, for validating the BMS's ability, a more significant variation and a long period of discharge must be required.

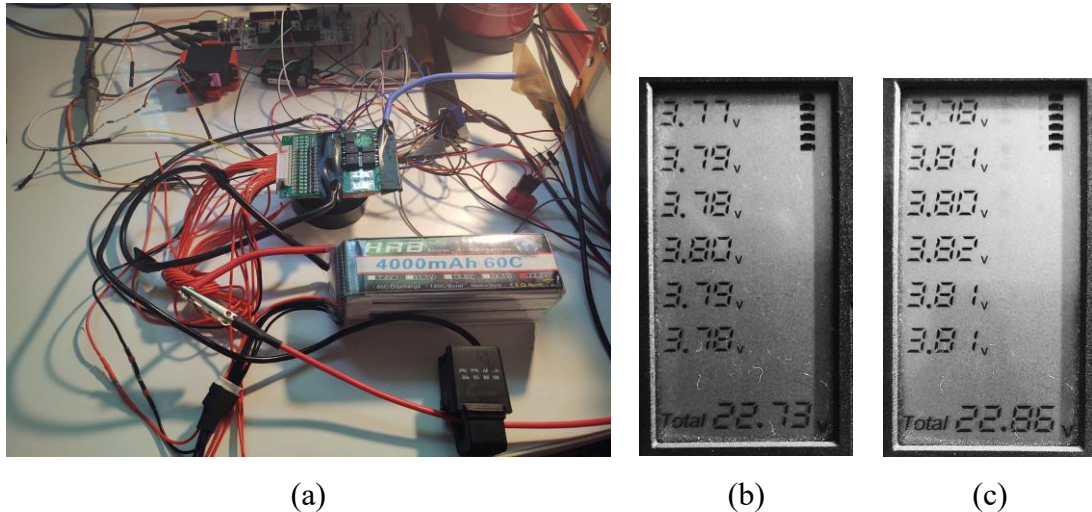


Figure 64 SOC estimation with BMS (a), battery cell voltages before and after 5 mins of charging (b) and (c)

The estimated SOC result is depicted in figure 65 on the top and remarkable ranges of the data are zoomed on at the middle and bottom. The x-axes are time in seconds while the y-axes are SOC in per cent. The data acquisition result with the selected filters from the battery voltage and current sensors are represented in figure 66 on the top and the bottom respectively. The voltage sensor derivative in the middle indicates how much the voltage is less varying or constant. The negative polarity of current implies charging. The x-axes are time in seconds while the y-axes are voltage in volts, derivative and current in ampere. In addition, a push button (on the GC) signal and a signal named “hybrid SOC signal” that combines OCV SOC into CC SOC, are revealed in figure 67 on the top and bottom each. The x-axes are time in seconds while the y-axes are logic signals. There are four method comparisons, a battery model, the OCV method, the CC method and their hybrid method. The battery model inputs the current data and outputs the SOC. The initial SOC is set to be the same for all by the push button as seen in the first 10 seconds. As varying charging (up to 2.5C) started, the battery model SOC increased according to the given charge. Since it is a mathematical model, no fluctuation can not be seen at all times. Regarding the OCV SOC, as charged longer, the voltage increases and the SOC also increases with large variation. When the charging current jumps suddenly, the voltage and the SOC rocket as well. On the contrary, when the charging current drops, the voltage

and the SOC fall rapidly. Also, it takes some time to be in a stable state like a first-order system. Considering the CC SOC, it is almost the same as the battery model SOC. However, the first three times at every 50 seconds, the push-button is pushed intensionally and the SOC is set based on the OCV SOC. After that, the SOC has a constant deviation. Whenever the button is pushed, the deviation is enlarged (since the voltage increases). In other words, the OCV modelling is not accurate for the used battery. Therefore, remodelling of the SOC depending on voltage is necessary. For the hybrid SOC, it is affected by OCV and CC SOC and the mentioned characteristics appear. The effect depends on a complementary OCV reliability ratio (0.2). One thing that differs from them is that it gains the OCV SOC automatically (hybrid SOC signal) when the battery voltage is stable, the current is not flowing and under a certain SOC (100 % this time). As a result, the trend is almost the same as the CC SOC but some effects from the OCV SOC appear sometimes.

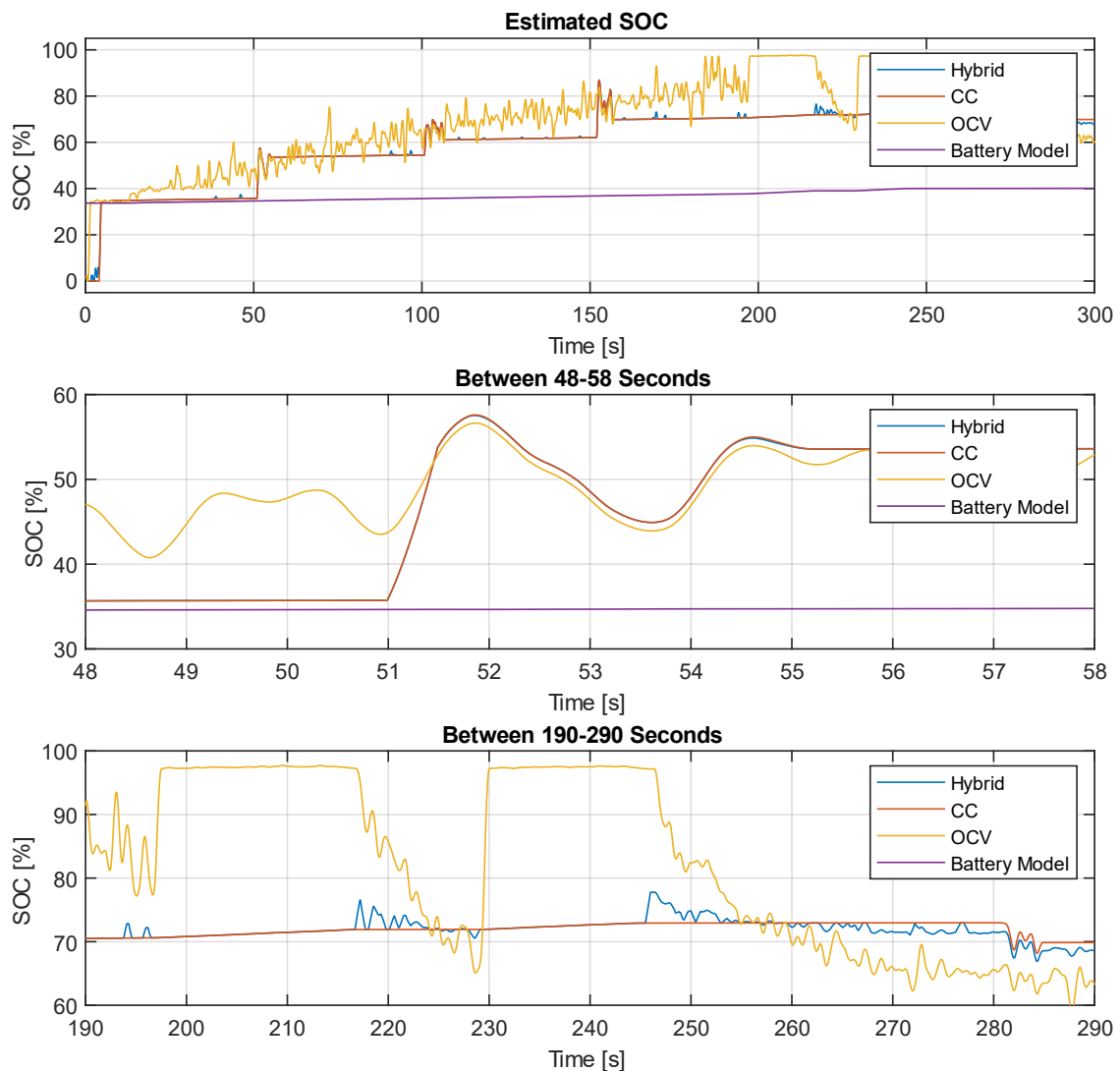


Figure 65 Estimated SOC (top), zoomed views (middle) and (bottom)

The validation is performed only when charging but discharging. Charging is limited at 4 A (1C) normally but discharging can go over 200 A. And, predictably, SOC estimation gets much more difficult. The introduced methods will not estimate the SOC properly in that case. Therefore, model-based SOC estimation such as an extended Kalman filter might be required for accurate estimation.

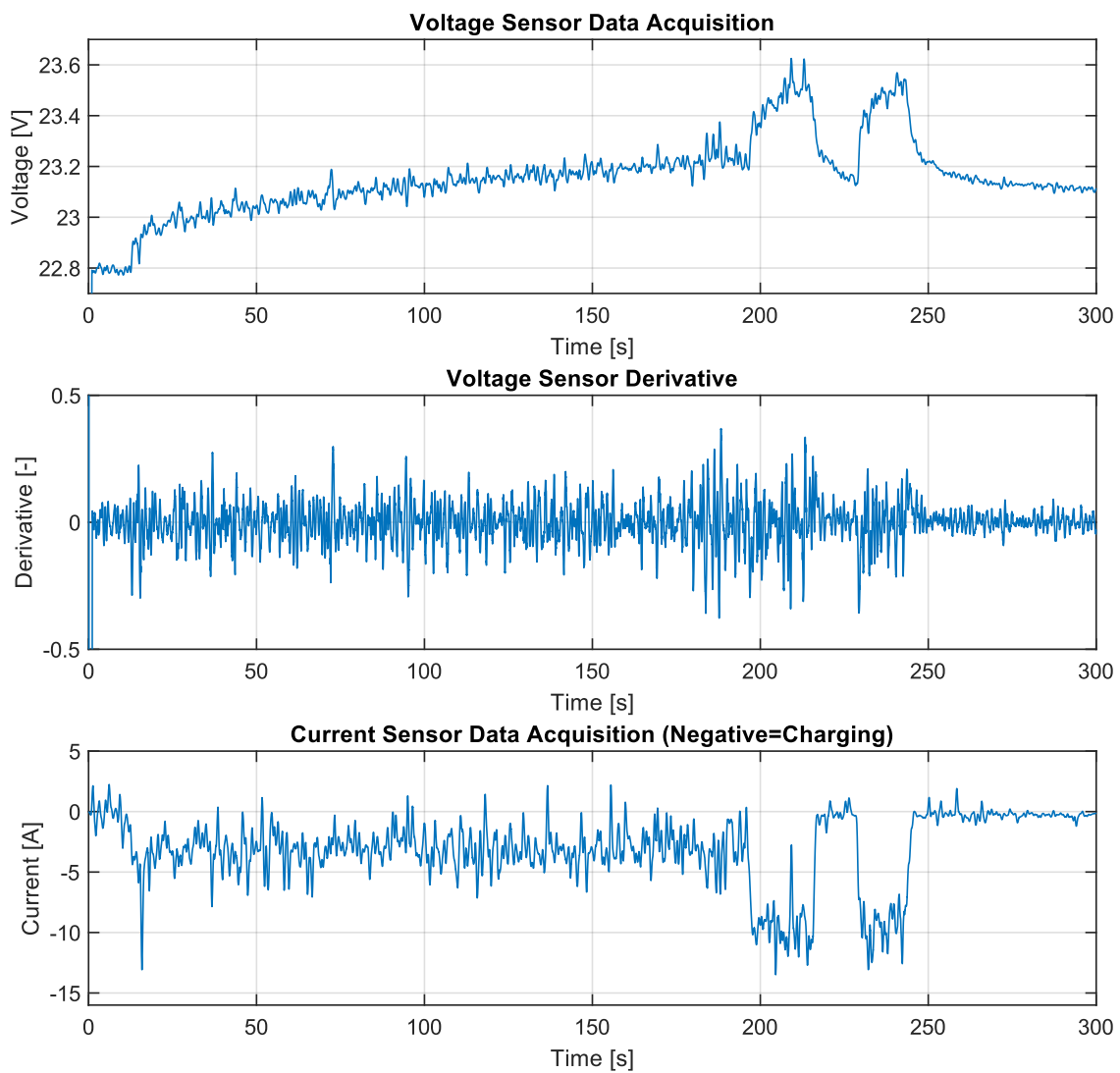


Figure 66 Voltage (top), voltage derivative (middle) and current (bottom) sensor data acquisitions during SOC measurement

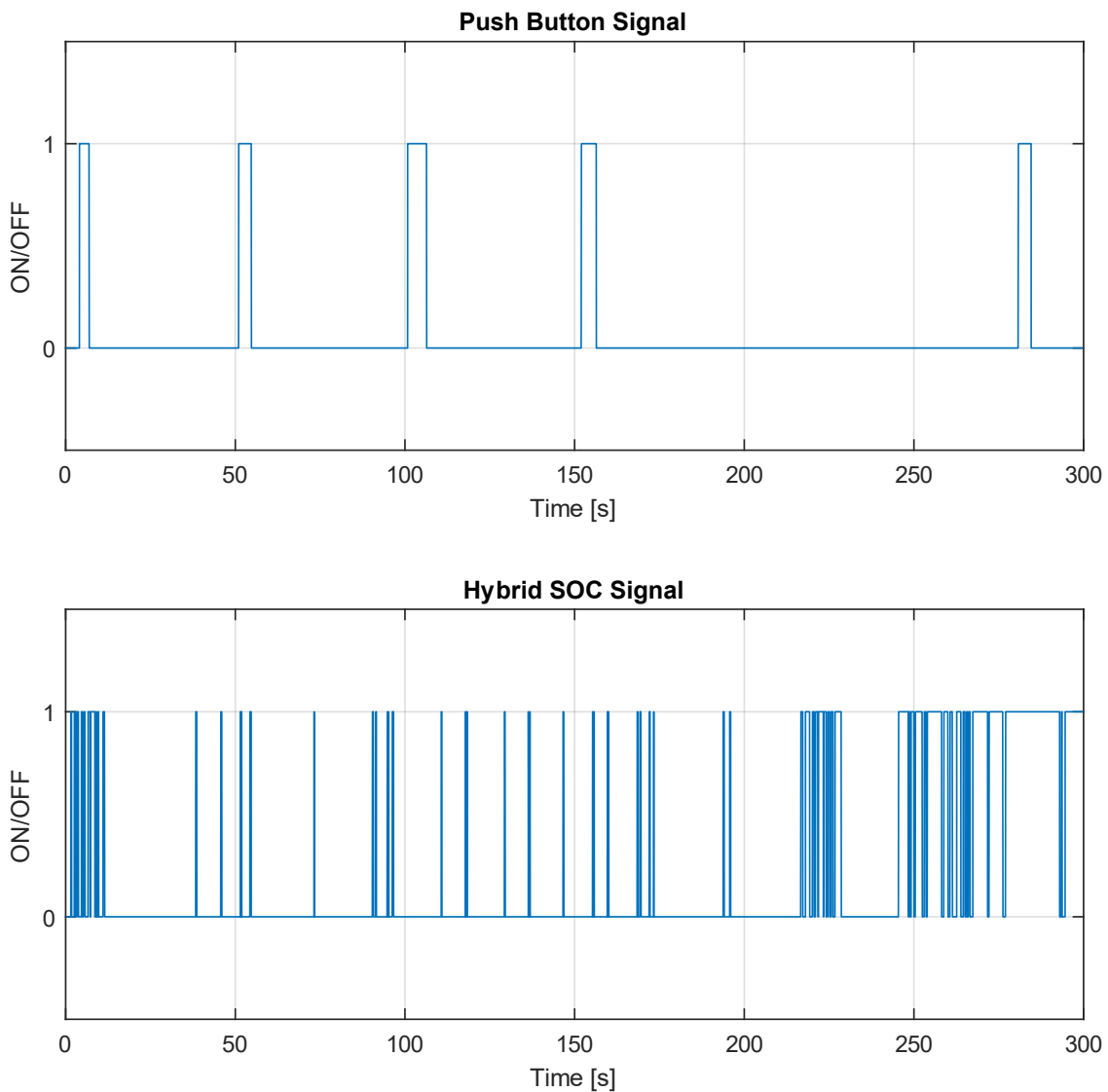


Figure 67 Push button (top) and hybrid SOC (bottom) signals during SOC measurement

The sixth validation is MOSFET logic control. It depends on the SOC, required power and generator power. The SOC is set in two setpoint constants, 95 and 50 % arbitrary. The SOC is manipulated by the push button on the GC only for this validation. The required power varies by a thrust motor's speed through the introduced estimators. For simplicity, only one motor is run and to consider eight motors rotate at the same speed. The generator power is set at 1800 W constant. All used instruments are the same as the already introduced ones. The results are shown in figure 68, with the SOC on the top, required power in blue colour and generator power in orange colour in the middle and the MOSFETs' duty ratios for charging and discharging on the bottom. The x-axes are time

in seconds while the y-axes are the SOC in per cent, power in watt and duty ratio in per cent respectively. When the SOC is 95 % and the required power is lower than the generator power, both charging and discharging MOSFETs' duty ratios stay at 0 %. As the SOC decreases under 90 %, the charging MOSFET's duty ratio is set to 95 % which means to allow the current flow. If the SOC is 95 % and the required power exceeds the generator power, the discharge MOSFET's duty ratio is set to 95 %. After all, it is confirmed that the MOSFET logic control works fine.

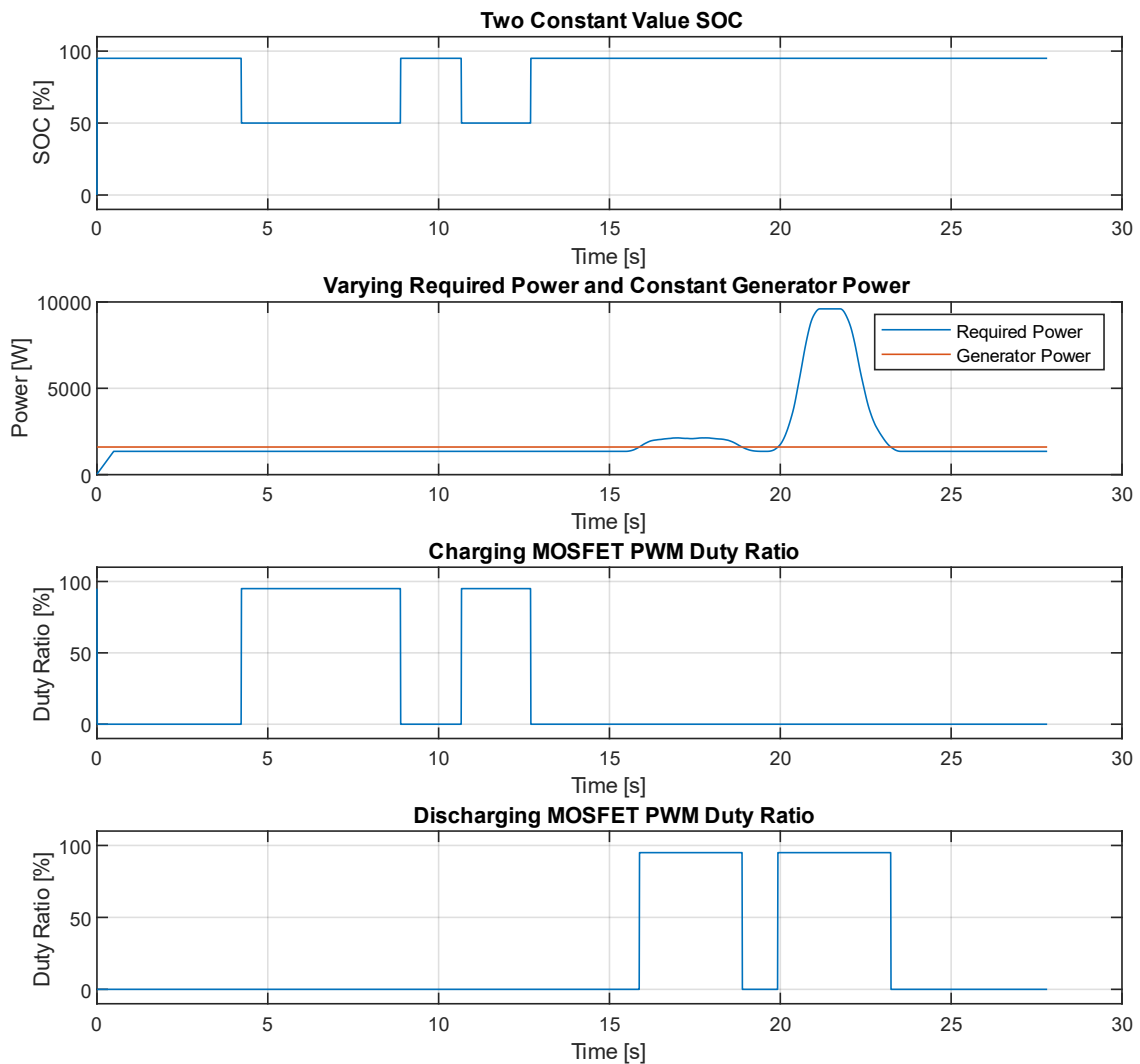


Figure 68 SOC (top), required and generator power (middle) and charging/discharging MOSFET PWM duty ratios (bottom)

The last validation is throttle PID control. A servomotor (listed in the parts list) is connected to the GC and the required power and the generator power are the same way

as in the previous validation. The results are depicted in figure 69, with the required power in blue colour and generator power in orange colour on the top and the ICE's throttle (the servomotor's angle) on the bottom. The x-axes are time in seconds while the y-axes are power in watt and ICE's throttle in per cent respectively. As the required power exceeds the generator power, the throttle increase and vice versa as expected. However, sudden drops or unnatural fluctuations can be found during the throttle operation. They might be caused by mismatched PID parameters. To solve the problem, modelling the accurate transfer function between the servomotor and the ICE must be needed because the PID parameters are tuned (by the CHR method) and depended on the estimated transfer function of the model.

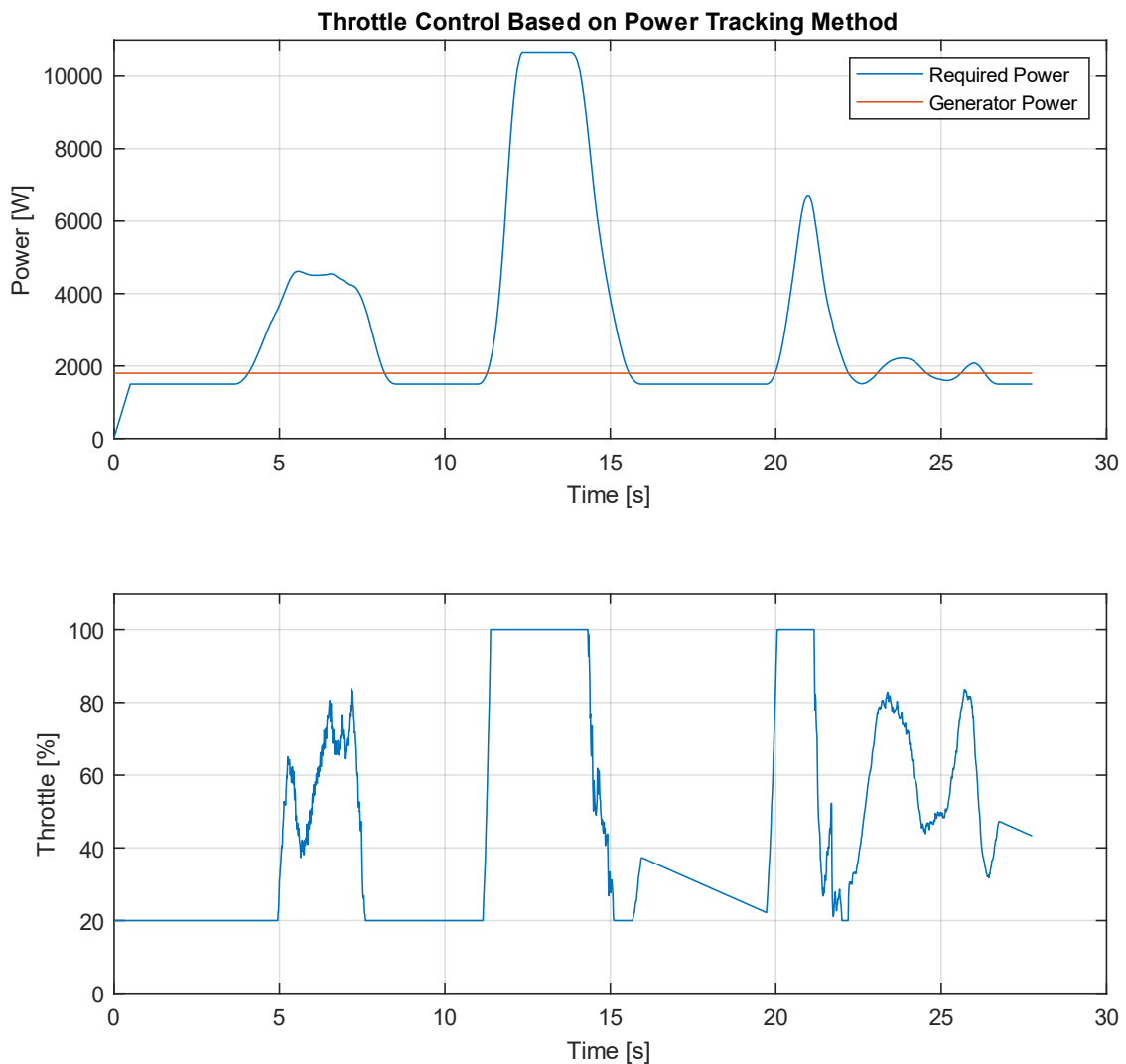


Figure 69 Required and generator power (top) and throttle servomotor PWM duty ratio (bottom)

CHAPTER 6

Conclusion

In conclusion, firstly, designing the HMC body considering efficiency and safety is introduced. Next, block connections for the HMC's power electronics are created. Accordingly, electronics and related parts are selected satisfying various requirements. For achieving high efficiency, the power voltage should be set high, 12-cell, 24-cell or even more. Accompanied by that, choosing a high-voltage compatible ESC is inevitable. At least for this designed HMC, alternating the selected ESC with a high-efficient ESC is suggested to gain 20 % more efficiency. Thirdly, control systems for the PMSG unit are designed. In the end, the HMC body and the PMSG unit are constructed and validated experimentally. There are four revealed facts from the PMSG unit validations. The first is that an ordinary ESC for MC cannot be utilised for the ICE starter with the PMSG due to a torque variation caused by the ICE's compression and expansion cycles. The second is that an ESC as an ICE starter might have a problem when the ICE's speed exceeds the ESC's maximum speed. The third is that the PMSG unit should have allowed direct access to the pulley holder shaft or the ICE's shaft. The fourth is that some mechanical parts such as the pulley holder should have been chosen or designed considering the torque, stresses and vibrations. Especially for the pulley holder, it should have been equipped with a key for torque transfer and should have been fixed on the PMSG with more bolts. Regarding the control systems, they are implemented on NUCLEO F767ZI and are validated experimentally with the related electronics. The data acquisitions with various filters are compared by analysing the frequency spectrum. For the speed sensing algorithm, the FFT-based one could have been more accurate. Considering the SOC estimation, the designed estimations are quite different from the mathematical model due to deviations in the SOC model that depends on voltage. Furthermore, the SOC estimation by the designed methods when huge discharging must be challenging. Therefore, a model-based SOC estimation is suggested. Regarding the throttle PID control, it works somehow but the PID parameters should have need tuned based on an accurate transfer function of a model.

Acknowledgement

First, I would like to say a special thank you to my supervisor, doc. Ing. Martin Novák, Ph.D. for his consistent support and guidance during the running of this project. Also, I would like to thank Ing. Zdeněk Novák Ph.D. for advising and helping the project a lot. Second, I would also like to acknowledge Czech Technical University in Prague for their engagement in the study and research as well as big financial support. Also, I would like to express my appreciation to SAITOTEC Co., Ltd. for its experienced advice and huge financial support. In the end, many thanks to my family and friends.

References

- [1] L. V. Pham, B. Dickerson and J. Sanders, "UAV swarm attack: protection system alternatives for Destroyers;Casserly, Michael;Maldonado, Vicente;Balbuena, Demostenes;Graves, Stephen;Pandya, Bhavisha," NAVAL POSTGRADUATE SCHOOL, Monterey, 2012.
- [2] D. Valdenegro, A. Capunay, D. Gonzalez, L. R. G. Carrillo and P. Rangel, "Improving Safety: Design and Development of a Bladeless Thruster for Autonomous Multicopters," in *2018 International Conference on Unmanned Aircraft Systems (ICUAS)*, Dallas, 2018.
- [3] D. Q. Nguyen, G. Loianno and V. A. Ho, "Towards Design of a Deformable Propeller for Drone Safety," in *2020 3rd IEEE International Conference on Soft Robotics (RoboSoft)*, New Haven, 2020.
- [4] J. Jang, K. Cho and G.-H. Yang, "Design and Experimental Study of Dragonfly-Inspired Flexible Blade to Improve Safety of Drones," *IEEE Robotics and Automation Letters*, vol. 4, no. 4, pp. 4200-4207, 2019.
- [5] R. Oliver, S. Y. Khoo, M. Norton, S. Adams and A. Kouzani, "Development of a Single Axis Tilting Quadcopter," in *2016 IEEE Region 10 Conference (TENCON)*, Singapore, 2016.
- [6] M. Nisser, C. Liao, Y. Chai, A. Adhikari, S. Hodges and S. Mueller, "LaserFactory: A Laser Cutter-based Electromechanical Assembly and Fabrication Platform to Make Functional Devices & Robots," in *CHI Conference on Human Factors in Computing Systems*, 2021.
- [7] S. Sun, G. Cioffi, C. d. Visser and D. Scaramuzza, "Autonomous Quadrotor Flight despite Rotor Failure with Onboard Vision Sensors: Frames vs. Events," *IEEE Robotics and Automation Letters*, p. 99, 2021.
- [8] A. LOQUERCIO, E. KAUFMANN, R. RANFTL, M. MÜLLER, V. KOLTUN and D. SCARAMUZZA, "Learning High-Speed Flight in the Wild," *Science Robotics*, vol. 6, no. 59, 2021.
- [9] K. Celik and H. Eren, "UAV Fuel Preferences for Future Cities," in *2018 6th International Istanbul Smart Grids and Cities Congress and Fair (ICSG)*, Istanbul, 2018.
- [10] "Drone Industry Insights," Drone Industry Insights UG, [Online]. Available: <https://droneii.com/>. [Accessed 14 2 2022].
- [11] M. N. Boukoberine, Z. Zhou and M. Benbouzid, "A Critical Review on Unmanned Aerial Vehicles Power Supply and Energy Management Solutions, Strategies, and Prospects," *Elsevier Applied Energy*, vol. 255, 2019.
- [12] B. Bluteau, R. Briand and O. Patrouix, "Design and Control of an Outdoor Autonomous Quadrotor powered by a four strokes RC engine," in *IECON 2006 - 32nd Annual Conference on IEEE Industrial Electronics*, Paris, 2006.
- [13] S. F. Tie and C. W. Tan, "A review of energy sources and energy management system in electric vehicles," *Renewable and Sustainable Energy Reviews*, vol. 20, pp. 82-102, 2013.
- [14] Y. Kato, S. Hori, T. Saito, K. Suzuki, M. Hirayama, A. Mitsui, M. Yonemura, H. Iba and R. Kanno, "High-power all-solid-state batteries using sulfide superionic conductors," *Nature Energy*, vol. 1, no. 4, pp. 1-7, 2016.

- [15] H. Zhang, C. Saudemont, B. Robyns and M. Petit, "Comparison of Technical Features between a More Electric Aircraft and a Hybrid Electric Vehicle," in *2008 IEEE Vehicle Power and Propulsion Conference*, Harbin, 2008.
- [16] D. Meyer, R. Alexander and J. Wang, "A Simple Method for Energy Optimization to Enhance Durability of Hybrid UAV Power Systems," in *2017 North American Power Symposium (NAPS)*, Morgantown, 2017.
- [17] M. Bai, W. Yang, D. Song, M. Kosuda, S. Szabo, P. Lipovsky and A. Kasaei, "Research on Energy Management of Hybrid Unmanned Aerial Vehicles to Improve Energy-Saving and Emission Reduction Performance," *International Journal of Environmental Research and Public Health*, vol. 17, no. 8, p. 2917, 2020.
- [18] M. Huang and Y. Guo, "Research on Energy Management of Hybrid Electric Vehicle," in *2021 International Conference on Machine Learning and Intelligent Systems Engineering (MLISE)*, Chongqing, 2021.
- [19] Fineart, "photoAC," [Online]. Available: <https://www.photo-ac.com/profile/1481865>. [Accessed 14 2 2022].
- [20] K. Nagashima, "Design of a Small Quadrotor," Czech Technical University in Prague, Prague, 2020.
- [21] K. Noba, *Drone Engineering: from Modelling to Controlling (Drone Kougaku Nyumon: Modelling Kara Seigyo Made)*, CORONA PUBLISHING CO.,LTD., 2020.
- [22] "PX4 User Guide," [Online]. Available: <https://docs.px4.io/master/en/>. [Accessed 14 2 2022].
- [23] T. J. Mueller, "Aerodynamic Measurements at Low Reynolds Numbers for Fixed Wing Micro-Air Vehicles," Hessert Center for Aerospace Research University of Notre Dame, Belgium, 1999.
- [24] Y. T. Kim, C. H. Park and H. Y. Kim, "Three-Dimensional CFD Investigation of Performance and Interference Effect of Coaxial Propellers," in *2019 IEEE 10th International Conference on Mechanical and Aerospace Engineering (ICMAE)*, 2019.
- [25] J. L. Pereira, "Hover and wind-tunnel testing of shrouded rotors for improved micro air vehicle design," University of Maryland, College Park, 2008.
- [26] B. Theys, G. Dimitriadis, P. Hendrick and J. D. Schutter, "Influence of propeller configuration on propulsion system efficiency of multi-rotor Unmanned Aerial Vehicles," in *2016 International Conference on Unmanned Aircraft Systems (ICUAS)*, Arlington, 2016.
- [27] "A New Fault Tolerant Multicopter Using Dense Propellers for Size Compacting -- A New Direction in Multicopter Design Part 2 --".
- [28] "A New Stable Multicopter Avoiding Crashes without the Detection of Rotor Failure -- A New Direction in Multicopter Design --".
- [29] TechIngredients, "Hybrid Drone Generator," TECH INGREDIENTS LLC., [Online]. Available: <https://youtu.be/1yB49G756OI>. [Accessed 14 2 2022].
- [30] "Sankyo Manufacturing," Sankyo Manufacturing Co.,ltd, [Online]. Available: <https://www.sankyo-ss.co.jp/about-cfrp.html>. [Accessed 14 2 2022].
- [31] "ELEVATED MATERIALS," ELEVATED MATERIALS, [Online]. Available: <https://www.elevatedmaterials.com/carbon-fiber-weaves-what-they-are-and-why-to-use-them/>. [Accessed 14 2 2022].

- [32] “Foundation for Promotion of Material Science and Technology of Japan,” Foundation for Promotion of Material Science and Technology of Japan, [Online]. Available: <https://www.mst.or.jp/casestudy/tabid/1318/pdId/476/Default.aspx>. [Accessed 14 2 2022].
- [33] C. Dughir, “Power wire thickness influence on the multicopters flight time,” in *2016 12th IEEE International Symposium on Electronics and Telecommunications (ISETC)*, Timisoara, 2016.
- [34] V. M. Dileepan, K. T. Madhavan and J. Jayakumar, “Performance Analysis of Lithium Polymer Battery and Super Capacitor,” in *2017 International Conference on Energy, Communication, Data Analytics and Soft Computing (ICECDS)*, Chennai, 2017.
- [35] O. Corporation, “Products FAQ,” OMRON Corporation, [Online]. Available: <https://faq.fa.omron.co.jp/tech/s/article/faq02804>. [Accessed 14 2 2022].
- [36] “DIY Database (自作用データベース(バッテリー自作知識編)),” esk8.jp, [Online]. Available: <https://esk8.jp/>. [Accessed 14 2 2022].
- [37] “NITRO-X,” O.S.ENGINES.Mfg.,Co.Ltd., [Online]. Available: <http://www.nitro-x.jp/secret/02.html>. [Accessed 14 2 2022].
- [38] “x-engineer.org,” [Online]. Available: <https://x-engineer.org/power-vs-torque/>. [Accessed 14 2 2022].
- [39] “T-motor,” T-motor, [Online]. Available: <https://store.tmotor.com/>. [Accessed 14 2 2022].
- [40] Designatronics Inc., [Online]. Available: <https://sdp-si.com/resources/>. [Accessed 14 2 2022].
- [41] Y. Tomoaki, “Development of high efficiency multicopter,” *Hiroshima Institute of Technology Bulletin*, vol. 52, pp. 125-131, 2018.
- [42] T. E. D. & S. Corporation, “120° Square-Wave Commutation for Brushless DC Motors,” Toshiba Electronic Devices & Storage Corporation, 2018.
- [43] D. G. Lui, “Gough's Tech Zone,” [Online]. Available: <https://goughlui.com/2021/02/28/tested-xw-0936-24-240w-9-36v-to-24v-10a-dc-dc-buck-boost-converter/>. [Accessed 14 2 2022].
- [44] A. v. Dalen, “avdweb,” [Online]. Available: <https://avdweb.nl/solar-bike/electronics/bms/battery-management-system-bms>. [Accessed 14 2 2022].
- [45] FoolishEngineer, “How does a BMS (Battery Management System) work? | Passive & Active cell balancing Explained,” [Online]. Available: https://youtu.be/q4wDa_m9-8E. [Accessed 14 2 2022].
- [46] “Battery State of Charge calculation with EPC Converters,” Epic Power Converters, S.L., Zaragoza, 2020.
- [47] “Li-ion Battery and Gauge Introduction,” Richtek Technology Corporation., [Online]. Available: <https://www.richtek.com/Design%20Support/Technical%20Document/AN024>. [Accessed 14 2 2022].
- [48] M. Murnane and A. Ghazel , “A Closer Look at State Of Charge (SOC) and State Of Health (SOH) Estimation Techniques for Batteries,” Analog Devices, Inc..
- [49] W.-Y. Chang, “The State of Charge Estimating Methods for Battery: A Review,” *International Scholarly Research Notices*, vol. 2013, p. 7, 2013.
- [50] KEI, “Minimum Structured Model-Based Development Examples Back Number (最小構成のモデルベース開発事例 バックナンバー),” 14 11 2021. [Online]. Available:

<https://www.simulationroom999.com/blog/model-based-of-minimum-backnumber/>. [Accessed 14 2 2022].

- [51] K. J. Åström, “Control System Design Lecture notes for ME 155A,” *Department of Mechanical and Environmental Engineering University of California Santa Barbara*, vol. 333, 2022.
- [52] L. Wang, *PID Control System Design and Automatic Tuning using MATLAB/Simulink*, Wiley-IEEE Press, 2020.
- [53] V. Bobál, J. Macháček and R. Prokop, “Tuning of Digital PID Controllers Based on Ziegler - Nichols Method,” *IFAC Proceedings Volumes*, vol. 30, no. 21, pp. 145-150, 1997.
- [54] M. Shahrokhi and A. Zomorodi, “Comparison of PID Controller Tuning Methods”.
- [55] “PID Controller,” The MathWorks, Inc., [Online]. Available: <https://jp.mathworks.com/help/simulink/sref/pidcontroller.html?lang=en>. [Accessed 14 2 2022].
- [56] “EnergyChord,” [Online]. Available: http://energychord.com/children/energy/pe/dcdc/contents/dcdc_chopper_types.html. [Accessed 14 2 2022].
- [57] “Gas Engine Magazine,” Ogden Publications, Inc., [Online]. Available: <https://www.gasenginemagazine.com/gas-engines/2-stroke-cycle-zm0z19djzhur>. [Accessed 14 2 2022].
- [58] A. Vojáček, “BLDC / EC technology or AC with inverter? (BLDC / EC technologie nebo AC s měničem?),” [Online]. Available: <https://automatizace.hw.cz/ec-technologie-nebo-frekvencni-menic.html>. [Accessed 14 2 2022].
- [59] S. Goodarzil, R. Beiranvand, S. M. Mousavi and M. Mohamadian, “A New Algorithm for Increasing Balancing Speed of Capacitor Lithium-Ion Battery Cell Equalizers,” in *The 6th International Power Electronics Drive Systems and Technologies Conference (PEDSTC2015)*, Tehran, Iran, 2015.
- [60] T. LEI, Z. YANG, Z. LIN and X. ZHANG, “State of art on energy management strategy for hybrid-powered unmanned aerial vehicle,” *Chinese Journal of Aeronautics*, vol. 32, no. 6, pp. 1488-1503, 2019.
- [61] “Measuring the differences: Shunt-based sensing technology vs. magnetic solutions,” GlobalSpec, [Online]. Available: <https://electronics360.globalspec.com/article/15270/measuring-the-differences-shunt-based-sensing-technology-vs-magnetic-solutions>. [Accessed 14 2 2022].
- [62] “Principle of Current Sensors and Technical Information (電流センサの原理と技術情報),” HIOKI E.E. CORPORATION, [Online]. Available: <https://www.hioki.co.jp/jp/products/listUse/?category=39>. [Accessed 14 2 2022].
- [63] T. H. Inc., “FIR Filter,” Typhoon HIL Inc., [Online]. Available: https://www.typhoon-hil.com/documentation/typhoon-hil-software-manual/References/fir_filter.html. [Accessed 14 2 2022].
- [64] S. Aich, C. Ahuja, T. Gupta and P. Arulmozhivarman, “Analysis of Ground Effect on Multi-Rotors,” in *International Conference on Electronics, Communication and Computational Engineering*, Hosur, 2014.

- [65] V. Vara and P. Wadhvani, "How to Calculate State of Charge(SOC)? Battery & Energy Technologies," Bacancy, 13 12 2021. [Online]. Available: <https://www.bacancytechnology.com/blog/state-of-charge-calculation-for-battery-energy>. [Accessed 14 2 2022].
- [66] B. G. Kim, F. P. Tredeau and Z. M. Salameh, "Fast Chargeability Lithium Polymer Batteries," in *2008 IEEE Power and Energy Society General Meeting - Conversion and Delivery of Electrical Energy in the 21st Century*, Pittsburgh, 2008.
- [67] S. Goodarzi, R. Beiranvand, S. M. Mousavi and M. Mohamadian, "A new algorithm for increasing balancing speed of switched-capacitor lithium-ion battery cell equalizers," in *The 6th Power Electronics, Drive Systems & Technologies Conference (PEDSTC2015)*, Tehran, 2015.
- [68] T. LEI, Z. YANG, Z. LIN and X. ZHANG, "State of art on energy management strategy for hybrid-powered unmanned aerial vehicle".
- [69] W. Lu, D. Zhang, J. Zhang, T. Li and T. Hu, "Design and implementation of a gasoline-electric hybrid propulsion system for a micro triple tilt-rotor VTOL UAV," in *2017 6th Data Driven Control and Learning Systems (DDCLS)*, Chongqing, 2017.
- [70] H. Qian, Y. Zhang, W. Qin, F. Wang and X. Ding, "Design and Implementation of Hybrid UAV Starter/Generator Module," in *2018 Joint International Conference on Energy, Ecology and Environment (ICEEE 2018) and International Conference on Electric and Intelligent Vehicles (ICEIV 2018)*, 2019.
- [71] J. Yun, S. Cho, H. c. Liu, H.-W. Lee and J. Lee, "Design of Electromagnetic Field of Permanent Magnet Generator for VTOL Series-Hybrid UAV," in *2015 18th International Conference on Electrical Machines and Systems (ICEMS)*, Pattaya, 2015.
- [72] Š. Riss, "Development of a Hybrid Power Unit for Unmanned Aerial Vehicles," Czech Technical University in Prague, Prague, 2017.
- [73] D. Pavković, M. Krznar, M. Čipek, D. Zorc and M. Trstenjak, "Internal Combustion Engine Control System Design Suitable for Hybrid Propulsion Applications*," in *2020 International Conference on Unmanned Aircraft Systems (ICUAS)*, Athens, 2020.
- [74] P. Gasior, A. Bondyra, S. Gardecki, W. Giernacki and A. Kasiński, "Thrust estimation by fuzzy modeling of coaxial propulsion unit for multicopter UAVs," in *2016 IEEE International Conference on Multisensor Fusion and Integration for Intelligent Systems (MFI)*, Baden, 2016.
- [75] T. Donato, L. Spedicato and D. P. Placentino, "Design and performance evaluation of a hybrid electric power system for multicopters," *Energy Procedia*, vol. 126, pp. 1035-1042, 2017.
- [76] G. J. Ducard and M. Allenspach, "Review of designs and flight control techniques of hybrid and convertible VTOL UAVs," *Aerospace Science and Technology*, vol. 118, 2021.
- [77] I. M. N. Ph.D., "Lecture 12+13 Validation of sensor signals," Prague, 2021.

Appendix

Parameters defined in MATLAB for the designed control systems are displayed below.

```
%% simulink
Ts = 0.0001; % sampling period [s]
Fs = 1/Ts % sampling frequency [Hz]
%% board
Ts_board = 0.01; % sampling period [s]
Fs_board = 1/Ts_board % sampling frequency [Hz]
Vr = 3.3; % reference voltage for F767ZI analogue input port
%% generator and motor
RR = 1.5; % reduction ratio between engine and generator
KV = 120; % KV value of generator
wght_total = 12; % total weight [kg]
P_gen = 42; % number of poles
P_mot = 28; % number of poles
%% voltage and current sensor
Ts_anlg = 0.01; % sampling period [s]
Fs_anlg = 1/Ts_anlg % sampling frequency [Hz]
R1 = 190*1000; % resistance 1 [ohm]
R2 = 10*1000; % resistance 2 [ohm]
Gain_current = 0.05; % gain for current sensor
Offset_current = 3; % offset for current sensor
%% speed sensor
Ts_speed = 0.0001; % sampling period [s]
Fs_speed = 1/Ts_speed % sampling frequency [Hz]
Gain_speed = 0.95; % gain for speed sensor
%% switch
Ts_switch = 0.0001; % sampling period [s]
Fs_switch = 1/Ts_switch % sampling frequency [Hz]
DRupper_switch = 9; % upper duty ratio [%]
DRlower_switch = 6; % lower duty ratio [%]
DRupper_switch_15 = 12; % upper duty ratio [%]
DRlower_switch_15 = 8; % lower duty ratio [%]
%% MOSFET
Finit_MOSFET = Fs_board % initial frequency [Hz]
DRon_MOSFET = 95; % on duty ratio [%]
DRoff_MOSFET = 0; % off duty ratio [%]
DRinit_MOSFET = 0; % initial duty ratio
%% servomotor
Ts_servo = 0.02; % sampling period [s]
Fs_servo = 1/Ts_servo % sampling frequency [Hz]
Ts_servo_15 = 0.015; % sampling period [s]
Fs_servo_15 = 1/Ts_servo_15 % sampling frequency [Hz]
DRopmin_servo = 6; % minimum throttle duty ratio [%]
DRstop_servo = 5; % stop engine angle duty ratio [%]
%% estimator
eff_coax = 0.9; % efficiency of coaxial configuration
%% estimator battery 6-cell
Cap_bat_Ah = 4; % battery capacity [Ah]
% from Excel
V_bat_approx_Thr_1 = 23.29; % threshold for approximation of battery voltage
V_bat_approx_Thr_2 = 23.00; % threshold for approximation of battery voltage
V_bat_approx_Thr_3 = 22.05; % threshold for approximation of battery voltage
V_bat_approx_eq_1_a = 1.767; % coefficient of equation for approximation of
battery voltage
V_bat_approx_eq_1_b = 5.6*10^1; % coefficient of equation for approximation
of battery voltage
V_bat_approx_eq_2_a = 1.931*10^2; % coefficient of equation for
approximation of battery voltage
```

```

V_bat_approx_eq_2_b = -4.401*10^3; % coefficient of equation for
approximation of battery voltage
V_bat_approx_eq_3_a = 3.091*10^1; % coefficient of equation for
approximation of battery voltage
V_bat_approx_eq_3_b = -6.701*10^2; % coefficient of equation for
approximation of battery voltage
V_bat_approx_eq_4_a = 4.604; % coefficient of equation for approximation of
battery voltage
V_bat_approx_eq_4_b = -9.010*10^1; % coefficient of equation for
approximation of battery voltage
% from experiments
a_power_to_thrust = -0.0051; % coefficient of equation for power to thrust
estimation
b_power_to_thrust = 8.8519; % coefficient of equation for power to thrust
estimation
a_speed_to_thrust = 0.0003; % coefficient of equation for speed to thrust
estimation
b_speed_to_thrust = -0.1097; % coefficient of equation for speed to thrust
estimation
a_thrust_to_power = 3*10^-5; % coefficient of equation for thrust to power
estimation
b_thrust_to_power = 0.0674; % coefficient of equation for thrust to power
estimation
%
Thr_SOC_max = 90; % max threshold for SOC
Thr_SOC_min = 20; % min threshold for SOC
Thr_SOC_ltd = 10; % limited threshold for SOC
Thr_crnt_zero = 0.5; % zero threshold for current
Thr_vltg_zero = 0.5; % zero threshold for voltage
Thr_SOC_complementary_filter = 100; % threshold for complementary filter [%]
stp_derivative = 1/(Ts_board*10); % number of step for derivative
SOC_OCV_reliability = 0.2; % SOC OCV method reliability
Gain_SOC_OCV = 1; % gain for SOC OCV method
Init_SOC = 100; % initial SOC [%]
Init_V_bat = 25.2; % initial battery voltage [V]
%% moving average window length
WL_current = 50; % for current sensor
WL_voltage = 50; % for voltage sensor
WL_speed_gen = 100; % for generator speed sensor
WL_speed_mot = 100; % for motor speed sensor
WL_power = 50; % for power output
WL_SOC = 50; % for SOC output
WL_thrust = 50; % for thrust output
%% PID controller by CHR method
% ICE transfer function
% input = servomotor duty ratio [%]
% output = speed [rpm]
L = 1; % time delay
T = 3; % time constant
K = 900; % steady state gain (9000rpm/10%)
%Kp = (0.35*T)/(K*L) % PI
%Ki = 0.29/(K*L) % PI
Kp = (0.6*T)/(K*L); % PID
Ki = 0.6/(K*L); % PID
Kd = (0.3*T)/K; % PID
%% UART
Ts_UART = 1; % sampling period [s]
Fs_UART = 1/Ts_UART % sampling frequency [Hz]

```